

THE COOPERATIVE TRANSVERSE
MODULATIONAL INSTABILITY OF
COUNTERPROPAGATING WAVES

by

Gregory G. Luther

Submitted in Partial Fulfillment
of the
Requirements for the Degree

DOCTOR OF PHILOSOPHY

Supervised by Professor Colin J. McKinstrie

Department of Mechanical Engineering
College of Engineering and Applied Science

University of Rochester
Rochester, New York

Reviewed by _____ 5/18/92
(Date)
ACCEPTED
The University of Rochester
Rochester, New York
Classified

1991

Curriculum Vitae

The author was born on December 1, 1962 in Rochester, New York. He earned the Bachelor of Science degree in Mechanical Engineering, with distinction, at the University of Rochester in 1985. He then attended Columbia University, receiving the Master of Science degree in Applied Physics in 1987 under the supervision of Professor C. K. Chu. He spent the summer of 1987 at the Los Alamos National Laboratory in association with the Center for Nonlinear Studies. In the Fall of 1987 he began doctoral study at the University of Rochester under the supervision of Professor C. J. McKinstrie.

Publications

G. G. Luther and C. J. McKinstrie, "Cooperative Instabilities of Counterpropagating Light Waves in Homogeneous Plasma," to be published in *Phys. Rev. Lett.*

G. G. Luther and C. J. McKinstrie, "The Transverse Modulational Instability of Counterpropagating Light Waves," to be published in *J. Opt. Soc. Am. B*.

G. G. Luther and C. J. McKinstrie, "Transverse Instabilities of Counterpropagating Light Waves," *LLE Review* **46**, DOE/DP40200-156, 65 – 79 (1991).

G. G. Luther, C. J. McKinstrie and A. L. Gaeta, "The Transverse Modulational Instability of Counterpropagating Light Waves," *OSA Proceedings on Nonlinear Dynamics in Optical Systems, Vol. 7*, Neal B. Abraham, Elsa M. Garmire, Paul Mandel, eds. (Opt. Soc. Am., Washington, D.C. 1991), pp. 205 – 209.

G. G. Luther and C. J. McKinstrie, "Transverse Modulational Instability of Collinear Waves," *J. Opt. Soc. Am. B* **7**, 1125 – 1141 (1990).

C. J. McKinstrie and G. G. Luther, "The Modulational Instability of Collinear Waves," *Physica Scripta* **T-30**, 31 – 40 (1990).

C. J. McKinstrie, G. G. Luther and S. H. Batha, "Signal Enhancement in Collinear Four-Wave Mixing," *J. Opt. Soc. Am. B* **7**, 340 – 344 (1990).

C. J. McKinstrie and G. G. Luther, "Solitary-Wave Solutions of the Generalized Three-Wave and Four-Wave Equations," *Phys. Lett. A* **127**, 14 – 18 (1988).

Oral Presentations

G. G. Luther, C. J. McKinstrie and M. V. Goldman, "Three-Dimensional Instabilities of Counterpropagating Light Waves," Quantum Electronics and Laser Science Conference, Baltimore, Maryland, May 12 - 17, 1991.

G. G. Luther, C. J. McKinstrie and M. V. Goldman, "Three-Dimensional Instabilities of Counterpropagating Waves," 32nd Annual Meeting of the APS, DPP, Cincinnati, Ohio, November 12 - 16, 1990.

G. G. Luther, C. J. McKinstrie and A. L. Gaeta, "Transverse Modulational Instability of Counterpropagating Waves and Conical Radiation," 20th Annual Anomalous Absorption Conference, Traverse City, Michigan, July 9 - 13, 1990.

G. G. Luther, C. J. McKinstrie and A. L. Gaeta, "The Transverse Modulational Instability of Counterpropagating Waves," OSA Topical Meeting on Nonlinear Dynamics in Optical Systems, Afton, Oklahoma, June 4 - 8, 1990.

G. G. Luther and C. J. McKinstrie, "Ponderomotive Filamentation in Counterpropagating Geometry," 31st Annual Meeting of the APS, DPP, Anaheim, California, November 13 - 17, 1989.

G. G. Luther, "Ponderomotive Filamentation in Counterpropagating Geometry," Department of Mechanical Engineering, University of Rochester, October 1989.

G. G. Luther, C. J. McKinstrie and R. W. Short, "The Filamentation of Two Counterpropagating Waves," 19th Annual Anomalous Absorption Conference, Fort Lewis College, Durango, Colorado, June 19 - 23, 1989.

G. G. Luther, C. J. McKinstrie and R. W. Short, "The Filamentation of Two Counterpropagating Waves," 16th IEEE International Conference on Plasma Science, Buffalo, New York, May 22 - 24, 1989.

G. G. Luther, S. H. Batha and C. J. McKinstrie, "Enhancement of the Conjugate Signal for a Collinear Four-Wave Mixing Process," 18th Annual Anomalous Absorption Conference, l'Estérel, Québec, June 26 - July 1, 1988.

G. G. Luther, "Solitary-Wave Solutions of the Generalized Three-Wave and Four-Wave Equations," Applied Mechanics Seminar Series, Department of Mechanical Engineering, University of Rochester, October 1987.

G. G. Luther, "Solitary-Wave Solutions of the Generalized Three-Wave Equations," Center for Nonlinear Studies, Los Alamos National Laboratory, August 1987.

Acknowledgments

I owe a very special debt to all the people who have enriched and supported my education thus far. For sharing his expertise and providing patient guidance, and for his efforts as coauthor on those papers upon which this work was based, I extend my deepest gratitude to Colin McKinstrie. During my years at the University of Rochester I have been fortunate to spend many hours with Alfred Clark Jr. He has been an inspirational teacher and role model. Both my work and my graduate education has been enhanced by discussions with David Meyerhofer.

For their continued enthusiasm and the support of their institutions during my graduate studies, I wish to thank Robert McCrory and Albert Simon of both the Laboratory for Laser Energetics and the Department of Mechanical Engineering at the University of Rochester, Roger Gans of the Department of Mechanical Engineering, John Soures and Charles Verdon of the Laboratory for Laser Energetics, C. K. Chu of the Department of Applied Physics at Columbia University, and David Campbell of the Center for Nonlinear Studies at Los Alamos National Laboratory.

I am indebted to all the members of the staff at the Laboratory for Laser Energetics who have aided me in completing my work there. I have profited from conversations with Eduardo Epperlein, Patrick McKenty, and Robert Short. Robert Kremens and Marie Russotto have given me a peek at some of the experimental aspects of inertial confinement fusion. Special thanks are due the illustration and word-processing staff for their help preparing manuscripts and conference presentations.

My contact with members of the Institute of Optics has been invaluable. I have learned from Robert Boyd and his group. Alex Gaeta has helped make this

interaction possible and has collaborated on the computational calculation of the finite-medium absolute instability thresholds.

It has been a great pleasure to share parts of my graduate years with friends Pierre Basseras and Mark Arend. I owe many thanks to Bedros Afeyan. His efforts to encourage me to think more critically and his passion for physics have left an enduring impression upon me.

My family has provided a stable environment that has helped sustain me. Many of the lessons learned from my grandparents have served me well during my years of graduate study; my special friend Hiram Luther has been a great inspiration. George and Jo Ann Luther, my parents, have been close friends and generous benefactors. Finally, I am fortunate to have Dana who has unselfishly shared both my moments of joy and excitement and my moments of despair.

This work was supported by the National Science Foundation under Contract No. 9057093, by the United States Department of Energy Division of Inertial Fusion under Agreement No. DE-FC03-85DP40200, and by the Laser Fusion Feasibility Project at the Laboratory for Laser Energetics, which has the following sponsors: Empire State Electric Energy Research Corporation, New York State Energy Research and Development Authority, Ontario Hydro and the University of Rochester. Such support does not imply endorsement of the content by any of the above parties.

Abstract

The transverse modulational instability (TMI), or filamentation, of two intense light waves in both finite and infinite, cubically nonlinear media is investigated using a coupled nonlinear Schroedinger-equation model. It is shown that the presence of the second laser field increases the growth rate of the filamentation instability. Systems of two copropagating waves are convectively unstable and systems of two counterpropagating waves are absolutely unstable, even when the ratio of backward- to forward-wave intensity is small. The cooperative TMI of two counterpropagating light waves is a hybrid instability caused by the interaction of four electromagnetic sidebands and is shown to occur in the spectral overlap region of single-wave TMI, phase conjugation and Bragg scattering. This instability dominates the interaction over a significant range of pump-intensity ratios in both self-focusing and self-defocusing media. The absolute phase conjugation instability dominates only for small pump-intensity ratios in self-defocusing media. Having demonstrated the importance of the cooperative TMI in nonresonant media, the analysis is extended to finite Brillouin-active media. This thesis provides the first unified treatment of the TMI, near-forward and near-backward stimulated Brillouin scattering of counterpropagating light waves. The cooperative TMI and cooperative Brillouin-enhanced four-wave mixing instabilities are shown to possess larger convective growth rates and smaller absolute instability thresholds than conventional single-pump instabilities. Either cooperative TMI or its resonantly enhanced counterparts may dominate. This analysis is consistent with recent experiments and suggests that cooperative instabilities may be important in applications of laser-plasma interactions.

Table of Contents

Curriculum Vitae	iii
Publications	v
Oral Presentations	vii
Acknowledgments	ix
Abstract	xi
Table of Contents	xiii
List of Figures	xv
1 Introduction	1
2 The Coupled Nonlinear Schroedinger Equations	9
3 Colinear Waves in Infinite Homogeneous Media	15
3.1 Copropagation in Semi-Infinite Media	16
3.2 Colinear Waves in Infinite Media	24
3.3 Summary	42
Appendix 3: Four-Wave Interactions in Infinite Media	42
4 Counterpropagating Light Waves in Finite Media	49
4.1 Two-Sideband Limits of the Four Sideband Equations	55
4.2 The Four-Sideband Interaction	65
4.2.1 Solutions in the Convective Regime	68
4.2.2 The Absolute Instability Threshold	87
4.3 Summary	100
Appendix 4: Numerical Calculation of the Absolute Threshold	101
5 Resonant Instabilities of Counterpropagating Light Waves	103

6 Discussion

117

References

121

List of Figures

3.1	The temporal growth rates of the transverse modulational instability of a single wave and of two equal-amplitude copropagating waves	20
3.2	The filament amplitudes G_{\pm} as functions of position for three different values of the wave-damping coefficients	24
3.3	The imaginary part of the dispersion surface $\omega(k_{\parallel}, k_{\perp})$ for counter-propagating waves	28
3.4	The convective and absolute impulse response of a linear system .	31
3.5	The impulse response of the transverse modulational instability of two colinear waves in self-focusing media	34
3.6	The growth rate, velocity and transverse wave number at the peak of the impulse response	36
3.7	The pole structure	37
3.8	The modulus of the single-wave dispersion function $D_2(\omega, k_{\parallel}, k_{\perp})$, evaluated at the pinch-point	38
3.9	The impulse response curves of the transverse modulational instability of two colinear waves in self-defocusing media	40
3.10	The peak temporal growth rate of the impulse response as a function of the intensity ratio R	41
4.1	The four-sideband wave vector matching diagram	51
4.2	The two-sideband wave vector matching diagrams	57
4.3	The spectral overlap region of the two-sideband interactions . . .	64
4.4	The gain spectrum for symmetric pumps in self-focusing media . .	73
4.4	Figure 4.4 continued	74

4.5	The gain spectrum for symmetric pumps in self-defocusing media	75
4.5	Figure 4.5 continued	76
4.6	The gain spectrum for asymmetric pumps in self-focusing media .	78
4.6	Figure 4.6 continued	79
4.7	The gain spectrum for asymmetric pumps in self-defocusing media	80
4.7	Figure 4.7 continued	81
4.8	The gain spectrum for asymmetric pumps in self-focusing media .	83
4.8	Figure 4.8 continued	84
4.9	The gain spectrum for asymmetric pumps in self-defocusing media	85
4.9	Figure 4.9 continued	86
4.10	The static absolute intensity threshold for self-focusing media with backward to forward pump intensity ratio $r^2 = 1.00, 0.67, 0.33, 0.10$	89
4.11	The static absolute intensity threshold in self-focusing media for $r^2 = 10^{-1}, 10^{-2}, 10^{-3}, 10^{-4}$	91
4.12	The static absolute intensity threshold as a function of the pump- wave intensity ratio in self-focusing media	92
4.13	The static absolute intensity threshold in self-defocusing media for $r^2 = 1.00, 0.67, 0.33, 0.10$	94
4.14	The absolute intensity thresholds for $r^2 = 1.0$ and $\epsilon = 2.0$	96
4.15	The absolute intensity thresholds for $r^2 = 0.1$ and $\epsilon = 2.0$	98
4.16	The minimum absolute instability threshold.	99
5.1	The gain spectrum for a strongly damped Brillouin medium . . .	108
5.1	Figure 5.1 continued	109
5.2	Thresholds for a strongly damped Brillouin medium	111
5.3	Thresholds for a weakly damped Brillouin medium	112

5.4	Thresholds as a function of pump intensity ratio for a Brillouin medium	115
-----	---	-----

Chapter 1

Introduction

The intensity pattern due to the beating of a strong electromagnetic wave with one of its electromagnetic sidebands may induce periodic variations in the index of refraction of a host medium. These stimulated material waves act as gratings and may scatter pump energy into electromagnetic sidebands. If the linear and nonlinear phases of these waves are matched inside the medium, feedback from the pump causes phase-matched sidebands to grow. This process is the basis of stimulated scattering and modulational instabilities in both plasmas [1 – 4] and other nonlinear optical materials [5 – 8].

The ponderomotive force of an electromagnetic field is proportional to the gradient of the low-frequency average of the field intensity. In an underdense plasma, this force may cause periodic intensity variations in the electromagnetic field to drive ion waves by pushing plasma particles from regions of high intensity. Since the linear dispersion relation for a light wave propagating in a plasma is $\omega^2 = \omega_e^2 + c^2 k^2$ where $\omega_e^2 = 4\pi e^2 n_e / m_e$ is the plasma frequency, e is the electron charge, n_e is the electron number density and m_e is the electron mass, it follows that the index of refraction of a plasma varies with density and ion waves act as gratings.

Both stimulated Brillouin scattering (SBS) and filamentation, also known as

the transverse modulational instability (TMI), arise in a plasma due to the interaction of an intense electromagnetic pump wave with a low-frequency ion wave. A nonresonant stationary ion wave driven by the fields acts as the grating for filamentation. These instabilities require only one electromagnetic pump wave interacting with either one or two electromagnetic sidebands.

A pair of pump waves may coexist in many nonlinear optical systems. In these systems, the properties of one light wave may be altered by variations in the index of refraction caused by the other. For instance, a pump wave may produce a signal sideband by scattering from a grating produced by the beating of a second pump wave with a probe sideband. This process is called four-wave mixing (FWM) [9, 10]. When the signal sideband propagates in the opposite direction with respect to the probe sideband the interaction is called phase conjugation by FWM. The physics of this and other multi-pump systems is richer and can be qualitatively different from the corresponding single-pump processes. Complicated instabilities of multi-pump systems which are caused by the simultaneous occurrence of simpler instabilities are called hybrid instabilities. If the result of the multi-pump interaction is to introduce a new instability or change the properties of single-pump instabilities in such a way that the effect is different than the simple superposition of the single-pump instabilities, it will be referred to as a cooperative interaction. Cooperative instabilities of two electromagnetic pump waves are the subject of this thesis.

When two waves propagate in media with an instantaneous cubic nonlinearity, media in which the index of refraction is linearly proportional to the intensity of the light wave, their spatio-temporal evolution is governed by two coupled nonlinear Schroedinger equations; one for each complex wave amplitude. These equations include the effects of convection, diffraction, dispersion and nonlinearity

on the slowly varying envelopes of the electromagnetic fields. The modulational physics embodied by the Schroedinger-equation model is extremely rich, and has been studied independently by many authors [11 – 21]. Berkhoer and Zakharov [11], Das and Sihi [12], and Menyuk [13] have shown that the modulational growth rate associated with a single, modulationally unstable wave is increased by the presence of a second, modulationally unstable wave. Inoue [14], and Som, Gupta and Dasgupta [15] have shown that a wave which is modulationally stable in isolation can be destabilized by the presence of a second, modulationally unstable wave. Litvak and Fraiman [16], Gupta, Som and Dasgupta [17], Agrawal [18], Gosh and Das [19], and McKinstrie and Bingham [20] have all shown that two waves, which are both modulationally stable by themselves, are often modulationally unstable in the other's presence! Although the modulational growth rates depend on the relative amplitudes of the waves, the existence of modulational instability does not. Thus, the evolution of two coupled waves can differ qualitatively, as well as quantitatively, from the evolution of a single wave. A tutorial introduction to coupled modulational instabilities is to be found in Ref. [21].

The linear growth of these instabilities is characterized as convectively or absolutely unstable. An instability which propagates in such a way that the velocity of both its leading and trailing edges have the same sign is said to be a convective instability. An instability which propagates in such a way that the velocities of both its leading and trailing edges have the opposite sign is said to be an absolute instability. Thus, an absolute instability grows in the frame of the medium while a convective instability grows as it propagates [22 – 24].

Most of the work described above is confined to the longitudinal modulational instability of colinear waves with comparable group velocities, which is convective in nature. The most recent activity in this area has been due to models of non-

linear wave propagation in optical fibers [25 – 28]. In addition, Law and Kaplan have recently used analogous nonlinear Schroedinger equations to show that counterpropagating waves can exhibit absolute longitudinal modulational instabilities in finite media [29, 30]. Much of the work on instabilities of counterpropagating light waves was inspired by the early papers of Silberberg and Bar-Joseph [31, 32] which showed that distributed feedback resulting from the interaction of two counterpropagating light waves leads to complex scalar instabilities. Complex polarization instabilities [33, 34] and cooperative Brillouin-enhanced FWM instabilities in the limit of no transverse effects [35, 36] have been shown to exist. Absolute phase conjugation instabilities have also been shown to exist both in plasmas [37, 38] and in other materials [39 – 42].

Considerably less work has been done on the cooperative TMI in either resonant or nonresonant media. The TMI of two copropagating waves in infinite homogeneous media has been discussed briefly by Berkhoer and Zakharov [11], and McKinstrie and Bingham [20]. The TMI of two equal-amplitude counterpropagating waves has been discussed for inhomogeneous media [43], for finite homogeneous [44 – 55], and for infinite homogeneous media [16, 21, 51]. In self-focusing media, the TMI growth rates which result from the combined effect of two counterpropagating light waves are larger than those of the single-wave case. In addition, the coupled-wave instability is absolutely unstable [43 – 54]. Thus, thermal [43] and ponderomotive [51] filamentation are both absolutely unstable when driven by counterpropagating pumps in plasma. In self-defocusing media, both a convective and an absolute TMI are introduced by the second counterpropagating light wave [46, 21, 50, 51, 53, 54]. The relationship between the TMI and the dispersive instability has been discussed in [50, 53]. In addition, the effect of polarization on the TMI has been discussed [53]. Other work has shown that a

second copropagating light wave induces convective TMI [20, 21, 51, 56] and whole beam self-focusing effects [57] in self-defocusing media [58], and enhances whole beam self-focusing effects in self-focusing media. An extensive review of recent work on transverse effects in nonlinear optical systems is contained in Ref. [59].

By studying the interaction and evolution of the nonlinear wave processes described above using a combination of analytical and computational tools, the implicit hope is to understand them deeply enough to suggest practical ways of avoiding or suppressing deleterious instabilities in applications or to use this knowledge to construct novel devices.

Direct-drive inertial confinement fusion (ICF) [60 – 62] requires high-gain fusion pellets to overcome losses associated with initiating the fusion process. Efficient conversion of laser energy into the plasma kinetic energy used to drive the compression of the fuel pellet is essential in inertial fusion. This process begins in the corona where the intense laser field must penetrate a dense plasma and deposit its energy into the pellet material. Two critical aspects of this deposition process are the laser absorption efficiency and the implosion symmetry.

A variety of physical processes can take place due to nonlinear interaction between the coronal plasma and the electromagnetic field of the laser. In the direct drive fusion process both absorption efficiency and implosion symmetry can be adversely affected by parametric and focusing instabilities. Focusing instabilities can degrade the uniformity of the laser light as it passes through the corona by enhancing modulations of the laser profile and distributing the incident laser light into filaments. This nonuniform deposition of laser energy can seed hydrodynamic instabilities, such as the Rayleigh–Taylor instability, which further degrade the laser-to-fuel coupling efficiency and inhibit the fusion gain. Parametric instabilities can degrade the absorption of laser light by scattering it away from the

pellet and are one source of hot electrons which can divert energy from the ablation process and preheat the fuel. Filamentation may influence the initiation and growth of these parametric instabilities. Though recent studies have shown that shorter wavelength lasers and beam smoothing techniques significantly reduce the effect of these instabilities, there is still much to be learned about their role in reactor size plasmas.

Counterpropagating pump waves may arise in the context of ICF when the incident pump laser is reflected from the critical density surface or is parametrically backscattered from the underdense plasma region. Burn-through light, which penetrates the target after the plasma is formed, may also act as a source for the counterpropagating pump. In previous studies [63 – 65], the counterpropagating pump wave, when shifted by the sound wave frequency as a result of the plasma motion, was shown to increase the amount of backward SBS by seeding the Stokes sideband well above the noise level. In contrast, cooperative instabilities can have larger growth rates than single-wave instabilities and need not have single-wave analogs.

The counterpropagating waves are applied externally when the laser-plasma interaction is used for phase conjugation [38]. Optical phase conjugation has applications in real-time adaptive optics, optical computing and optical communications. Generating high-quality conjugate waves by FWM requires reference waves which are uniform in the interaction volume and have sufficiently high intensity to initiate nonlinear coupling. Both filamentation and resonant absolute instabilities of the reference waves could seriously hamper efforts to utilize FWM in phase conjugation. Phase conjugation may also play a role in backscattering [66] and is being studied for use as a plasma diagnostic [37, 67].

This thesis examines the cooperative TMI and provides the first unified treat-

ment of filamentation, near-forward and near-backward SBS of counterpropagating light waves, showing that cooperative instabilities are an important part of the counterpropagating-wave interaction. In Chapter 2, the nonlinear Shroedinger model of two counterpropagating light waves in a homogeneous plasma are derived. In Chapter 3 the stability analysis of these equations shows that convective TMI of a single light wave is transformed into an absolute instability by the presence of a second, counterpropagating light wave. In Chapter 4, the linear four-sideband analysis of the cooperative TMI is presented. The four-sideband instability is decomposed into three FWM interactions which form the two-sideband limits of the four-sideband interaction. The cooperative TMI is shown to occur in the spectral overlap region of the three limiting two-sideband interactions. The linear convective gain spectrum and the threshold for absolute instability are calculated for the four-sideband system. In Chapter 5 the work on nonresonant TMI is extended to include effects due to the resonant ion-acoustic response of a plasma. In Chapter 6 recent experimental observations are discussed and a summary is provided of the major results of this work.

Chapter 2

The Coupled Nonlinear Schroedinger Equations

In this chapter the equations that govern the evolution of a pair of electromagnetic waves in a plasma are obtained. The evolution of the fields is governed by Maxwell's equations driven by the charge and current densities of the plasma; thus

$$\nabla \cdot \vec{E} = 4\pi\rho \quad (2.1)$$

$$\nabla \times \vec{E} = -\frac{1}{c}\partial_t \vec{B} \quad (2.2)$$

$$\nabla \cdot \vec{B} = 0 \quad (2.3)$$

$$\nabla \times \vec{B} = \frac{4\pi}{c}\vec{J} + \frac{1}{c}\partial_t \vec{E} , \quad (2.4)$$

where

$$\begin{aligned} \rho &= \sum_s n_s q_s , \\ \vec{J} &= \sum_s n_s q_s \vec{V}_s , \end{aligned} \quad (2.5)$$

\vec{V}_s is the velocity field of species s , n_s is its number density and q_s is its charge. In equilibrium, $n_e^{(0)} = Zn_i^{(0)} = n_0$ where Z is the ionization number and $\vec{V}_e^{(0)} = \vec{V}_i^{(0)} = 0$. The evolution of \vec{V}_s and n_s may be modeled by the fluid equations

which have the form

$$\partial_t n_s + \nabla \cdot (n_s \vec{V}_s) = 0 , \quad (2.6)$$

$$\partial_t \vec{V}_s + (\vec{V}_s \cdot \nabla) \vec{V}_s = -\frac{\nabla P_s}{n_s m_s} + \frac{q_s}{m_s} \left(\vec{E} + \frac{1}{c} \vec{V}_s \times \vec{B} \right) , \quad (2.7)$$

where $P_s = n_s T_s$ is the pressure. From Eq. (2.7) it can be seen that the first-order electron motion is in the direction of the applied electric field. Thus,

$$\vec{V}_\perp = \frac{e}{m_e c} \vec{A}_\perp , \quad (2.8)$$

where \vec{A}_\perp is the transverse component of the vector potential.

Assuming that the low-frequency plasma evolution is quasi-neutral, then $n_{el}^{(1)} \approx Z n_i^{(1)}$ and the following set of equations governing the evolution of \vec{V}_\perp and $\langle n \rangle = n_{el}^{(1)}/n_0$ arise from the root equations [4]

$$[\partial_{tt} + \omega_e^2 - c^2(\nabla^2 - \nabla \nabla \cdot)] \vec{V}_\perp = -\omega_e^2 \langle n \rangle \vec{V}_\perp , \quad (2.9)$$

$$(\partial_{tt} - c_s^2 \nabla^2) \langle n \rangle = \frac{Z m_e}{2 m_i} \nabla^2 \langle \vec{V}_\perp^2 \rangle , \quad (2.10)$$

where $\langle \rangle$ denotes an average over the high frequency components, $c_s^2 = Z T_e^{(0)}/m_i$ is the ion sound speed and $T_e^{(0)}$ is the equilibrium electron temperature. Equation (2.9) is Maxwell's wave equation for the electric field driven by the nonlinear current. Equation (2.10) is the sound wave equation driven by the low-frequency variations in light pressure. Equations (2.9) and (2.10) are the starting point for the analysis that follows.

In the presence of a second field, the ponderomotive force depends on the intensities of both fields and couples the wave evolution. The total field, \vec{V}_\perp can be chosen as

$$\vec{V}_\perp = \frac{1}{2} \{ \vec{V}_1(\vec{x}, t) \exp[i\phi_1(\vec{x}, t)] + \vec{V}_2(\vec{x}, t) \exp[i\phi_2(\vec{x}, t)] + c.c. \} \quad (2.11)$$

where

$$\phi_j = \vec{k}_j^{(0)} \cdot \vec{x} - \omega_j^{(0)} t, \quad (2.12)$$

and the wave amplitudes vary slowly in space and time. By substituting this form of \vec{V}_\perp into the equation for $\langle n \rangle$ and averaging over the fast time scale, the following equation for the density perturbation is obtained:

$$\begin{aligned} (\partial_{tt} - c_s^2 \nabla^2) \langle n \rangle = & \frac{Z m_e}{8 m_i} \nabla^2 (|\vec{V}_1|^2 + |\vec{V}_2|^2 \\ & + \langle \vec{V}_1 \cdot \vec{V}_2^* \exp(\phi_1 - \phi_2) + \vec{V}_1^* \cdot \vec{V}_2 \exp(\phi_2 - \phi_1) \rangle). \end{aligned} \quad (2.13)$$

The last two terms on the right side of Eq. (2.13) will not appear for $|\omega_1 - \omega_2| \gg \omega_{ia}$ or for waves with orthogonal linear polarizations. If $\omega_2^0 \approx \omega_1^0$ and $\vec{k}_2^{(0)} \approx -\vec{k}_1^{(0)}$, then the cross terms will drive a short-wavelength density grating.

When the instability growth time occurs on a time scale long compared to the time associated with the natural ion motion ($\omega^2 \ll c_s^2 k^2$), an algebraic equation for $\langle n \rangle$ is obtained. This condition implies that the ion-acoustic wave is driven nonresonantly and, hence, that there is little indirect absorption of laser energy. In Chapter 5 this restriction will be relaxed. By substituting the algebraic expression for $\langle n \rangle$ in Eq. (2.13), and neglecting the second-order temporal derivative and the second-order longitudinal spatial derivative of the slowly-varying wave amplitude, the equations

$$\begin{aligned} [2i(\omega_j^{(0)} \partial_t + c^2 \vec{k}_j^{(0)} \cdot \nabla) + c^2 \nabla_\perp^2] V_j &= -\frac{\omega_e^2}{4v_e^2} (|V_1|^2 + \epsilon |V_2|^2) V_j, \\ [2i(\omega_2^{(0)} \partial_t + c^2 \vec{k}_2^{(0)} \cdot \nabla) + c^2 \nabla_\perp^2] V_2 &= -\frac{\omega_e^2}{4v_e^2} (|V_2|^2 + \epsilon |V_1|^2) V_2, \end{aligned} \quad (2.14)$$

are obtained, where v_e is the electron thermal speed, it is understood that $\omega_j^{(0)}$ and $\vec{k}_j^{(0)}$ satisfy the linear electromagnetic dispersion relation, and ϵ is either 1 or 2, as explained above. An extra factor of 4 has been incorporated in the denominators

of the nonlinear terms so that the V_j 's now represent the *peak* electron quiver velocities.

Equations (2.14) can be written in the canonical form [44 – 46, 22, 48]:

$$\begin{aligned} [i(\partial_t + v_1\partial_z) + \mu_{1\perp}\nabla_{\perp}^2 + \lambda_{11}|A_1|^2 + \lambda_{12}|A_2|^2]A_1 &= 0, \\ [i(\partial_t + v_2\partial_z) + \mu_{2\perp}\nabla_{\perp}^2 + \lambda_{21}|A_1|^2 + \lambda_{22}|A_2|^2]A_2 &= 0, \end{aligned} \quad (2.15)$$

where

$$A_j = \frac{V_j}{v_e}, v_j = \frac{c^2 k_j^{(0)}}{\omega_j^{(0)}}, \mu_{j\perp} = \frac{c^2}{2\omega_j^{(0)}}, \lambda_{jl} = \frac{\omega_e^2}{8\omega_j^{(0)}} \epsilon^{(1-\delta_{jl})}, \quad (2.16)$$

and δ_{jl} is the Kronecker Delta. These scalings yield a convenient form of the coupled nonlinear Schroedinger equations, (2.15), where v_j is the group velocity, $\mu_{j\perp}$ is the diffraction coefficient, and the λ_{jl} are the self nonlinearities when $j = l$ and the cross-coupling nonlinearities when $j \neq l$. Although they have been obtained by considering the interaction of intense laser radiation with a uniform plasma, these equations are sufficiently general to apply to a host of relevant problems in which a small amplitude expansion of the governing equations applies. In particular, these equations describe the filamentation and nonlinear focusing of laser beams in media with instantaneous Kerr nonlinearities. In the field of nonlinear optics the λ_{jl} are generally given in terms of the third order nonlinear susceptibility. It is also more common in the nonlinear optics literature to write the convective terms in such a way that the partial derivative with respect to time is multiplied by the inverse of the group velocity and μ and λ are redefined accordingly.

The coupled nonlinear Schroedinger equations model the propagation of two counterpropagating light waves through a medium in which the index of refraction may either increase or decrease as a linear function of the total local field

intensity, has no natural resonances, and responds to intensity variations on time scales much shorter than the time scales associated with variations in the envelope amplitudes of the fields. If the medium is homogeneous, these equations are independent of translations and rotations. In Chapters 3 and 4 these equations are studied in detail. In Chapter 5 the restrictions of the nonlinear Shroedinger model are relaxed so that the effects of sound-wave resonances can be considered.

Chapter 3

Colinear Waves in Infinite Homogeneous Media

In this chapter, the transverse modulational instability (TMI) of two colinear waves propagating in media with instantaneous cubic nonlinearities is investigated using the coupled nonlinear Schroedinger-equations (2.15). No restrictions are made on either the relative amplitudes of the waves, or on the signs and magnitudes of the group velocities of the waves. The outline is as follows. In the first section, analytic solutions of the linearized version of the governing equations are obtained for two waves propagating with equal group velocities in a semi-infinite medium. Then the linear stability analysis for two colinear waves propagating with arbitrary group speeds in an infinite medium is used to show how the convective and absolute nature of the TMI depends on the relative amplitudes of the waves. A summary of the chapter is provided in the final section.

To make the physical content of the results more transparent, it is assumed that $\lambda_{22} \approx \lambda_{11}$ and $\mu_{2\perp} \approx \mu_{1\perp} = \mu_{\perp}$. Strictly speaking, these approximations only apply to waves of comparable frequency or to different polarizations of the same wave. However, with the single exception of the study of wave-damping effects in Sec. 3.1, none of the results will depend sensitively on these approximations.

3.1 Copropagation in Semi-Infinite Media

When the waves have equal group velocities, the linearized equations can be solved explicitly using the method of characteristics. To illustrate this method, the single-wave instability is considered first. In terms of the characteristic variables

$$\tau = t - z/v, \quad z, \quad (3.1)$$

the nonlinear Schroedinger equation can be written as

$$[iv\partial_z + \mu_{\perp}\nabla_{\perp}^2 + \lambda_{11}|A_1|^2]A_1 = 0 \quad (3.2)$$

and is to be solved for $z > 0$. Since the operator ∂_{τ} does not appear in Eq. (3.2), the wave amplitude A_1 can depend only parametrically on τ . Equation (3.2) has the equilibrium solution

$$A_{1e}(\tau, z) = A_1(\tau) \exp[i\lambda_{11}|A_1(\tau)|^2 z/v], \quad (3.3)$$

where, without loss of generality, the equilibrium parameter $A_1(\tau)$ can be taken to be real. The stability of this plane-wave equilibrium, with respect to small perturbations in wave amplitude, can be studied by substituting the ansatz

$$A_1(t, \vec{x}) = [A_{1e}(\tau) + A_1^{(1)}(\tau, z)\phi(\vec{x}_{\perp})] \exp[i\lambda_{11}|A_1(\tau)|^2 z/v] \quad (3.4)$$

into Eq. (3.2) and retaining only those terms which are linear in the perturbed wave amplitudes. If ϕ is assumed to satisfy the Helmholtz equation

$$(\nabla_{\perp}^2 + k_{\perp}^2)\phi = 0, \quad (3.5)$$

in whatever coordinate system is appropriate, the linearized equation is

$$[iv\partial_z - \mu_{\perp}k_{\perp}^2 + \lambda_{11}|A_1|^2]A_1^{(1)} + \lambda_{11}|A_1|^2 A_1^{(1)*} = 0. \quad (3.6)$$

This complex equation is equivalent to the real equations

$$[(v\partial_z)^2 - \mu_\perp k_\perp^2 (2\lambda_{11}|A_1|^2 - \mu_\perp k_\perp^2)]A_{1r}^{(1)} = 0, \quad (3.7)$$

$$v\partial_z A_{1r}^{(1)} - \mu_\perp k_\perp^2 A_{1i}^{(1)} = 0, \quad (3.8)$$

where the subscripts r and i denote the real and imaginary parts of the perturbed wave amplitude. It follows from Eqs. (3.7) and (3.8), together with the boundary conditions

$$A_{1i}^{(1)}(\tau, 0) = 0, \quad (3.9)$$

that

$$A_{1r}^{(1)}(t, z) = A_{1r}^{(1)}(\tau, 0) \cosh(\gamma z/v), \quad (3.10)$$

where

$$\gamma^2(\tau) = \mu_\perp k_\perp^2 (2\lambda_{11}|A_1(\tau)|^2 - \mu_\perp k_\perp^2). \quad (3.11)$$

The corresponding solution for $A_{1i}^{(1)}$ follows from Eqs. (3.8) and (3.10). If the product $\mu_\perp \lambda_{11}$ is positive, equilibrium (3.3) is modulationally unstable with respect to perturbations whose wavenumbers satisfy $0 < |\mu_\perp k_\perp^2| < 2|\lambda_{11}A_1^2(\tau)|$. The amplitude perturbations grow as they convect, with a maximal temporal growth rate of $\lambda_{11}|A_1(\tau)|^2$, corresponding to an optimal transverse wavenumber of $(\lambda_{11}/\mu_\perp)^{1/2}|A_1(\tau)|$. Notice that, since ϕ is *any* solution of the Helmholtz equation, the perturbations in wave amplitude need not be planar.

From Eqs. (2.16) and (3.11), the maximal growth rate and optimal transverse wavenumber for the single-wave instability of wave 1 are given by

$$\gamma_1 = \frac{\omega_e^2}{8\omega_1} \left| \frac{v_1}{v_e} \right|^2, \quad k_\perp = \frac{\omega_e}{2c} \left| \frac{v_1}{v_e} \right|, \quad (3.12)$$

respectively, where

$$\left| \frac{v_1}{v_e} \right| \approx 1.9 \times 10^{-8} \frac{\lambda[\mu\text{m}](I[\text{Wcm}^{-2}])^{1/2}}{(T_e[\text{KeV}])^{1/2}}. \quad (3.13)$$

Using these results, the exponent of the single-wave convective gain

$$\frac{\gamma_1 l}{v} = \frac{(k_1 l)(n_e/n_c) \left| \frac{v_1}{v_e} \right|^2}{8[1 - (n_e/n_c)]^{1/2}} \quad (3.14)$$

and the corresponding measure of the transverse wavenumber

$$\frac{\mu_\perp k_\perp^2 l}{v} = \frac{k_\perp^2 l}{2k_1[1 - (n_e/n_c)]^{1/2}}, \quad (3.15)$$

where k_1 is the vacuum wavenumber of the incident wave and the critical electron density

$$n_c[\text{cm}^{-3}] \approx 1.1 \times 10^{21} (\lambda[\mu\text{m}])^{-2}. \quad (3.16)$$

For the experimental parameters of Young *et al.* [68, 69] ($\lambda \approx 1 \mu\text{m}$, $l \approx 300 \mu\text{m}$, $n_e \approx 0.1n_c$ and $T_e \approx 0.8 \text{ KeV}$), it follows from Eqs. (3.13) and (3.14) that $I[\text{Wcm}^{-2}] \approx (\gamma_1 l/v) \times 10^{14}$.

Now consider the evolution of two copropagating waves. For such waves, Eqs. (2.15) have the equilibrium solution

$$\begin{aligned} A_{1e} &= A_1(\tau) \exp[i(\lambda_{11}|A_1(\tau)|^2 + \lambda_{12}|A_2(\tau)|^2)z/v], \\ A_{2e} &= A_2(\tau) \exp[i(\lambda_{21}|A_1(\tau)|^2 + \lambda_{22}|A_2(\tau)|^2)z/v], \end{aligned} \quad (3.17)$$

where, without loss of generality, the equilibrium parameters $A_1(\tau)$ and $A_2(\tau)$ can both be taken to be real. Small perturbations of this plane-wave equilibrium are governed by the equations

$$[(v\partial_z)^2 - \mu_\perp k_\perp^2 (2\lambda_{11}|A_1|^2 - \mu_\perp k_\perp^2)]A_{1r}^{(1)} - 2\lambda_{12}|A_1 A_2| \mu_\perp k_\perp^2 A_{2r}^{(1)} = 0, \quad (3.18)$$

$$v\partial_z A_{1r}^{(1)} - \mu_\perp k_\perp^2 A_{1i}^{(1)} = 0 \quad (3.19)$$

for wave 1, together with corresponding equations for wave 2. Equation (3.18) and its analog for wave 2 can be written in the matrix form

$$(v\partial_z)^2 A - MA = 0, \quad (3.20)$$

where A is the column vector $(A_{1r}^{(1)}, A_{2r}^{(1)})^T$ and M is the matrix

$$\begin{pmatrix} \mu_{\perp} k_{\perp}^2 (2\lambda_{11}|A_1|^2 - \mu_{\perp} k_{\perp}^2) & 2\lambda_{12}|A_1 A_2| \mu_{\perp} k_{\perp}^2 \\ 2\lambda_{21}|A_2 A_1| \mu_{\perp} k_{\perp}^2 & \mu_{\perp} k_{\perp}^2 (2\lambda_{22}|A_2|^2 - \mu_{\perp} k_{\perp}^2) \end{pmatrix}. \quad (3.21)$$

Let $E_{\pm}(\tau)$ denote the eigenvectors of M and let $F_{\pm}(\tau)$ denote the inner products $(E_{\pm}(\tau), A(\tau, 0))$. Then the solution of Eq. (3.20) can be written in the form

$$A(t, z) = E_+(\tau)F_+(\tau)G_+(\tau, z) + E_-(\tau)F_-(\tau)G_-(\tau, z), \quad (3.22)$$

where the functions $G_{\pm}(\tau, z)$ satisfy the auxiliary equations

$$[(v\partial_z)^2 - \mu_{\perp} k_{\perp}^2 (2\Delta_{\pm} - \mu_{\perp} k_{\perp}^2)]G_{\pm} = 0, \quad (3.23)$$

together with the boundary conditions

$$G_{\pm}(\tau, 0) = 1, \quad v\partial_z G_{\pm}(\tau, 0) = 0. \quad (3.24)$$

Equations (3.23) are identical in form to Eq. (3.7), with driving terms

$$\begin{aligned} 2\Delta_{\pm} &= (\lambda_{11}|A_1|^2 + \lambda_{22}|A_2|^2) \\ &\pm [(\lambda_{11}|A_1|^2 - \lambda_{22}|A_2|^2)^2 + (2\lambda_{12}|A_1 A_2|)^2]^{1/2}, \end{aligned} \quad (3.25)$$

which now depend on the equilibrium amplitudes of both waves. The solutions of Eqs. (3.23) subject to the boundary conditions (3.24) are simply

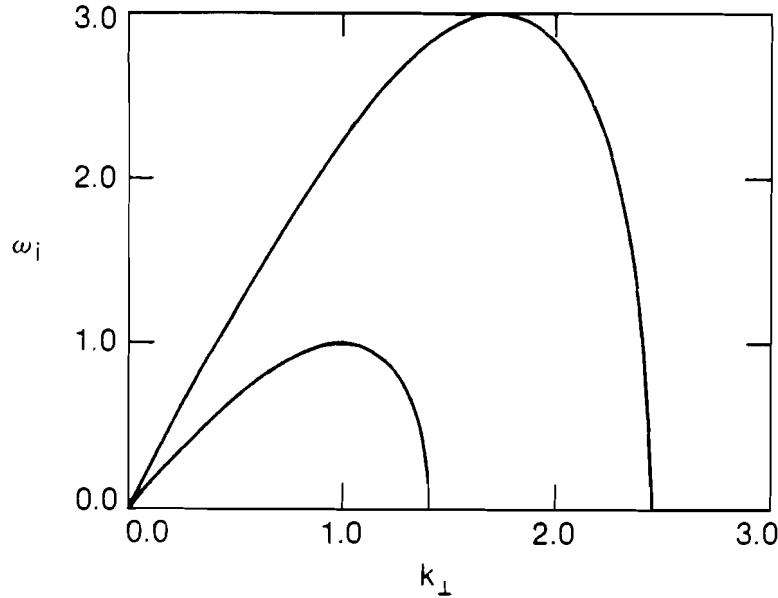
$$G_{\pm}(\tau, z) = \cosh(\gamma_{\pm} z/v), \quad (3.26)$$

where

$$\gamma_{\pm}^2(\tau) = \mu_{\perp} k_{\perp}^2 (2\Delta_{\pm}(\tau) - \mu_{\perp} k_{\perp}^2) \quad (3.27)$$

are the eigenvalues of the matrix M .

Suppose that λ_{11} and μ_{\perp} are positive, so that waves 1 and 2 are both unstable by themselves. Then, $\mu_{\perp} \Delta_+(\tau)$ is positive, and it follows from Eqs. (3.25) – (3.27)



P819

Figure 3.1: The temporal growth rate of sinusoidal perturbations in wave amplitude is plotted as a function of transverse wavenumber for the case in which $\mu_{\perp} \lambda_{11}$ is positive and $\lambda_{12}/\lambda_{11}$ is equal to 2. The lower curve corresponds to the TMI of a single wave, while the upper curve corresponds to the TMI of two equal-amplitude copropagating waves. The temporal growth rates are normalized to $|\lambda_{11} A_1^2|$ and the transverse wavenumbers are normalized to $(\lambda_{11}/\mu_{\perp})^{1/2}|A_1|$, their optimal values for the single-wave instability.

that equilibrium (3.17) is modulationally unstable with respect to perturbations whose wavenumbers satisfy $0 < \mu_{\perp} k_{\perp}^2 < 2\Delta_+(\tau)$. The amplitude perturbations grow as they convect, with a maximal temporal growth rate of $\Delta_+(\tau)$ corresponding to an optimal transverse wavenumber of $(\Delta_+(\tau)/\mu_{\perp})^{1/2}$. The temporal growth rate is plotted as a function of transverse wavenumber in Fig. 3.1, for the common case in which $|A_2(\tau)| = |A_1(\tau)|$ and $\lambda_{12} = 2\lambda_{11}$. The lower curve corresponds to the single-wave instability, while the upper curve corresponds to the coupled-wave instability. Notice that the optimal transverse wavenumber for the coupled-wave instability lies outside the range of unstable wavenumbers for the single-wave instability. Let the components of the eigenvectors $E_{\pm}(\tau)$ be denoted by $e_1^{\pm}(\tau)$ and

$e_2^\pm(\tau)$. Then, it follows from Eqs. (3.18), (3.23) and (3.25) that

$$\frac{e_2^+}{e_1^+} = \frac{\Delta_+ - \lambda_{11}|A_1|^2}{\lambda_{12}|A_1A_2|}. \quad (3.28)$$

For the common case in which λ_{11} and λ_{12} have the same sign, this amplitude ratio is positive and the maxima of waves 1 and 2 are aligned. This alignment of the local maxima allows the self-nonlinear and cross-nonlinear wavenumber shifts to add constructively and enhance the phase-front curvature responsible for the TMI.

Conversely, suppose that λ_{11} is positive and μ_\perp is negative, so that waves 1 and 2 are both stable by themselves. Then, in this case, $\mu_\perp\Delta_+(\tau)$ is negative. However $\mu_\perp\Delta_-(\tau)$ is positive whenever

$$|\lambda_{12}| > (\lambda_{11}\lambda_{22})^{1/2} \quad (3.29)$$

and equilibrium (3.17) is modulationally unstable with respect to perturbations whose wavenumbers satisfy $0 < |\mu_\perp k_\perp^2| < 2|\Delta_-(\tau)|$. The amplitude perturbations grow as they convect, with a maximal temporal growth rate of $|\Delta_-(\tau)|$ corresponding to an optimal transverse wavenumber of $(\Delta_-(\tau)/\mu_\perp)^{1/2}$. For the common case in which λ_{11} and λ_{12} have the same sign, the amplitude ratio

$$\frac{e_2^-}{e_1^-} = \frac{\Delta_- - \lambda_{11}|A_1|^2}{\lambda_{12}|A_1A_2|} \quad (3.30)$$

is negative, and the maxima of wave 1 are aligned with the minima of wave 2. It is this misalignment of the local maxima which allows the cross-nonlinear wavenumber shift to compensate for the self-nonlinear wavenumber shift and produce the concave phase-fronts required for the TMI. (Although the geometry is different, it is the same addition of self-nonlinear and cross-nonlinear wavenumber shifts that makes possible the longitudinal modulational instability [18, 20].) Similar remarks

apply to the other choices of signs for λ_{11} and μ_{\perp} ; whenever inequality (3.29) is satisfied, one of $\mu_{\perp}\Delta_{\pm}(\tau)$ is always positive and the waves are modulationally unstable [20].

The collisional damping of the waves is often important in experiments, and can be modeled by the inclusion of the terms $i\nu_1 A_1$ and $i\nu_2 A_2$ in the first and second of Eqs. (2.15), respectively. In many applications involving light waves, the damping coefficients of the waves are approximately equal. The equality of damping coefficients will henceforth be assumed. Usually, one neglects the effects of damping on the plane-wave equilibrium (3.17) and retains the effects of damping only on the perturbed wave amplitudes. The changes in the characteristic analysis necessitated by this idealized approach are $v\partial_z \rightarrow v\partial_z + \nu$ in Eq. (3.20) – (3.24), and, hence, $G_{\pm}(\tau, z) \rightarrow G_{\pm}(\tau, z) \exp(-\nu z/v)$ in Eqs. (3.26). Consequently, one expects the perturbations in wave amplitude to grow as they convect whenever

$$\gamma_{\pm} > \nu . \quad (3.31)$$

However, Eq. (3.20) can be solved exactly, even with the effects of equal pump-wave damping taken into account. The exact solutions can then be used to gauge the accuracy of the usual idealized approach.

In the presence of damping, Eqs. (2.15) have the equilibrium solution

$$\begin{aligned} A_{1e} &= A_1(\tau) \exp[-\nu z/v + i(\lambda_{11}|A_1(\tau)|^2 + \lambda_{12}|A_2(\tau)|^2) \int_0^z \exp(-2\nu z'/v) dz'/v] , \\ A_{2e} &= A_2(\tau) \exp[-\nu z/v + i(\lambda_{21}|A_1(\tau)|^2 + \lambda_{22}|A_2(\tau)|^2) \int_0^z \exp(-2\nu z'/v) dz'/v] . \end{aligned}$$

The characteristic analysis of the linearized equations proceeds as for the conservative case, with the exception that the functions G_{\pm} now satisfy the auxiliary equations

$$[(v\partial_z + \nu)^2 - \mu_{\perp} k_{\perp}^2 (2\Delta_{\pm} \exp(-2\nu z/v) - \mu_{\perp} k_{\perp}^2)] G_{\pm} = 0 , \quad (3.32)$$

together with the boundary conditions

$$G_{\pm}(\tau, 0) = 1, \quad (v\partial_z + \nu)G_{\pm}(\tau, 0) = 0. \quad (3.33)$$

Equations (3.32) can be solved by defining new dependent and independent variables [70]

$$H_{\pm} = G_{\pm} \exp(\nu z/v), \quad \zeta_{\pm} = \beta_{\pm} \exp(-\nu z/v), \quad (3.34)$$

respectively. The functions H_{\pm} satisfy the auxiliary equations

$$[(\zeta_{\pm}\partial_{\zeta_{\pm}})(\zeta_{\pm}\partial_{\zeta_{\pm}}) + \alpha^2 - \zeta_{\pm}^2]H_{\pm} = 0, \quad (3.35)$$

where

$$\alpha = \mu_{\perp} k_{\perp}^2 / \nu, \quad \beta_{\pm} = (2\mu_{\perp} k_{\perp}^2 \Delta_{\pm})^{1/2} / \nu, \quad (3.36)$$

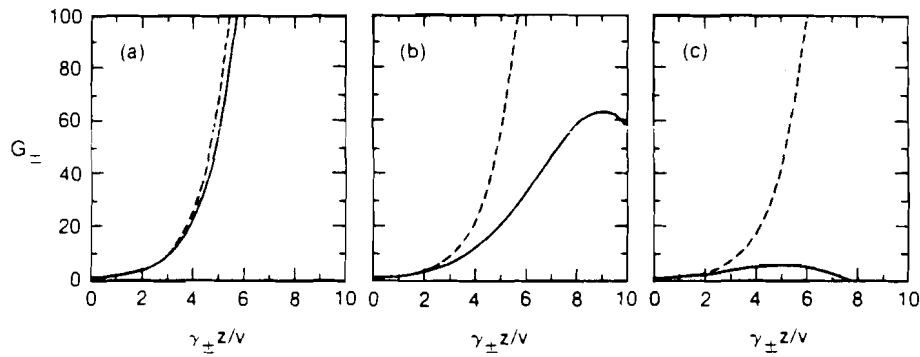
together with the boundary conditions

$$H_{\pm}(\tau, \beta_{\pm}) = 1, \quad \partial_{\zeta_{\pm}} H_{\pm}(\tau, \beta_{\pm}) = 0. \quad (3.37)$$

Since Eqs. (3.35) are just variants of Bessel's equation, their solutions, consistent with the boundary conditions (3.37), can be written as

$$H_{\pm}(\tau, \zeta_{\pm}) = \frac{J'_{-i\alpha}(i\beta_{\pm})J_{i\alpha}(i\zeta_{\pm}) - J'_{i\alpha}(i\beta_{\pm})J_{-i\alpha}(i\zeta_{\pm})}{J'_{-i\alpha}(i\beta_{\pm})J_{i\alpha}(i\beta_{\pm}) - J'_{i\alpha}(i\beta_{\pm})J_{-i\alpha}(i\beta_{\pm})}. \quad (3.38)$$

Although the solutions specified by Eqs. (3.34) and (3.38) are explicit, the effects of damping can be seen more easily from the numerical solutions of Eqs. (3.32) and (3.33), which are displayed in Fig. 3.2. The solid lines represent the exact solutions of Eqs. (3.32) and (3.33), while the broken lines represent the idealized solutions which neglect the effects of pump-wave damping. The transverse wavenumber was taken to have its optimal value throughout the Figure, so that $\gamma_{\pm} = \Delta_{\pm}$. It can be seen from Fig. 3.2(a) that the two solutions are approximately equal for the case in which $\nu = 0.01\gamma_{\pm}$. Although the two solutions differ considerably



P835

Figure 3.2: The filament amplitudes G_{\pm} are plotted as functions of position for three different values of the wave-damping coefficients. (a) $\nu = 0.01\gamma_{\pm}$. (b) $\nu = 0.05\gamma_{\pm}$. (c) $\nu = 0.10\gamma_{\pm}$. The solid line represents the exact solutions, while the broken line represents the idealized solutions which neglect the effects of pump-wave damping.

when $\nu = 0.05\gamma_{\pm}$, the exact solution does exhibit significant gain, as shown in Fig. 3.2(b). The case in which $\nu = 0.10\gamma_{\pm}$ is displayed in Fig. 3.2(c). Not only do the two solutions differ considerably, but the exact solution also exhibits negligible gain. Thus, the true instability threshold in the presence of damping exceeds the naive estimate by a factor of about 20. In this chapter and in Chapter 4 damping will be neglected, with the understanding that the analysis and physics is modified substantially in those applications for which damping is significant.

3.2 Colinear Waves in Infinite Media

When the waves are colinear, with unequal group velocities, the evolution of small perturbations in wave amplitude is dispersive and the method of characteristics cannot normally be used to solve the linearized equations. Consequently, in this section, Fourier – Laplace transform techniques are used to study the wave evolution. By definition, there are no boundaries in infinite media, so an initial-value problem is formulated.

Equations (2.15) have the equilibrium solution

$$\begin{aligned} A_{1e} &= A_1 \exp[i(\lambda_{11}|A_1|^2 + \lambda_{12}|A_2|^2)t] \\ A_{2e} &= A_2 \exp[i(\lambda_{21}|A_1|^2 + \lambda_{22}|A_2|^2)t] , \end{aligned} \quad (3.39)$$

where the equilibrium parameters A_1 and A_2 can be taken to be real and, henceforth, are assumed to be constant. Small perturbations of this plane-wave equilibrium, with transverse wave vector \vec{k}_\perp , are governed by the equations

$$\begin{aligned} [i(\partial_t + v_1 \partial_z) - \mu_\perp k_\perp^2 + \lambda_{11}|A_1|^2]A_1^{(1)} + \lambda_{11}|A_1|^2 A_1^{(1)*} \\ + \lambda_{12}|A_1 A_2|A_2^{(1)} + \lambda_{12}|A_1 A_2|A_2^{(1)*} = 0 , \\ [i(\partial_t + v_2 \partial_z) - \mu_\perp k_\perp^2 + \lambda_{22}|A_2|^2]A_2^{(1)} + \lambda_{22}|A_2|^2 A_2^{(1)*} \\ + \lambda_{21}|A_2 A_1|A_1^{(1)} + \lambda_{21}|A_2 A_1|A_1^{(1)*} = 0 \end{aligned} \quad (3.40)$$

together with their complex conjugates. Subject to the initial conditions

$$\begin{aligned} A_{1r}^{(1)}(0, z) &= F_{1r}(z) , \quad \partial_t A_{1r}^{(1)}(0, z) = G_{1r}(z) , \\ A_{2r}^{(1)}(0, z) &= F_{2r}(z) , \quad \partial_t A_{2r}^{(1)}(0, z) = G_{2r}(z) , \end{aligned} \quad (3.41)$$

the solution of Eqs. (3.40) for wave 1 can be written in the form

$$A_{1r}^{(1)}(t, z) = \int_F \int_L \frac{S_1(\omega, k_\parallel, k_\perp)}{D_c(\omega, k_\parallel, k_\perp)} \exp[i(k_\parallel z - \omega t)] d\omega dk_\parallel , \quad (3.42)$$

where F and L denote the usual Fourier and Laplace contours [22 – 24], respectively. The source function

$$\begin{aligned} S_1(\omega, k_\parallel, k_\perp) &= \frac{1}{2\pi} \left(D_2(\omega, k_\parallel, k_\perp) [i(\omega - 2v_1 k_\parallel) F_{1r}(k_\parallel) - G_{1r}(k_\parallel)] \right. \\ &\quad \left. - 2\lambda_{12}|A_1 A_2| \mu_\perp k_\perp^2 [i(\omega - 2v_1 k_\parallel) F_{2r}(k_\parallel) - G_{2r}(k_\parallel)] \right) \end{aligned} \quad (3.43)$$

depends on the initial conditions chosen for both $A_1^{(1)}$ and $A_2^{(1)}$,

$$D_2(\omega, k_\parallel, k_\perp) = [(\omega - v_2 k_\parallel)^2 + \mu_\perp k_\perp^2 (2\lambda_{22}|A_2|^2 - \mu_\perp k_\perp^2)] \quad (3.44)$$

is the single-wave dispersion function of wave 2 and

$$\begin{aligned}
D_c(\omega, k_{\parallel}, k_{\perp}) = & [(\omega - v_1 k_{\parallel})^2 + \mu_{\perp} k_{\perp}^2 (2\lambda_{11}|A_1|^2 - \mu_{\perp} k_{\perp}^2)] \\
& [(\omega - v_2 k_{\parallel})^2 + \mu_{\perp} k_{\perp}^2 (2\lambda_{22}|A_2|^2 - \mu_{\perp} k_{\perp}^2)] \\
& - [2\lambda_{12}|A_1 A_2| \mu_{\perp} k_{\perp}^2] [2\lambda_{21}|A_2 A_1| \mu_{\perp} k_{\perp}^2] \quad (3.45)
\end{aligned}$$

is the coupled-wave dispersion function. By interchanging the subscripts 1 and 2, the corresponding solution for $A_{2r}^{(1)}$ can be obtained. The analysis of Eqs. (3.42) -- (3.45) can be simplified by making the substitutions

$$\frac{\omega}{\lambda_{11}|A_1|^2} \longrightarrow \omega, \quad \frac{v_j k_{\parallel}}{\lambda_{11}|A_1|^2} \longrightarrow v_j k_{\parallel}, \quad \frac{\mu_{\perp} k_{\perp}^2}{\lambda_{11}|A_1|^2} \longrightarrow k_{\perp}^2, \quad (3.46)$$

which correspond to measuring all frequencies relative to the maximal growth rate of the single-wave instability of wave 1, assuming it to be unstable, and all transverse wavenumbers relative to the optimal transverse wavenumber of wave 1. These substitutions result in the dimensionless dispersion function

$$\begin{aligned}
D_c(\omega, k_{\parallel}, k_{\perp}) = & [(\omega - v_s k_{\parallel} - v_d k_{\parallel})^2 + \sigma_{\perp} k_{\perp}^2 (2 - \sigma_{\perp} k_{\perp}^2)] \\
& [(\omega - v_s k_{\parallel} + v_d k_{\parallel})^2 + \sigma_{\perp} k_{\perp}^2 (2r^2 - \sigma_{\perp} k_{\perp}^2)] \\
& - [2\epsilon r \sigma_{\perp} k_{\perp}^2]^2, \quad (3.47)
\end{aligned}$$

where the sum and difference velocities v_s and v_d are equal to $\frac{1}{2}(v_1 + v_2)$ and $\frac{1}{2}(v_1 - v_2)$ respectively, σ_{\perp} is the sign of the product $\mu_{\perp} \lambda_{11}$ and determines whether or not the waves are modulationally unstable by themselves, ϵ is the ratio $\lambda_{12}/\lambda_{11}$, and r is the pump-wave amplitude ratio $|A_2/A_1|$. The pump-wave intensity ratio r^2 will also be denoted by the symbol R .

For the special case in which the perturbations in wave amplitude are initially sinusoidal in the z -direction, Eq. (3.42) shows that they remain so with a temporal growth rate ω_i ; which follows from the coupled dispersion function (3.47).

When v_d is equal to zero, the solutions of the coupled dispersion equation are given by the simple expression

$$\omega = v_s k_{\parallel} \pm i[\sigma_{\perp} k_{\perp}^2 (2\delta_{\pm} - \sigma_{\perp} k_{\perp}^2)]^{1/2}, \quad (3.48)$$

where

$$2\delta_{\pm} = (1 + r^2) \pm [(1 - r^2)^2 + (2\epsilon r)^2]^{1/2} \quad (3.49)$$

is the driving term for the coupled-wave instability. Eqs. (3.48) and (3.49) are dimensionless versions of Eqs. (3.25) and (3.27), respectively. If $|\epsilon|$ is greater than unity, one of $\sigma_{\perp} \delta_{\pm}$ is always positive and equilibrium (3.39) is modulationally unstable with respect to amplitude perturbations whose transverse wavenumbers satisfy $0 < k_{\perp}^2 < 2\sigma_{\perp} \delta_{\pm}$. The maximal temporal growth rate is equal to $\sigma_{\perp} \delta_{\pm}$ and corresponds to the optimal transverse wavenumber $(\sigma_{\perp} \delta_{\pm})^{1/2}$. It is a noteworthy feature of the modulational instability of copropagating waves that the region of k_{\perp} -space corresponding to unstable amplitude perturbations is *bounded*.

When v_d is nonzero, the solutions of the coupled-wave dispersion equation can be written in the simple analytic form

$$\begin{aligned} (\omega - v_s k_{\parallel})^2 &= (v_d k_{\parallel})^2 - [\sigma_{\perp} k_{\perp}^2 (2 - \sigma_{\perp} k_{\perp}^2)] \\ &\quad \pm \left([2\epsilon \sigma_{\perp} k_{\perp}^2]^2 - 4(v_d k_{\parallel})^2 [\sigma_{\perp} k_{\perp}^2 (2 - \sigma_{\perp} k_{\perp}^2)] \right)^{1/2} \end{aligned} \quad (3.50)$$

only for the special case in which R is equal to unity. The imaginary part of the dispersion surface $\omega(k_{\parallel}, k_{\perp})$ is displayed in the upper graph of Fig. 3.3. The maximal temporal growth rate is equal to $1 + |\epsilon|$, corresponding to an optimal transverse wavenumber of $(1 + |\epsilon|)^{1/2}$ and a longitudinal wavenumber of zero. These results are identical to the results described in the preceding paragraph for two copropagating waves of equal amplitude. When $|v_d k_{\parallel}|$ is much larger than k_{\perp}^2 ,

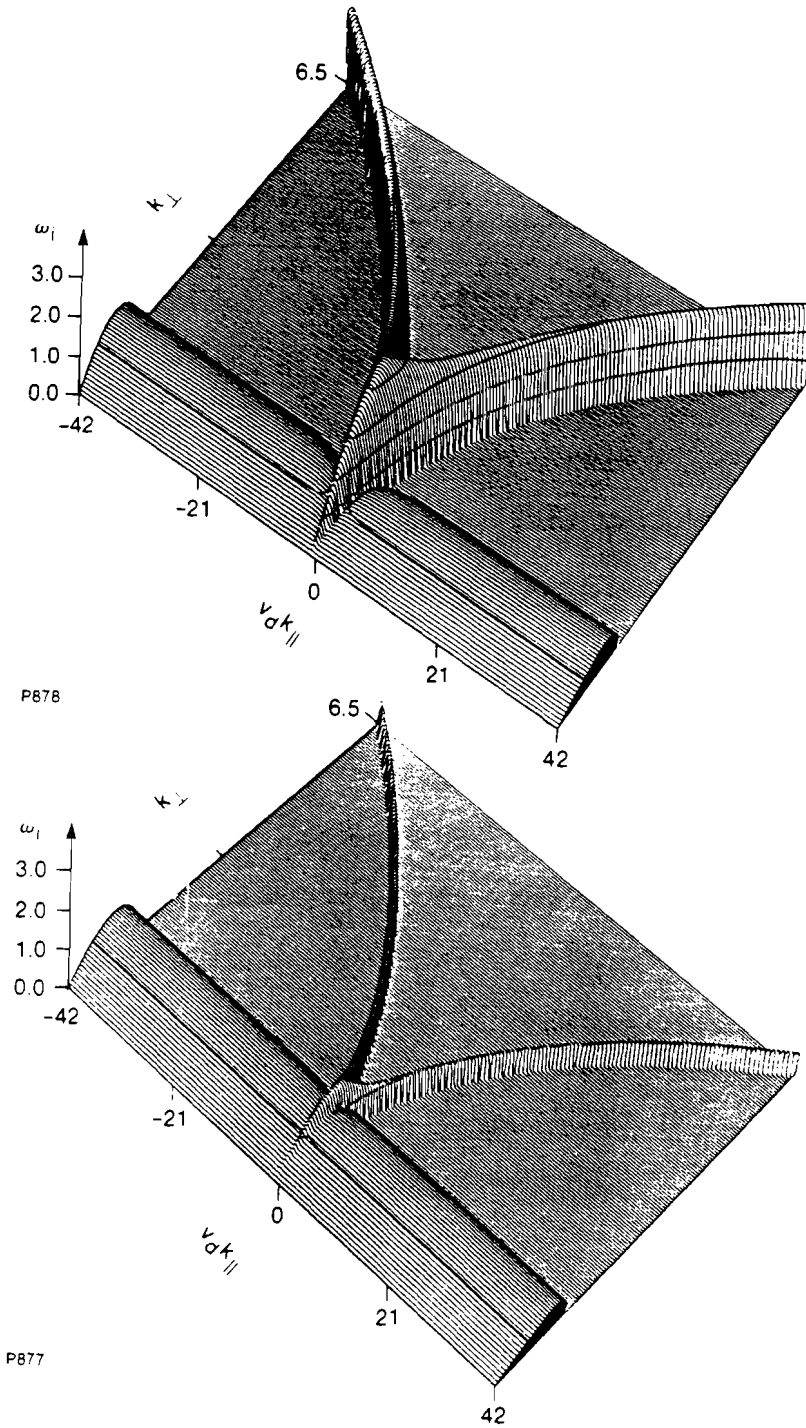


Figure 3.3: The imaginary part of the dispersion surface $\omega(k_{\parallel}, k_{\perp})$ is displayed as a function of the longitudinal and the transverse wavenumber for two values of the pump intensity ratio R . In the upper figure $R = 1.0$, and in the lower $R = 0.1$. The instability branch due to the cooperative action has the largest growth rate for both values of R .

the solutions of the coupled-wave dispersion equation reduce to

$$\omega \approx (v_s \pm v_d)k_{\parallel} \pm i[\sigma_{\perp}k_{\perp}^2(2 - \sigma_{\perp}k_{\perp}^2)]^{1/2}. \quad (3.51)$$

This single-wave limit can be obtained more easily from Eq. (3.47) than from Eq. (3.50). However, the most striking feature of the dispersion surface is that instability exists for transverse wavenumbers which are larger than $[2(1 + |\epsilon|)]^{1/2}$; the region of k_{\perp} -space corresponding to unstable amplitude perturbations is *unbounded*. For large values of the transverse wavenumber, equilibrium (3.39) is modulationally unstable with respect to amplitude perturbations whose longitudinal wavenumbers satisfy

$$k_{\perp}^2(k_{\perp}^2 - 2\sigma_{\perp} - 2|\epsilon|) < (v_d k_{\parallel})^2 < k_{\perp}^2(k_{\perp}^2 - 2\sigma_{\perp} + 2|\epsilon|). \quad (3.52)$$

For each value of the transverse wavenumber, the maximal temporal growth rate is approximately equal to $|\epsilon|$ and corresponds to an optimal longitudinal wavenumber of approximately $(k_{\perp}^2 - \sigma_{\perp})/v_d$. The range of longitudinal wavenumbers corresponding to modulational instability has a width of approximately $2|\epsilon/v_d|$. The instability of amplitude perturbations with large transverse wavenumbers has been established for the special case of counterpropagating waves by Vlasov and Talanov [44], and Firth and Paré [46]. However, it should be emphasized that this phenomenon is more general; it occurs for two colinear waves of unequal group velocities, regardless of their relative directions of propagation. It is, of course, essential to know how large v_d must be in order for the branch of the modulational instability at large transverse wavenumbers to exist. The coupled nonlinear Schroedinger equations (2.15) were derived under the assumption that the longitudinal envelope wavenumbers are much smaller than the transverse envelope wavenumbers. The requirement that this assumption be self-consistent, together

with Eq. (3.52), leads to the restrictions

$$|(v_1 - v_2)/v_1| \gg |k_\perp/k_1|, \quad |(v_1 - v_2)/v_2| \gg |k_\perp/k_2| \quad (3.53)$$

on the physical variables. The condition

$$|k_\perp| \gg (\lambda_{11}/\mu_\perp)^{1/2}|A_1| \quad (3.54)$$

must be satisfied simultaneously, in order that the transverse wavenumber lie outside the range of wavenumbers corresponding to the modulational instability of two copropagating waves. Conditions (3.53) and (3.54) are consistent with the intuitive notion that the difference in group velocities can be neglected when the dispersive portions of the convective terms are much smaller than the nonlinear terms which make possible the instability. The imaginary part of the dispersion surface is displayed for the case in which $R = 0.1$ in the lower part of Fig. 3.3. Notice that the branch of the modulational instability at large transverse wavenumbers still exists, albeit with reduced strength. It is shown in the Appendix that, for large values of the transverse wavenumber, the longitudinal wavenumbers corresponding to modulational instability satisfy the inequality

$$[k_\perp^2 - \frac{1}{2}\sigma_\perp(1 + r^2) - |\epsilon|r] < |v_d k_\parallel| < [k_\perp^2 - \frac{1}{2}\sigma_\perp(1 + r^2) + |\epsilon|r] \quad (3.55)$$

approximately. When R is equal to unity, conditions (3.52) and (3.55) differ by terms of order k_\perp^{-2} , which are small by assumption. The maximal temporal growth rate is approximately equal to $|\epsilon|r$ and corresponds to an optimal longitudinal wavenumber of approximately $[k_\perp^2 - \frac{1}{2}\sigma_\perp(1 + r^2)]/v_d$.

In practice, however, the initial perturbations are rarely sinusoidal and a predictive capability must be developed for the spatio-temporal evolution of arbitrary initial perturbations. Fortunately, if the response of a linear system to a point

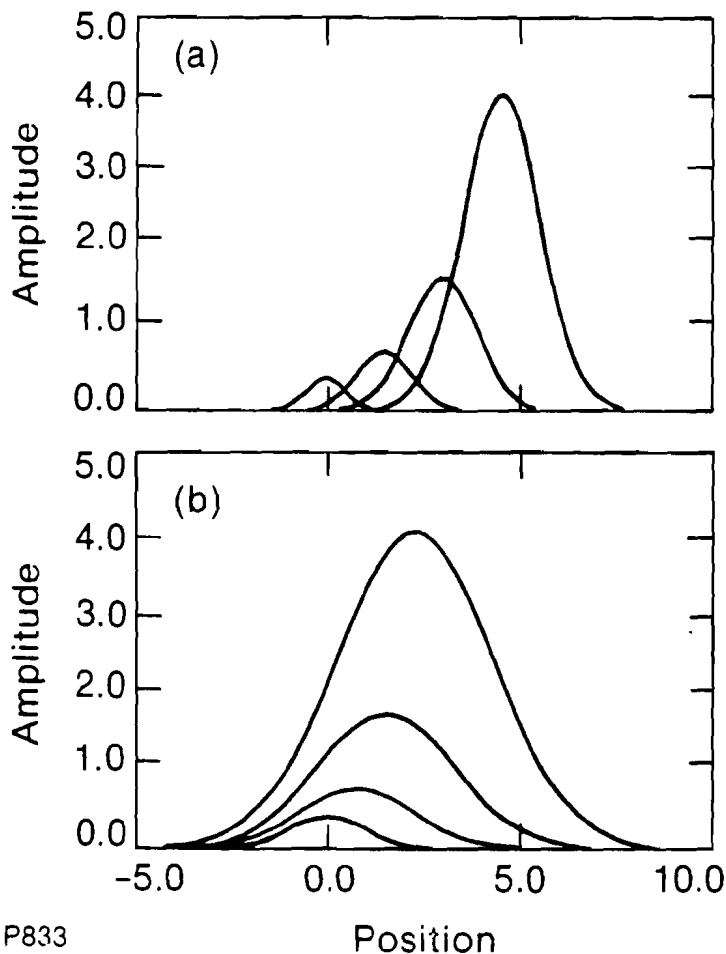


Figure 3.4: The impulse response of a linear system is plotted as a function of position, at several successive times. (a) The linear system is convectively unstable. (b) The linear system is absolutely unstable.

source is known, the response of that system to an arbitrary source can be constructed by convolution. In general, a linear system can respond in two different ways to a source which is localized in both space and time, as shown in Fig. 3.4. If the leading and trailing edge of a growing response travel in the same direction, the system is convectively unstable. If the leading and trailing edge of a growing response travel in opposite directions, the system is absolutely unstable. Clearly, the distinction between the two types of instability depends on the reference frame

from which the instability is observed. However, in any particular situation there is always a privileged reference frame from which the instability is to be studied. For the applications which motivated this paper, the nonlinear medium that makes the TMI possible is at rest in the laboratory frame. While absolute instabilities are generally considered more harmful to the underlying optical application than convective instabilities, because they grow in time and do not convect out of the affected region, there may exist convective instabilities whose trailing edges travel so slowly that they are effectively absolute. In general, one must carefully evaluate the nature of the impulse response on the space and time scales relevant to the underlying optical application.

The absolute or convective nature of the instability can be determined by investigating the singularities of the transformed Green function, even when the integrals in the expression for the inverse Fourier–Laplace transform are intractable. These singularities generally occur for the zeroes of the dispersion function, and, as usual, the existence of complex values of the frequency for real values of the wavenumber implies that the solution can be unstable. In cases where there are no branch-point singularities or other pathological properties of the integrand, the Laplace inversion contour can be analytically continued to the real axis. Unstable systems for which the Laplace contour can be analytically continued are convectively unstable; the perturbations in wave amplitude convect more quickly than they grow and no temporal growth is observed in the laboratory frame. During the process of analytically continuing the Laplace inversion contour, double roots in wavenumber space can pinch the Fourier inversion contour. These pinching roots map into branch points in frequency space and prevent further analytic continuation of the Laplace contour. Unstable systems in which these pinching poles occur are absolutely unstable; the perturbations in wave amplitude grow more quickly

than they convect and temporal growth is observed in the laboratory frame. This element of linear stability analysis is documented by several reviews in the fluids and plasma-physics literature [22 – 24].

Hall and Heckrotte [71] derived a set of ordinary differential equations that determine the path of pinching poles as the velocity parameter of a Galilean transformation is varied. This technique was subsequently extended, to allow for relativistic observation-frame velocities and Lorentz transformations, by Bers, Ram and Francis [72]. Typically, the Hall–Heckrotte technique is used to plot the temporal growth rate of the most unstable mode as a function of the observation-frame velocity. By scaling both axes with time, such a plot can be interpreted as the asymptotic response of the system to a point source. [To be precise, the asymptotic impulse response is the product of the cumulative gain and the source function (3.43) on which it acts.] An absolutely-unstable impulse response is characterized by a finite temporal growth rate in the laboratory frame. These impulse-response curves can be constructed for a series of values of the pump-wave intensity ratio R , to study how the stability properties of the coupled-wave system depend on this parameter.

For the TMI of a single wave (or two copropagating waves), the impulse-response curve is a δ -function of unit height centered on the (common) linear group velocity v_s . This result has a simple physical explanation. Consider the evolution of a filament with a specified k_\perp and initial depth profile. Since the temporal growth rate is independent of k_\parallel , all Fourier components of the source are amplified at the same rate. Furthermore, since ω and k_\parallel only enter in the characteristic combination $\omega - v_s k_\parallel$, the longitudinal evolution of the filament is dispersionless; *any* initial profile, and not just a point source, will propagate isomorphically with velocity v_s . This is why the linearized equations could be

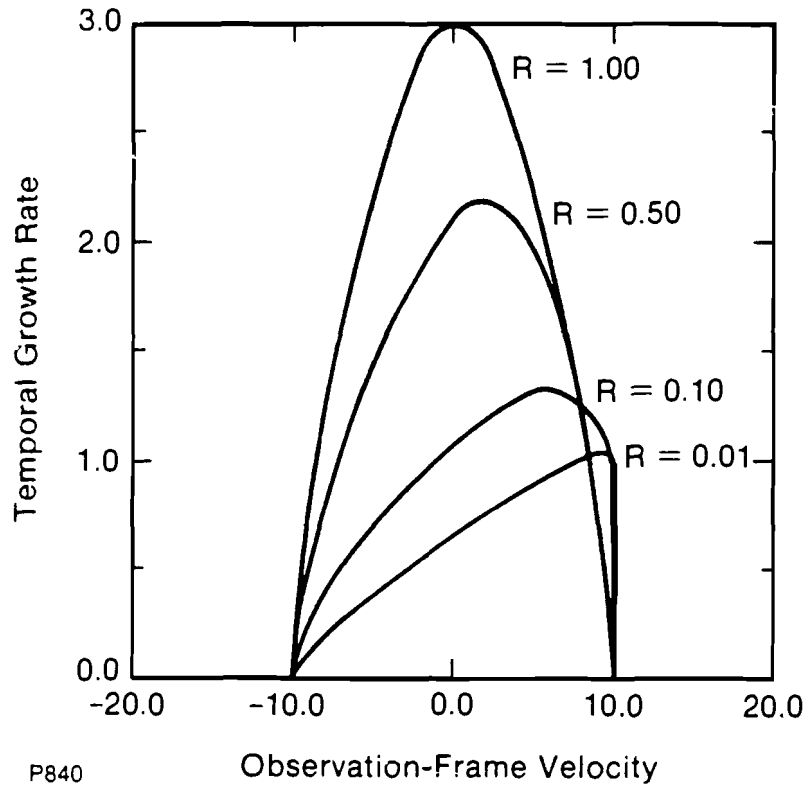
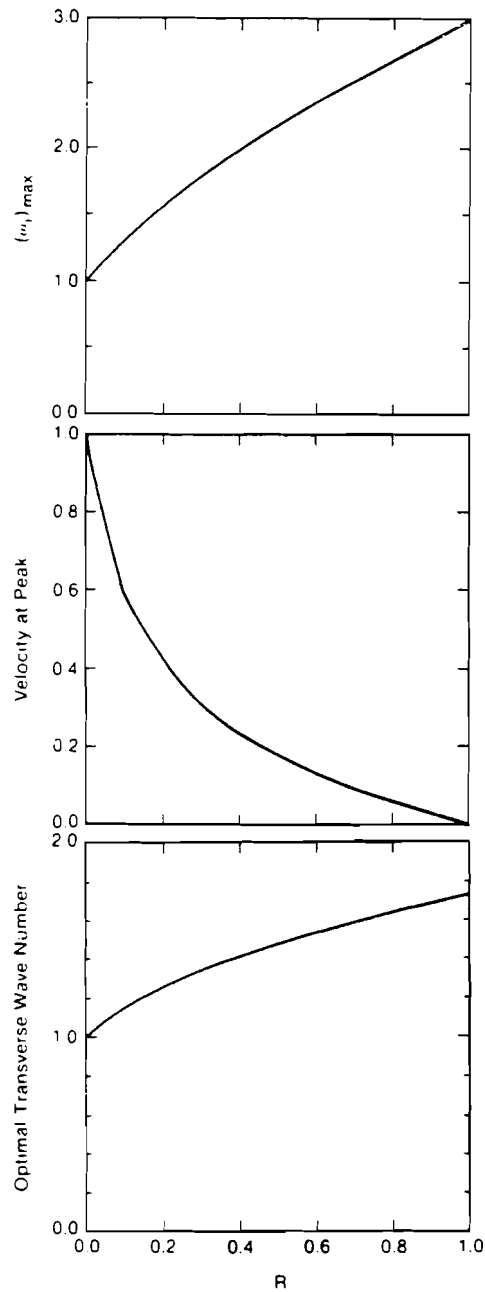


Figure 3.5: The impulse response curves of the TMI due to two colinear waves are displayed for several values of the backward to forward pump intensity values, R , where $\sigma_{\perp} = 1$, $\epsilon = 2$ and $v_d = 10$. The observation-frame velocity is measured relative to v_s .

solved using the method of characteristics in Sec. 3.1.

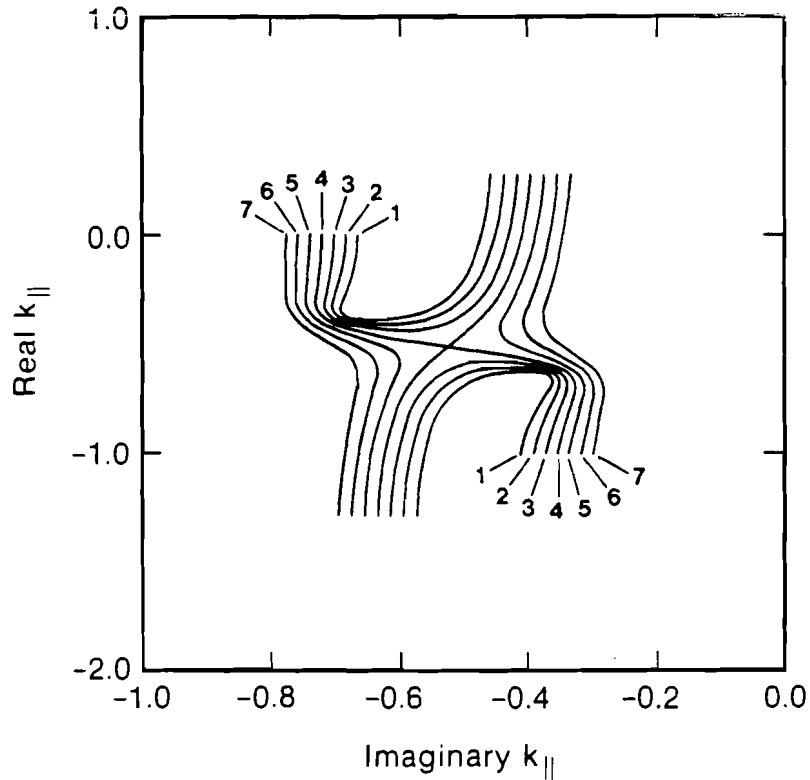
Consider the TMI of two unstable waves for which $\sigma_{\perp} = 1$ and $\epsilon = 2$. The temporal growth rate of the impulse response is plotted as a function of observation-frame velocity in Fig. 3.5, for several values of R . When R is equal to unity, the impulse response is centered on the average group velocity v_s and has a peak growth rate of 3.0, corresponding to an optimal transverse wavenumber of 1.7. Thus, the growth rate of the cooperative process γ_c is 3γ and $\lambda_{\perp c} = \lambda_{\perp}/1.7$. As R decreases to zero, the peak growth rate decreases monotonically to its single-wave value of 1.0, the optimal transverse wavenumber decreases monotonically

to its single-wave value of 1.0 and the impulse response becomes skewed towards the group velocity of wave 1, as shown in Fig. 3.6. However, the coupled-wave impulse-response curve does not tend to the single-wave impulse-response curve, which is a δ -function centered on the group velocity of wave 1, as R tends to zero. This curious behavior warrants further investigation. An inspection of the coupled-wave dispersion function (3.45) shows that pinching poles exist when R is exactly equal to zero. However, the source function (3.43) contains a factor of the single-wave dispersion function (3.44) which eliminates the spurious root from the integrand of Eq. (3.42). Thus, the predictions of Eqs. (3.42) – (3.45) are correct when R is equal to zero. When R is small, but finite, pinching poles still exist. Figure 3.7 shows the pole structure in an observation frame moving with velocity v_s , for the case in which $R = 0.01$. This saddle-point structure is typical for pinching poles. Since the poles do pinch the Fourier contour, the temporal growth implied by the corresponding impulse-response curve in Fig. 3.5 is genuine. However, the true impulse response is the product of the cumulative gain and the source function on which it acts; the common practice of characterizing the impulse response of a linear system solely by the associated temporal growth rates is inadequate for this particular wave interaction. The dispersion function of wave 2, evaluated at the saddle-point frequencies and wavenumbers of Fig. 3.5, is plotted as a function of R in Fig. 3.8. It follows that the source function (3.43) tends to zero as R tends to zero. Thus, although temporal growth is observed in a frame moving with velocity v_s , the time taken for the impulse response to grow to an appreciable magnitude tends to infinity as R tends to zero. In this sense, the coupled-wave impulse response *does* tend continuously to the single-wave impulse response as R tends to zero. An important feature of Fig. 3.5 is that the coupled-wave impulse response is confined to the region bounded



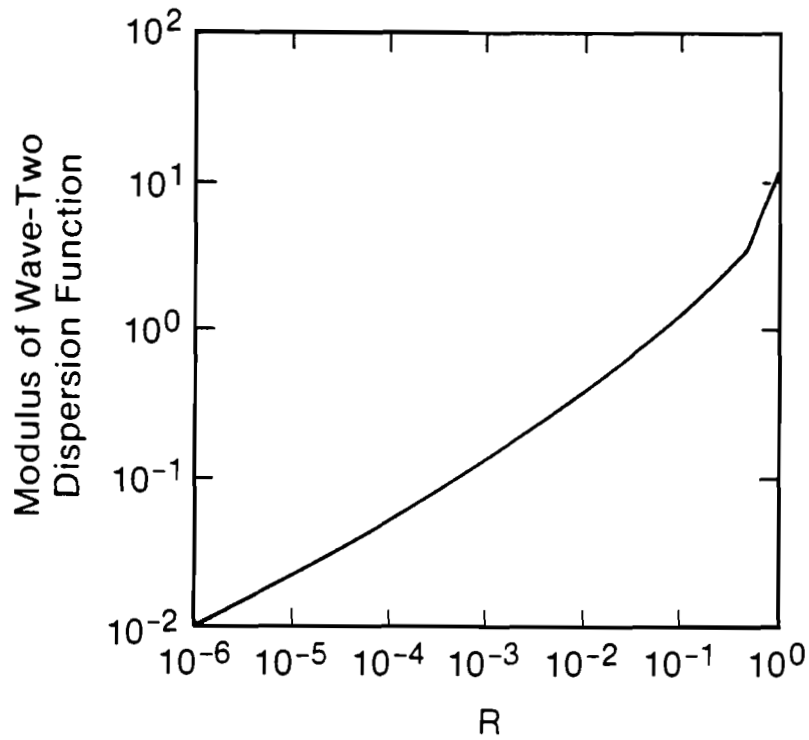
P845

Figure 3.6: The growth rate (a), velocity (b), and transverse wave number (c) at the peak of the impulse response curves are plotted as functions of the intensity ratio R for the parameters given in Fig. 3.5. The velocity of the peak of the impulse response is measured relative to v_s and normalized to $v_d = 10$.



P841

Figure 3.7: The pole structure in the complex plane of the longitudinal wavenumber is shown for an intensity ratio R of 0.1 and a reference-frame velocity of v_s . Seven fixed values of the real part of the frequency are mapped into this complex wavenumber space by the coupled dispersion equation as the imaginary part of the frequency is varied between zero and twice the maximally unstable value. The imaginary parts of the frequency are zero at the annotated ends, and their real parts increase in equally spaced steps starting with the lines labeled 1. The lines labeled 4 contains the pinching pole. The paths for the other pair of roots are not shown.



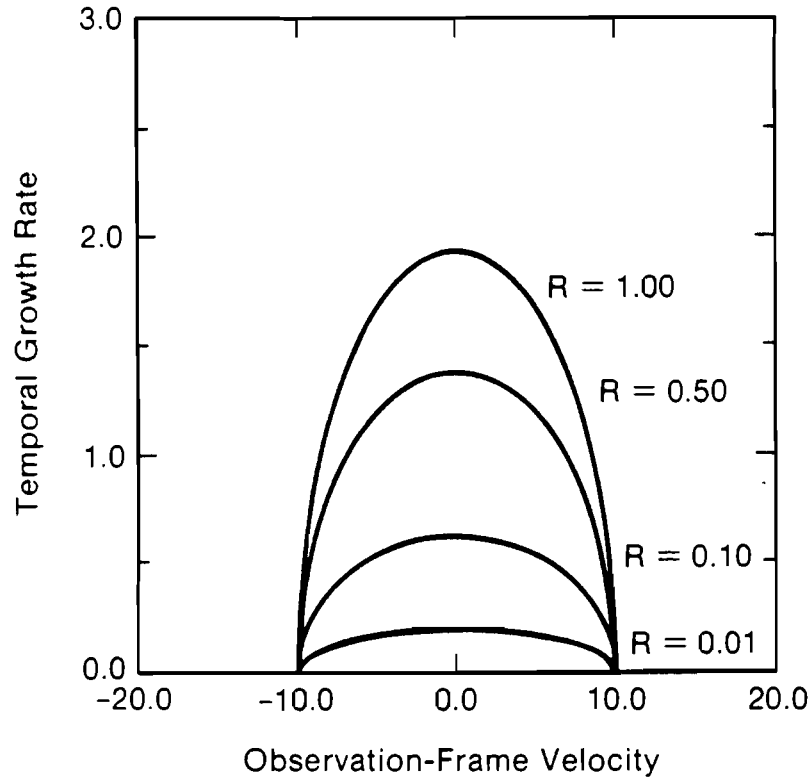
P884

Figure 3.8: The modulus of the single-wave dispersion function $D_2(\omega, k_{\parallel}, k_{\perp})$, evaluated at the pinch-point frequencies and wave vectors in an observation frame moving with velocity v_s , are plotted as functions of R . It follows that the source function (3.43) tends to zero as R tends to zero, for arbitrary initial conditions.

by the uncoupled group velocities v_1 and v_2 . Thus, the coupled-wave system is absolutely unstable whenever the product $v_1 v_2$ is negative.

Now consider the interaction of two stable waves for which σ_{\perp} is equal to -1 and ϵ equal to 2. The imaginary part of the dispersion surface can be inferred from Fig. 3.3 by omitting the single-wave features located at small values of the transverse wavenumber. Equations (3.52) and (3.55), and the discussion of their implications, are also relevant to the interaction of two stable waves. In particular, perturbations in wave amplitude are modulationally unstable for large values of the transverse wavenumber, with a maximal temporal growth rate of $|\epsilon|r$. The temporal growth rate of the impulse response is plotted as a function of observation-frame velocity in Fig. 3.9, for several values of R . A typical transverse wavenumber of 5.3, at which the peak temporal growth rates are near their maximal value, was used throughout the figure. Notice that the impulse response is no longer finite as R tends to zero, because the single-wave branch of the modulational instability no longer exists. The unstable impulse response is due solely to the coupling between the waves and is centered on the average group velocity v_s . (A similar component of the impulse response exists for the case in which $\sigma_{\perp} = 1$. However, it is not the dominant component and was, therefore, omitted from Fig. 3.6.) Once again, if the product $v_1 v_2$ is negative, the coupled-wave system is absolutely unstable for all nonzero values of R . However, in contrast to the case studied previously, the peak temporal growth rate of the impulse response tends to zero as R tends to zero, as shown in Fig. 3.10.

In both cases discussed above, the values of the maximal temporal growth rate and optimal transverse wavenumber of the coupled-wave instability are larger than the corresponding single-wave values, even when the pump-wave intensity ratio R is small. Thus, the coupled-wave instability always grows more quickly and



P839

Figure 3.9: The impulse response curves of the TMI for two colinear waves are displayed for the case in which $\sigma_{\perp} = -1$, $\epsilon = 2$ and $v_d = 10$. The dimensionless transverse wavenumber $k_{\perp} = 5.3$, for all values of the intensity ratio, R , and the observation-frame velocity is measured relative to v_s .

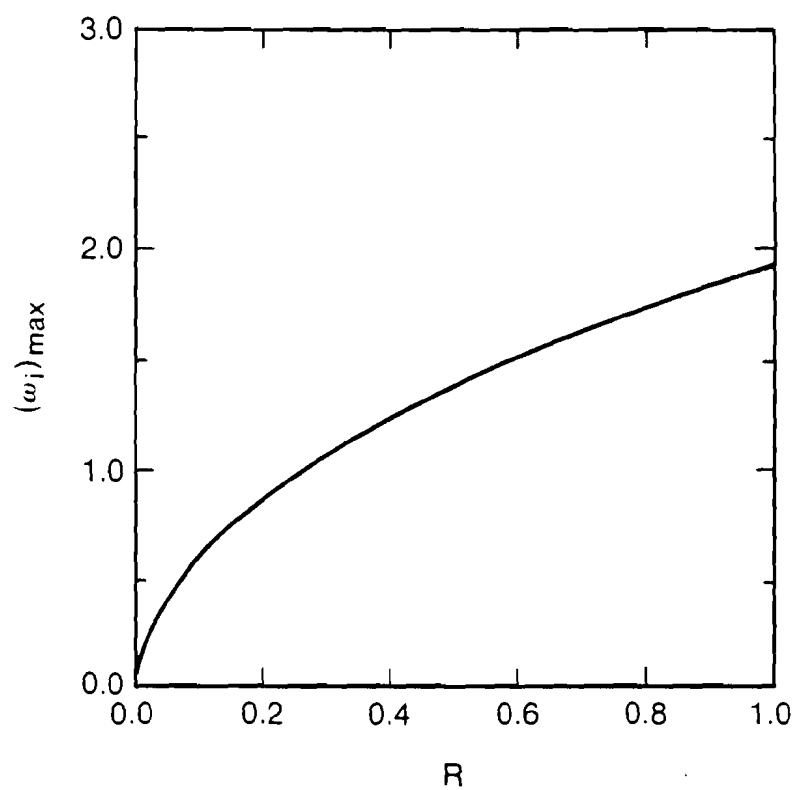


Figure 3.10: The peak temporal growth rate of the impulse response is plotted as a function of the intensity ratio R , for the parameters given in Fig. 3.9.

supports narrower filaments than does the single-wave instability.

Finally, the effects of equal wave damping on the perturbations in wave amplitude can be inferred from the preceding results by making the substitution $\omega_i \rightarrow \omega_i - \nu$. However, as noted in Sec. 3.1, this substitution gives only a crude estimate of the effects of wave damping.

3.3 Summary

In this chapter, the TMI of two colinear waves was studied. In general, the waves are modulationally unstable with a maximal temporal growth rate which is larger than that of either wave alone and a range of unstable transverse wavenumbers which is broader than that of either wave alone. Moreover, waves which are modulationally stable by themselves are often unstable in the other's presence. This is true for both copropagating and counterpropagating waves. The TMI of copropagating waves is always convective. The TMI of counterpropagating waves in infinite media is absolute for arbitrary values of the pump-wave intensity ratio, although the instability growth rate does depend on this ratio. Because of its novelty and its potential for adverse effects in applications, the analysis in the following chapters will be focused on understanding the TMI of counterpropagating waves.

Appendix 3: Four-Wave Interactions in Infinite Media

The linearized versions of Eqs. (2.15) describe implicitly the interaction of the + and - sidebands of wave 1, corresponding to transverse variations in perturbed wave amplitude of $\exp(\pm ik_1 x)$, respectively, with the + and - sidebands

of wave 2. The sideband evolution can be made explicit by making the substitutions

$$A_1^{(1)}(t, z)\phi(\vec{x}_\perp) \longrightarrow A_1^{(+)}(t, z)\exp(ik_\perp x) + A_1^{(-)}(t, z)\exp(-ik_\perp x), \quad (3A.1)$$

$$A_2^{(1)}(t, z)\phi(\vec{x}_\perp) \longrightarrow A_2^{(+)}(t, z)\exp(ik_\perp x) + A_2^{(-)}(t, z)\exp(-ik_\perp x), \quad (3A.2)$$

in the perturbation ansatz and linearizing Eqs. (2.15) accordingly. The interaction of the + and - sidebands of wave 1 is known as the transverse modulational instability of wave 1 and is nonresonant. For large values of the transverse wavenumber, this interaction and the corresponding interaction for wave 2 are weak and can be neglected. However, providing that v_1 is not equal to v_2 , the interaction of the + sideband of wave 1 with the - sideband of wave 2 is resonant for arbitrary values of the transverse wavenumber (as will be demonstrated shortly) and must always be retained in the stability analysis. This four-wave interaction is governed by the equations

$$\begin{aligned} (\partial_t + v_1\partial_z + i\delta_1)A_1^{(+)} - ic_{12}A_2^{(-)*} &= 0, \\ (\partial_t + v_2\partial_z - i\delta_2)A_2^{(-)*} + ic_{21}A_1^{(+)} &= 0, \end{aligned} \quad (3A.3)$$

where the frequency-mismatch coefficients

$$\delta_1 = \mu_\perp k_\perp^2 - \lambda_{11}|A_1|^2, \quad \delta_2 = \mu_\perp k_\perp^2 - \lambda_{22}|A_2|^2, \quad (3A.4)$$

and the coupling coefficients

$$c_{12} = \lambda_{12}|A_1A_2|, \quad c_{21} = \lambda_{21}|A_2A_1|, \quad (3A.5)$$

and is linearly independent of the corresponding interaction of the - sideband of wave 1 with the + sideband of wave 2. For the special case in which the pump

waves propagate in opposite directions, the four-wave interaction described by Eqs. (3A.3) is known as phase conjugation.

Subject to the initial conditions

$$A_1^{(+)}(0, z) = F_+(z) , \quad A_2^{(-)*}(0, z) = F_-(z) , \quad (3A.6)$$

the solution of Eqs. (3A.3) for the + sideband can be written as

$$A_1^{(+)}(t, z) = \int_F \int_L \frac{S_+(\omega, k_{\parallel}, k_{\perp})}{D(\omega, k_{\parallel}, k_{\perp})} \exp[i(k_{\parallel}z - \omega t)] d\omega dk_{\parallel} \quad (3A.7)$$

where the source function

$$S_+(\omega, k_{\parallel}, k_{\perp}) = i[(\omega - v_2 k_{\parallel} + \delta_2)F_+(k_{\parallel}) - c_{12}F_-(k_{\parallel})]/2\pi , \quad (3A.8)$$

the dispersion function

$$D(\omega, k_{\parallel}, k_{\perp}) = (\omega - v_1 k_{\parallel} - \delta_1)(\omega - v_2 k_{\parallel} + \delta_2) + \gamma^2 \quad (3A.9)$$

and the coupling term

$$\gamma^2 = c_{12}c_{21} . \quad (3A.10)$$

The expression for $A_2^{(-)*}(t, z)$ is similar. Henceforth, the subscript \parallel will be omitted.

It follows from Eqs. (3A.7) and (3A.9), that perturbations in wave amplitude which are initially sinusoidal in the z -direction remain so, with a temporal growth rate given by the formula

$$2\omega = (v_1 k + \delta_1) + (v_2 k - \delta_2) \pm \left([(v_1 k + \delta_1) + (v_2 k - \delta_2)]^2 - 4\gamma^2 \right)^{1/2} . \quad (3A.11)$$

Thus, the longitudinal wavenumbers corresponding to unstable perturbations in wave amplitude satisfy the inequality

$$-(\delta_1 + \delta_2) - 2\gamma < (v_1 - v_2)k < -(\delta_1 + \delta_2) + 2\gamma . \quad (3A.12)$$

For a point source and the dispersion function (3A.9), the integrals in Eq. (3A.7) can be evaluated exactly in terms of Bessel functions. However, it is sufficient, for the purposes of this paper, to determine the time-asymptotic impulse response. For exact frequency matching, Eqs. (3A.3) reduce to the standard wave-coupling equations. Thus, the determination of the time-asymptotic impulse response requires only minor modifications of the standard analysis described by Briggs [22]. Regarded as a function of frequency, the longitudinal wavenumber is given by the formula

$$2v_1v_2k = v_2(\omega - \delta_1) + v_1(\omega + \delta_2) \pm \left([v_2(\omega - \delta_1) - v_1(\omega + \delta_2)]^2 - 4v_1v_2\gamma^2 \right)^{1/2}. \quad (3A.13)$$

The longitudinal wavenumber is a double root of the dispersion equation whenever the discriminant in Eq. (3A.13) is equal to zero. This occurs for values of the frequency given by

$$\omega_* = -\frac{v_1\delta_2 + v_2\delta_1}{v_1 - v_2} \pm \frac{2\gamma(v_1v_2)^{1/2}}{v_1 - v_2}. \quad (3A.14)$$

The corresponding values of the longitudinal wavenumber are

$$k_* = -\frac{\delta_2 + \delta_1}{v_1 - v_2} \pm \frac{2\gamma(v_1 + v_2)}{(v_1v_2)^{1/2}(v_1 - v_2)}. \quad (3A.15)$$

To obtain the saddle-point frequencies and wavenumbers in a Galilean frame of observation, moving with constant speed relative to the source, one simply has to replace ω_* , k_* , v_1 and v_2 in Eqs. (3A.14) and (3A.15) by their transformed counterparts $\bar{\omega}_*$, \bar{k}_* , \bar{v}_1 and \bar{v}_2 , respectively. It follows, from Eq. (3A.14), that $\bar{\omega}_*$ will have a positive imaginary part whenever γ is nonzero and the product $\bar{v}_1\bar{v}_2$ is negative. Moreover, as the imaginary part of $\bar{\omega}_*$ tends to infinity, the two solutions \bar{k}_\pm of Eq. (3A.13) lie on opposite sides of the real \bar{k} -axis. Thus, as $\bar{\omega}$ approaches the saddle-point frequencies, the roots \bar{k}_\pm pinch the Fourier contour between them and *do* contribute to the impulse response. In terms of the sum

and difference velocities

$$v_s = \frac{1}{2}(v_1 + v_2) , \quad v_d = \frac{1}{2}(v_1 - v_2) , \quad (3A.16)$$

the observation-frame frequencies and wavenumbers can be expressed as

$$\begin{aligned} \bar{\omega}_*(v_s + v) &= \frac{1}{2}[(\delta_1 - \delta_2) + (v/v_d)(\delta_1 + \delta_2)] \pm i\gamma[1 - (v/v_d)^2]^{1/2} , \\ v_d \bar{k}_*(v_s + v) &= -\frac{1}{2}(\delta_1 + \delta_2) \pm i\gamma(v/v_d)[1 - (v/v_d)^2]^{-1/2} , \end{aligned} \quad (3A.17)$$

respectively, where v is the velocity of the observation frame measured relative to the average group speed of the waves. In particular, notice that

$$\bar{\omega}_*(v_s) = \frac{1}{2}(\delta_1 - \delta_2) \pm i\gamma , \quad v_d \bar{k}_*(v_s) = -\frac{1}{2}(\delta_1 + \delta_2) . \quad (3A.18)$$

There are a number of interesting features to solutions (3A.17). First, the imaginary part of $\bar{\omega}_*$ is maximal in a frame moving with speed v_s and decreases to zero parabolically as v tends to $\pm v_d$. Thus, the impulse response grows most rapidly in a frame moving with the average group velocity v_s and is bounded by the uncoupled group velocities v_1 and v_2 . Second, the imaginary part of \bar{k}_* corresponding to the unstable component of the impulse response has the same sign as v . This reflects the fact that the impulse response is a decreasing function of position ahead of its peak and an increasing function of position behind its peak. Third, the real parts of $\bar{\omega}_*$ and \bar{k}_* adjust themselves to compensate completely for the initial phase mismatch and, consequently, the imaginary parts of $\bar{\omega}_*$ and \bar{k}_* are independent of δ_1 and δ_2 . Thus, the interaction of the + sideband of wave 1 with the – sideband of wave 2 is resonant, as stated earlier.

The corresponding results, for the interaction of the + sideband of wave 2 with the – sideband of wave 1, can be inferred from the results described above by interchanging the subscripts 1 and 2. One consequence of this exchange is that

the term $v_1 - v_2$ changes sign and inequality (3A.12) becomes

$$(\delta_1 + \delta_2) - 2\gamma < (v_1 - v_2)k < (\delta_1 + \delta_2) + 2\gamma . \quad (3A.19)$$

Thus, one sideband interaction is unstable for positive values of the longitudinal wavenumber while the other sideband interaction is unstable for negative values of the longitudinal wavenumber. By rescaling all variables according to Eq. (3.46), Eqs. (3A.12) and (3A.19) can be rewritten in the form of Eq. (3.55) of the main text.

Chapter 4

Counterpropagating Light Waves in Finite Media

In Chapter 3 it was shown that the transverse modulational instability (TMI) of coupled colinear waves need not act as the superposition of the associated single-wave instabilities. Instead, the cooperative TMI arises having both qualitatively and quantitatively different characteristics. In either the copropagating or the counterpropagating case the growth rate spectrum acquires a branch due to the cooperative interaction of the pumps. In the counterpropagating case the maximum growth rate is larger than twice the single-wave growth rate and the cooperative instability is absolute. This absolute instability is of particular importance in finite media since its growth need not be restricted by the length of the medium. In media of finite length, cooperative absolute instabilities have nonzero intensity thresholds, even in the absence of damping. In this chapter we analyze the cooperative TMI of counterpropagating light waves in a finite cubically nonlinear medium.

Several mechanisms by which counterpropagating waves interact may be understood in terms of four-wave mixing (FWM) processes which occur between counterpropagating pump waves and their electromagnetic sidebands. Small am-

plitude electromagnetic sidebands may arise as a result of noise or by injection from an external source. These sidebands may beat with either of the counterpropagating pump fields driving refractive index gratings in the medium. The pump fields may then scatter from these gratings, enhancing the sidebands. Through this process these gratings couple the counterpropagating pumps and allow them to exchange energy with their sidebands. The sidebands that exchange energy most efficiently with the pump fields satisfy the optimal phase-matching conditions. These conditions require that the geometric orientation of the wave vectors of the sidebands and the magnitude and sign of their frequency shifts balance the nonlinear phase shifts. Thus, of all the possible combinations of modes, a distinct set of sidebands which satisfy the optimal phase matching conditions will be selected by the system of interacting waves. In many cases, these favored sidebands are described as FWM interactions and correspond to instabilities.

The introduction of a second counterpropagating light wave increases the number of couplings among the pumps and their sidebands, allowing several distinct FWM interactions to coexist. If two simultaneously phase-matched FWM interactions drive the same grating [73], hybrid instabilities may arise and single-wave instabilities may be enhanced. A hybrid TMI branch is formed through the interaction of three FWM interactions [50] which are simultaneously phase matched in the presence of a second counterpropagating light wave. Since this hybrid branch requires the interaction of more than one pump and manifests itself as more than simply the superposition of the three simpler interactions, it is a cooperative instability.

Let a pair of intense, counterpropagating light waves, of frequency ω_0 and wave vector $\pm\vec{k}_0$ irradiate opposite ends of a uniform plasma of length L . The amplitude of the intense pump wave injected at the left (right) end of the plasma shall be

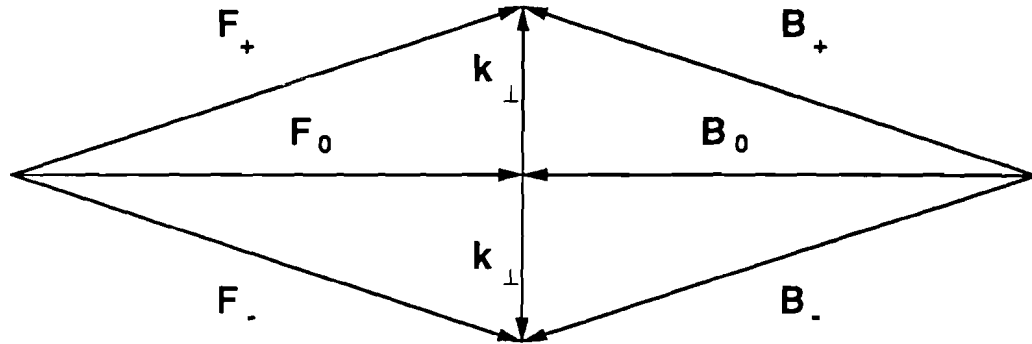


Figure 4.1: The wave vector matching diagram for the four-sideband interaction.

\vec{F}_0 (\vec{B}_0). Each pump wave has two sidebands: one Stokes shifted with frequency $\omega_0 - \omega^*$ and wave vector $\pm \vec{k}_0 - \vec{k}$, and one anti-Stokes shifted with frequency $\omega_0 + \omega$ and wave vector $\pm \vec{k}_0 + \vec{k}$. Thus, a small-amplitude anti-Stokes sideband F_+ which has frequency $\omega_0 + \omega$ and wave vector $\vec{k}_0 + \vec{k}_\perp$ couples most strongly to the three other coplanar sidebands shown in Fig. 4.1. It couples with the Stokes-shifted sideband F_- as a result of a forward FWM process, which gives rise to the single-wave TMI. It couples with the Stokes-shifted sideband B_- as a result of a backward FWM mixing process which is a phase conjugation interaction, and it couples with the anti-Stokes sideband B_+ as a result of a second backward FWM interaction which is Bragg reflection.

In general, this four-sideband interaction includes forward, side and backward scattering. By requiring that all six waves be linearly polarized in the same direction and that the transverse perturbation wave number satisfy the inequality $|\vec{k}_\perp|/|\vec{k}_0| \ll 1$ only the most important near-forward and near-backward scattering instabilities are treated. An investigation of the three-dimensional instabilities of counterpropagating waves which includes side scattering and arbitrary polariza-

tion vectors has confirmed the validity of this approximation and can be found in Ref. [74].

The phase-matched interaction of the two counterpropagating pumps with these four sidebands gives rise to a cooperative, *four-sideband*, TMI. This four-sideband interaction occurs in a localized region of the parameter space spanned by the transverse perturbation wave number and the frequency shift of the sidebands [55]. As it is detuned from its optimal phase matching condition, three two-sideband interactions are recovered. In the limit where the frequency shift of the sidebands is large, only forward FWM interactions are phase matched. In the limit where the transverse component of the wave vector of the sidebands is large, only phase conjugate interactions are phase matched. Finally, in the limit where both parameters are large, only Bragg scattering by FWM is phase matched. The four-sideband instability occurs in the spectral overlap region of these three two-sideband interactions. The four-sideband instability can have a larger convective growth rate and a lower absolute instability threshold than any of the instabilities which occur in these two-sideband limits for either self-focusing or self-defocusing media. Thus, the four-sideband TMI can dominate the interaction of the two counterpropagating waves.

When the growth of a finite set of sidebands is favored, the system of interacting modes governed by the coupled nonlinear Schroedinger equations can be truncated. This truncation yields the four-sideband model of the counterpropagating-wave system. It is obtained by perturbing an equilibrium solution of the nonlinear Schroedinger equations with four sidebands. One equilibrium solution of the coupled nonlinear Schroedinger equations is independent of time and the transverse

spatial dimension,

$$A_1^{(0)} = F_0 \exp(i\Delta_F z) , \quad (4.1)$$

$$A_2^{(0)} = B_0 \exp(-i\Delta_B(z - L)) , \quad (4.2)$$

where

$$\Delta_F = \lambda(|F_0|^2 + \epsilon|B_0|^2)/v , \quad (4.3)$$

$$\Delta_B = \lambda(\epsilon|F_0|^2 + |B_0|^2)/v , \quad (4.4)$$

and $k_0 = k_1^{(0)} = -k_2^{(0)}$, $v = v_1 = -v_2$, $\lambda = \lambda_{11} = \lambda_{22}$, $\lambda_{21} = \lambda_{12}$ and $\epsilon = \lambda_{12}/\lambda$.

When these solutions are perturbed by a set of four sidebands,

$$\begin{aligned} A_1 = & [F_0 + F_+(z, t) \exp(i\vec{k}_\perp \cdot \vec{r}_\perp) \\ & + F_-(z, t) \exp(-i\vec{k}_\perp \cdot \vec{r}_\perp)] \exp(i\Delta_F z) , \end{aligned} \quad (4.5)$$

$$\begin{aligned} A_2 = & [B_0 + B_+(z, t) \exp(i\vec{k}_\perp \cdot \vec{r}_\perp) \\ & + B_-(z, t) \exp(-i\vec{k}_\perp \cdot \vec{r}_\perp)] \exp(-i\Delta_B(z - L)) , \end{aligned} \quad (4.6)$$

where $|F_0|, |B_0| \gg |F_\pm|, |B_\pm|$, and each sideband has a wave number shift perpendicular to the pump axis such that $k_\perp/k_0 \ll 1$. The intensity-dependent phase shifts due to the pump fields cause a phase retardation of the sidebands F_\pm and B_\pm [75] with respect to the pumps.

The four complex amplitude equations which govern the linear evolution of the four sidebands are obtained by applying the expansion in Eqs. (4.5) and (4.6) to the coupled nonlinear Shroedinger equations Eqs. (2.15). The depletion of the pump due to interaction with the sidebands and terms which are quadratic or cubic in the sideband amplitudes are assumed to be small. By taking the Laplace transforms of the resulting linearized equations, the set of four sideband equations

become linear ordinary differential equations

$$\begin{aligned} v d_z F_+ &= i(\omega - \mu k_\perp^2 + \lambda |F_0|^2) F_+ \\ &\quad + i\lambda |F_0|^2 F_-^* + i\epsilon\lambda |F_0 B_0| (B_+ + B_-^*), \end{aligned} \quad (4.7)$$

$$\begin{aligned} v d_z F_-^* &= i(\omega + \mu k_\perp^2 - \lambda |F_0|^2) F_-^* \\ &\quad - i\lambda |F_0|^2 F_+ - i\epsilon\lambda |F_0 B_0| (B_+ + B_-^*), \end{aligned} \quad (4.8)$$

$$\begin{aligned} -v d_z B_+ &= i(\omega - \mu k_\perp^2 + \lambda |B_0|^2) B_+ \\ &\quad + i\lambda |B_0|^2 B_-^* + i\epsilon\lambda |F_0 B_0| (F_+ + F_-^*), \end{aligned} \quad (4.9)$$

$$\begin{aligned} -v d_z B_-^* &= i(\omega + \mu k_\perp^2 - \lambda |B_0|^2) B_-^* \\ &\quad - i\lambda |B_0|^2 B_+ - i\epsilon\lambda |F_0 B_0| (F_+ + F_-^*), \end{aligned} \quad (4.10)$$

where the pump envelopes are taken to be real, $\mu = \mu_\perp$ and $\sigma = \sigma_\perp$. The terms nonlinear in the sideband amplitudes which have been neglected consist of a set of second-order processes which couple two sidebands and one pump to drive a pump and a set of third-order processes which couple three sidebands to drive a sideband. These higher-order terms should be retained in the pump depletion regime or when the weaker of the two pump fields is of the same order as the probe. Neither of these cases will be discussed here.

The four-sideband interaction is mediated by the refractive index gratings of the perturbed system which have components $\langle \delta n \rangle(\omega, 2k_0 \pm k_\perp)$, $\langle \delta n \rangle(\omega, \pm k_\perp)$ along with their conjugates. The scattered fields may have frequencies shifted by $\pm\omega$ with respect to the pump-wave frequency. When high frequency material modes are of interest gratings at $2\omega_0$ become important.

By inspection of Eqs. (4.7)–(4.10) it is clear that the growth of instabilities in this four-sideband interaction depends only on the five parameters μk_\perp^2 , ω , $\epsilon\lambda |F_0 B_0|$, $\lambda |B_0|^2$ and $\lambda |F_0|^2$. The terms μk_\perp^2 and ω give rise to the linear phase

shifts in Eqs. (4.7)–(4.10). The transverse wave number parameter is related to the scattering angle of the sidebands as $\theta^2 = 2\mu k_{\perp}^2/vk_0$. The other three coupling terms are proportional to the pump strengths and give rise to nonlinear phase shifts. Note that neither the coupled nonlinear Schroedinger equations, Eqs. (2.15), nor the four sideband equations, Eqs. (4.7)–(4.10), depend on the initial phase shift between the pumps. As a result, the efficiency with which sidebands can couple to the pumps to exchange energy is a function only of the five parameters stated. In the remainder of this paper, these five quantities will be redefined such that $\omega = \omega L/v$, $r = |B_0/F_0|$, $\sigma P = \lambda|F_0|^2 L/v$, and $k_{\perp}^2 = \mu k_{\perp}^2 L/v = \theta^2 k_0 L/2$. The sign of λ is parameterized by σ . When μ is positive, as is the case for light waves in plasmas, σ is positive for self-focusing media and negative for self-defocusing media. The position variable will be scaled to the length of the medium: $\xi = z/L$.

4.1 Two-Sideband Limits of the Four Sideband Equations

In this section, each of the two-sideband limits of the four-sideband interaction is identified as a limit of the four sideband equations, Eqs. (4.7)–(4.10), by transforming the envelopes according to

$$F_+ = f_+ \exp(i(\omega - k_{\perp}^2)\xi) , \quad (4.11)$$

$$F_-^* = f_-^* \exp(i(\omega + k_{\perp}^2)\xi) , \quad (4.12)$$

$$B_+ = b_+ \exp(-i(\omega - k_{\perp}^2)\xi) , \quad (4.13)$$

$$B_-^* = b_-^* \exp(-i(\omega + k_{\perp}^2)\xi) . \quad (4.14)$$

This transformation creates a set of envelopes from which the linear wavenumber shifts have been removed. The governing equations for this set of transformed

wave envelopes contain terms on the right hand side due only to nonlinear effects and have the form

$$\begin{aligned} d_\xi f_+ &= i\sigma P[f_+ + f_-^* \exp(2ik_\perp^2 \xi)] \\ &\quad + i\sigma \epsilon r P[b_+ \exp(-2i(\omega - k_\perp^2)\xi) + b_-^* \exp(-2i\omega\xi)] , \end{aligned} \quad (4.15)$$

$$\begin{aligned} d_\xi f_-^* &= -i\sigma P[f_-^* + f_+ \exp(-2ik_\perp^2 \xi)] \\ &\quad - i\sigma \epsilon r P[b_+ \exp(-2i\omega\xi) + b_-^* \exp(-2i(\omega + k_\perp^2)\xi)] , \end{aligned} \quad (4.16)$$

$$\begin{aligned} -d_\xi b_+ &= i\sigma r^2 P[b_+ + b_-^* \exp(-2ik_\perp^2 \xi)] \\ &\quad + i\sigma \epsilon r P[f_+ \exp(2i(\omega - k_\perp^2)\xi) + f_-^* \exp(2i\omega\xi)] , \end{aligned} \quad (4.17)$$

$$\begin{aligned} -d_\xi b_-^* &= -i\sigma r^2 P[b_-^* + b_+ \exp(2ik_\perp^2 \xi)] \\ &\quad - i\sigma \epsilon r P[f_+ \exp(2i\omega\xi) + f_-^* \exp(2i(\omega + k_\perp^2)\xi)] . \end{aligned} \quad (4.18)$$

Equations (4.15)–(4.18) are no longer autonomous, having phases $\pm 2k_\perp^2 \xi$, $\pm 2\omega\xi$ and $\pm 2(\omega \pm k_\perp^2)\xi$ in their coupling terms. In the limits where these phase terms become large, the coupling terms become unimportant and the equations decouple. These are the two-sideband limits of the four-sideband system.

In the limit of large ω at fixed k_\perp^2 , Eqs. (4.15)–(4.18) decouple into two pairs of equations which govern the forward FWM interaction of f_+ with f_-^* and b_+ with b_-^* . As illustrated in Fig. 4.2(a), the F_+ sideband can couple to the pump F_0 to drive a grating at (ω, k_\perp) . The F_0 pump may then scatter from this grating to create the F_- sideband. This set of light waves must satisfy the matching conditions

$$\omega_0 + \omega_0 = \omega_s + \omega_a , \quad (4.19)$$

$$\vec{k}_0 + \vec{k}_0 = \vec{k}_s + \vec{k}_a , \quad (4.20)$$

where the subscripts denote Stokes and anti-Stokes sidebands. These two sideband equations are also obtained in the single-pump-wave limit where the cross-coupling

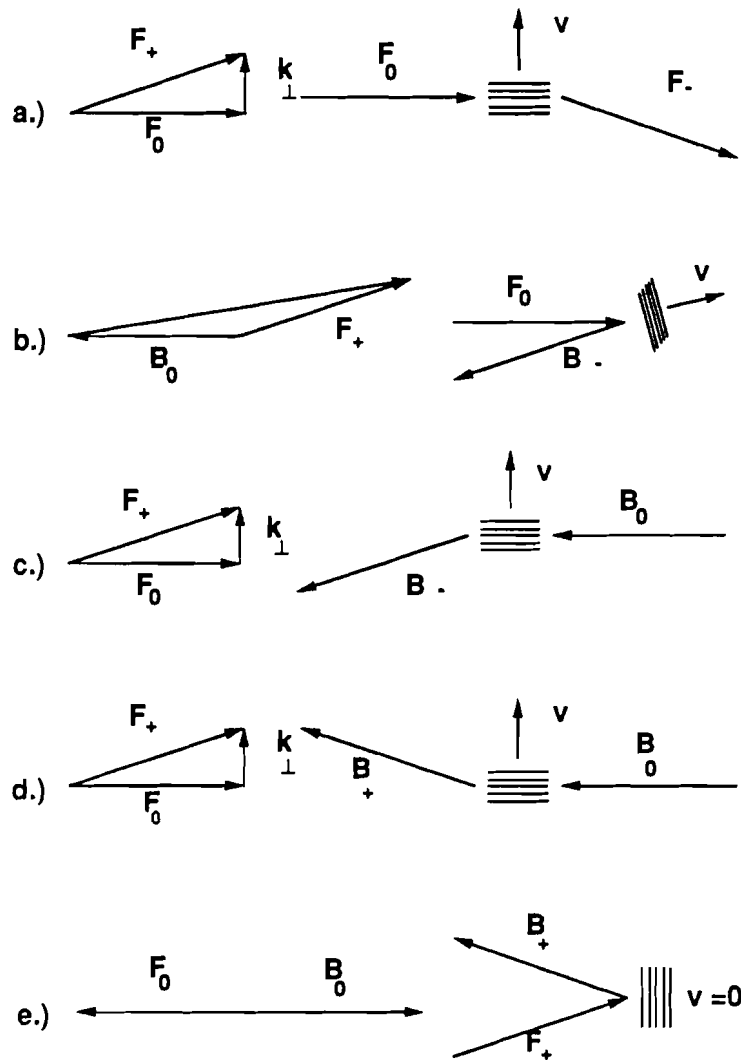


Figure 4.2: Each two-sideband interaction is shown: (a.) forward FWM, (b.) phase conjugation from the short wavelength grating, (c.) phase conjugation from the long wavelength grating, (d.) Bragg reflection from the long wavelength grating, (e.) Bragg reflection from the static $2k_0$ grating.

coefficient ϵ goes to zero at arbitrary ω and k_{\perp}^2 . Though the non-autonomous form of these equations facilitates the understanding of the limits in which the two-sideband interactions are recovered, solutions will be obtained using the envelopes of the original autonomous four sideband equations, Eqs. (4.7)–(4.10).

As the two pairs of sidebands propagate with their respective pumps, energy from the pumps may be transferred to the sidebands. If the F_+ sideband is seeded with an initial amplitude δ ,

$$F_+(\xi) = \delta \left[\cosh(k\xi) - i \frac{(k_{\perp}^2 - \sigma P)}{k} \sinh(k\xi) \right] \exp(i\omega\xi), \quad (4.21)$$

$$F_-(\xi) = -i\delta \frac{\sigma P}{k} \sinh(k\xi) \exp(i\omega\xi), \quad (4.22)$$

where $k = k_{\perp}(2\sigma P - k_{\perp}^2)^{\frac{1}{2}}$, and equivalent results can be obtained for the backward propagating pair of sidebands. Note that ω enters these solutions only as a phase factor. A band of unstable transverse wave numbers exists for $\sigma > 0$ when k_{\perp}^2 is in the interval $(0, 2P)$. The transverse wave number with the greatest gain occurs when $k_{\perp}^2 = P$, so $k_{opt} = P$. This well-known result [75] yields the value of the linear phase mismatch which balances the nonlinear phase shift. At this optimal wave number $F_+(1) \propto \cosh(P)$ and $F_-(1) \propto \sinh(P)$, so both sidebands grow exponentially at the optimal growth rate P . As the two pairs of sidebands propagate, they conserve the quantities

$$d_{\xi}(|F_+|^2 - |F_-|^2) = 0, \quad (4.23)$$

$$d_{\xi}(|B_+|^2 - |B_-|^2) = 0, \quad (4.24)$$

so that their gain is restricted only by the length of the medium. If $\sigma < 0$, the strongest interaction occurs for $0 < k_{\perp}^2 < [P^2 + (\frac{\pi}{2})^2]^{\frac{1}{2}} + P$, energy exchange is periodic as a function of P , and the interaction is stable. Note that for $k_{\perp}^2 L/2k_0 = 0$ the interaction of F_+ with F_-^* yields no net gain and $F_+ + F_-^* = \delta$, where

$$|F_+(1)/\delta| = \sqrt{1 + P^2} \text{ and } |F_-(1)/\delta| = P:$$

Taken together, this pair of sidebands is equivalent to a transverse spatial modulation of the light-wave intensity profile, so in a self-focusing medium the modulations grow as the interaction proceeds. This near-forward scattering instability is the TMI, and is associated with filamentation and self focusing in its fully nonlinear manifestation [76 – 83]. In plasmas, ponderomotive [4], thermal [82], and relativistic [11] effects are known to cause nonlinear focusing and filamentation. Extensive reference lists of work on the filamentation instability in laser-generated plasmas can be found in the review article by Sodha, Ghatak and Tripathi [82] and in the recent work by Kruer [4, 83]. In self-defocusing media, the index of refraction decreases as the intensity is increased, so transverse modulations in the intensity profile of a single light wave tend to be dispersed rather than enhanced.

The TMI has a dominant band of unstable transverse perturbation wave numbers. As a result, the transverse spatial Fourier spectrum of the scattered light will contain sidebands centered on the optimal transverse perturbation wave number or equivalently at the optimal cone angle. These sidebands are a signature of the instability. Since this interaction is invariant with respect to rotations about the collinear pump axis, a probe sideband injected at any point on the circle determined by the optimal cone angle will result in the appearance of a signal sideband located exactly opposite the probe signal on a similar circle at the output. When this convective instability is seeded by noise, all orientations of the sidebands are seeded equally and conical emission occurs.

In the large k_{\perp}^2 limit for finite ω , the four sideband equations separate into two sets of coupled equations that govern the backward FWM or phase conjugate interaction of f_+ with b_-^* and f_-^* with b_+ [9, 10]. In Figs. 4.2(b) and 4.2(c) the

wave vector diagrams for this interaction are shown. A probe beats with a copropagating or counterpropagating pump to form a grating at (ω, k_{\perp}) or $(\omega, 2k_0 \pm k_{\perp})$, respectively. The opposing pump can then scatter from either grating to produce a sideband that propagates in the opposite direction with respect to the probe and has the opposite frequency shift. This interaction must satisfy the matching conditions

$$\omega_0 + \omega_0 = \omega_s + \omega_a , \quad (4.25)$$

$$\vec{k}_0 - \vec{k}_0 = \vec{k}_s + \vec{k}_a , \quad (4.26)$$

and occurs in either self-focusing or self-defocusing media.

In this case, the two-sideband equations possess the conserved quantities

$$d_{\xi}(|B_{\pm}|^2 + |F_{\mp}|^2) = 0 . \quad (4.27)$$

The fraction of pump energy that can be diverted to the sidebands is not limited, since a probe entering the medium with intensity δ^2 at $\xi = 0$ having a companion sideband with zero intensity at $\xi = 1$ must satisfy the condition

$$\delta^2 = |F_{\pm}(1)|^2 - |B_{\mp}(0)|^2 . \quad (4.28)$$

For the linear model, growth of the convective instability is limited only by the length of the medium, and the growth of the absolute instability is limited only by the temporal extent of the pump.

Below the absolute threshold, the sidebands evolve such that [9, 10, 84]

$$F_+(\xi) = \delta \frac{[k \cos(k(1-\xi)) - i \sin(k(1-\xi))] \exp(i\gamma\xi)}{[k \cos(k) - i\phi \sin(k)]} , \quad (4.29)$$

$$B_-^*(\xi) = i\delta\epsilon r \sigma P \frac{\sin(k(1-\xi)) \exp(i\gamma\xi)}{[k \cos(k) - i\phi \sin(k)]} . \quad (4.30)$$

where $k^2 = \phi^2 + (\epsilon r P)^2$, $\phi = \omega + \sigma P(1 - r^2)/2$, $\gamma = \sigma P(r^2 + 1)/2 - k_{\perp}^2$ and δ is again the amplitude of the injected probe sideband. The gain spectrum of

this interaction is independent of k_{\perp}^2 and occurs predominantly over the band of frequencies

$$\omega = \sigma P \frac{(r^2 - 1)}{2} \pm [\pi^2 - (\epsilon r P)^2]^{\frac{1}{2}}. \quad (4.31)$$

At the peak of this band of frequencies, $\phi = 0$, so $k = \epsilon r P$. The gain at this value of k is faster than exponential, since $F_+(1) \propto \sec(\epsilon r P)$ and $B_-^*(0) \propto \tan(\epsilon r P)$. As the pump intensity is increased, the modes near this peak become absolutely unstable. Note that the convective gain is independent of r for this interaction when P is measured in terms of a constant fraction of the threshold intensity. Analogous solutions may be obtained for the other pair of sidebands.

The absolute instability intensity threshold for phase conjugation, P_{pco} , is $\pi(2n - 1)/2\epsilon r$, $n = 1, 2, 3, \dots$, and the associated oscillation frequency shift of the absolutely unstable sidebands at threshold is $\omega_{pco} = -\sigma P(1 - r^2)/2$. This frequency shift has the opposite sign for the other pair of sidebands, so either sign of the frequency shift may occur in the four-sideband system. Near the absolute instability threshold, the temporal growth rate is small and

$$\omega_i = \left[(\epsilon r P)^2 - \left(\frac{\pi(2n - 1)}{2} + \rho_n \right)^2 \right]^{\frac{1}{2}}, \quad (4.32)$$

where ω_i is the imaginary part of ω and the ρ_n are small corrections which can be obtained by solving the equation $k = -\omega_i \tan(k)$ when $k^2 = \omega_i^2 + (\epsilon r P)^2$. Well above threshold ω_i approaches the infinite medium limit $\epsilon r P$ with $\omega_{r \text{ inf}} = \omega_{pco}$ [85] since $\omega_i \approx [(\epsilon r P)^2 - (n\pi)^2]^{\frac{1}{2}}$, $n = 1, 2, 3, \dots$ for $\epsilon r P \gg n\pi$. Thus, the absolute instability threshold increases as $1/r$ and its temporal growth rate decreases as r decreases. These results for the characteristic frequencies and wavenumbers of the unstable eigenmodes are consistent with Eqs. (3A.18).

In the limit of large ω and k_{\perp}^2 with fixed $\omega - k_{\perp}^2$, Eqs. (4.15)–(4.18) reduce to a pair of coupled equations which govern the Bragg reflection interaction [84] of f_+

with b_+ . An equivalent limit is obtained for f_- and b_- at large $-\omega$ and k_\perp^2 when $\omega + k_\perp^2$ is held fixed. Each interaction is mediated by either the (ω, k_\perp) or the $(0, 2k_0)$ grating. Their wave vector diagrams are shown in Figs. 4.2(d) and 4.2(e). A pair of interacting anti-Stokes sidebands must satisfy the matching conditions

$$\omega_0 - \omega_{f_a} = \omega_0 - \omega_{b_a} , \quad (4.33)$$

$$-\vec{k}_0 + \vec{k}_{f_a} = \vec{k}_0 + \vec{k}_{b_a} , \quad (4.34)$$

where similar conditions hold for the Stokes sideband pairs. Again, note that both pairs of equations are independent of the quantity over which the limit is taken.

These equations possess the conserved quantities

$$d_\xi(|F_\pm|^2 - |B_\pm|^2) = 0 , \quad (4.35)$$

which imply that a probe entering the medium with intensity δ^2 at $\xi = 0$ and having a companion sideband with zero intensity at $\xi = 1$ must satisfy the condition

$$\delta^2 = |B_\pm(0)|^2 + |F_\pm(1)|^2 . \quad (4.36)$$

Thus, the sidebands exchange energy with each other but not with the pumps, and the gain is limited by the size of the probe. As a two-sideband process, this interaction is stable.

If the input probe field has amplitude δ , the evolution of the sidebands is given by:

$$F_+(\xi) = \delta \epsilon r \sigma P \frac{[k \cos(k(1-\xi)) - i\nu \sin(k(1-\xi))] \exp(i\Omega\xi)}{[k \cos(k) - i\nu \sin(k)]} , \quad (4.37)$$

$$B_+(\xi) = i\delta \epsilon r \sigma P \frac{\sin(k(1-\xi)) \exp(i\Omega\xi)}{[k \cos(k) - i\nu \sin(k)]} , \quad (4.38)$$

where $k = \sqrt{\nu^2 - (\epsilon r P)^2}$, $\nu = \omega - k_\perp^2 + \sigma P(1 + r^2)/2$ and $\Omega = \sigma P(1 - r^2)/2$. In this case, the two sidebands exchange energy primarily in a band of (ω, k_\perp^2) space

where

$$\omega - k_{\perp}^2 = -\sigma P \frac{(1+r^2)}{2} \pm [\pi^2 + (\epsilon r P)^2]^{\frac{1}{2}}. \quad (4.39)$$

For a given ω , the peak of this band corresponds to the transverse wave number for which the interaction is strongest and is given by $\nu = 0$, or $k_{\perp}^2 = \omega + \sigma P(1+r^2)/2$, making $k_{opt} = i\epsilon r P$. At this peak the linear phase shift balances the nonlinear phase shift, and the optimal mode evolves such that $F_+(1) \propto \text{sech}(\epsilon r P)$ and $B_+(0) \propto \tanh(\epsilon r P)$. Thus, the two sidebands exchange their energy only once as a function of $\epsilon r P$ and remain stable. In the $k_{\perp}^2 + \omega$ limit, the band of (ω, k_{\perp}^2) space where the two sidebands interact most strongly is located between

$$\omega + k_{\perp}^2 = \sigma P \frac{(1+r^2)}{2} \pm [\pi^2 + (\epsilon r P)^2]^{\frac{1}{2}}. \quad (4.40)$$

These modes are also stable and have solutions similar to those of the $\omega - k_{\perp}^2$ limit.

In each of the limits discussed above, a single two-sideband interaction is phase matched. The regions within which these two-sideband processes occur most strongly are plotted in (ω, k_{\perp}^2) space in Fig. 4.3. For small ω and k_{\perp}^2 these regions overlap. In this overlap region, each of the two-sideband processes can be phase matched simultaneously, allowing a four-sideband interaction to occur. In addition, the four sideband equations possess the conserved quantity

$$d_{\xi}(|F_+|^2 - |F_-|^2 - |B_+|^2 + |B_-|^2) = 0, \quad (4.41)$$

so no restrictions are imposed on the linear growth of the sidebands. These two points suggest that it is necessary to consider the complete four-sideband interaction. In the next section, the four-sideband interaction is analyzed.

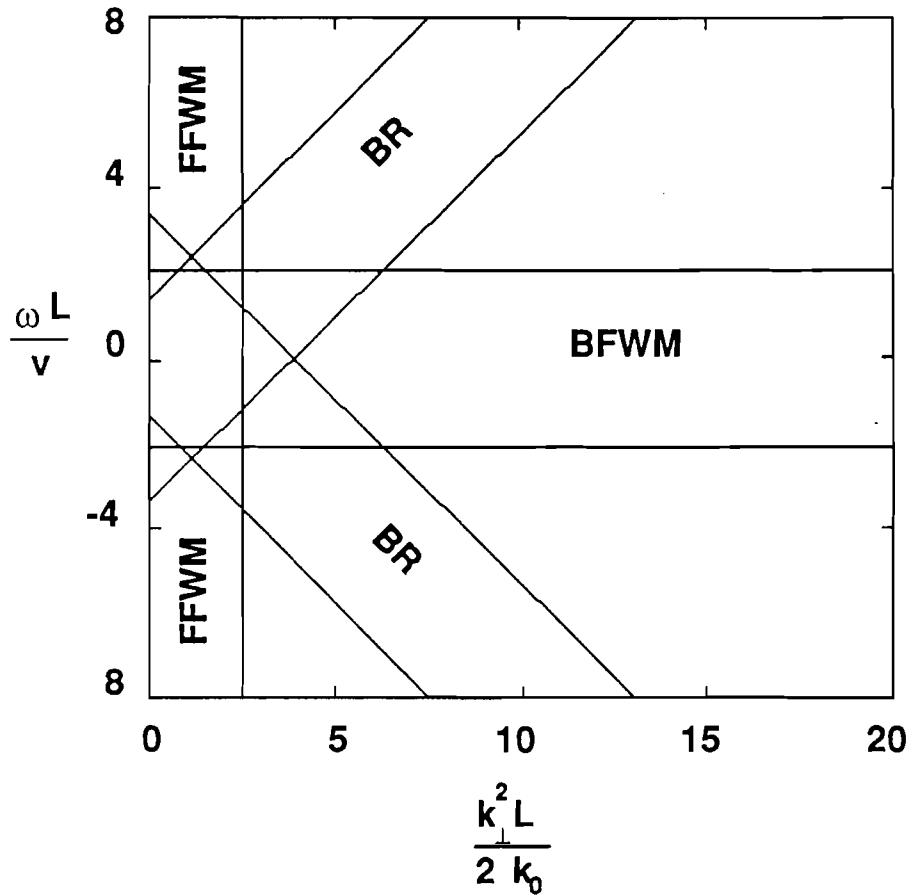


Figure 4.3: The primary bands of the gain spectra for the two-sideband interactions are plotted in the plane of the real part of the perturbation frequency, $\text{Re}(\omega L/v)$, and the transverse perturbation wavenumber parameter, $k_{\perp}^2 L/2k_0$. The cooperative instability occurs in the region of overlap for small k_{\perp}^2 and small ω .

4.2 The Four-Sideband Interaction

In this section, the properties of the linearized four sideband equations are discussed and solutions are obtained for the convective gain spectrum and the absolute instability threshold. In matrix form the linear four sideband equations, Eqs. (4.7)–(4.10), become

$$d_\xi \vec{A} = iM \vec{A}, \quad (4.42)$$

where $\vec{A} = (F_+, F_-, B_+, B_-)^T$ is the column vector of complex envelopes, and M is the following coefficient matrix:

$$M = \begin{pmatrix} (\omega - k_\perp^2 + \sigma P) \sigma P & \sigma \epsilon r P & \sigma \epsilon r P & \\ -\sigma P & (\omega + k_\perp^2 - \sigma P) & -\sigma \epsilon r P & -\sigma \epsilon r P \\ -\sigma \epsilon r P & -\sigma \epsilon r P & -(\omega - k_\perp^2 + \sigma r^2 P) & -\sigma r^2 P \\ \sigma \epsilon r P & \sigma \epsilon r P & \sigma r^2 P & -(\omega + k_\perp^2 - \sigma r^2 P) \end{pmatrix}. \quad (4.43)$$

While each of the off-diagonal matrix elements of M is real, the diagonal self-interaction terms contain the complex variable ω , so that the propagation matrix is nonhermitian. The antisymmetric part contains the couplings for the forward FWM pairs and for the Bragg reflected pairs. The forward FWM coupling terms are antisymmetric because the F_- and B_- equations are conjugated. The conjugation operation also reverses the sense of the wave vectors. The Bragg-reflection cross-coupling terms are antisymmetric because the sign of the group velocities is included within M . This operation also effectively reverses the sense of propagation in the B-equations, Eqs. (4.9) and (4.10). The phase-conjugation couplings are symmetric because they are subject to both the effect of conjugation and counterpropagation. The combination of these operations produces the coupling matrix M , which governs the equivalent system of four copropagating sidebands.

Since the medium is homogeneous, Eqs. (4.7)–(4.10) are invariant to the exchange of B with F , k_\perp with $-k_\perp$, and ξ with $-\xi$. In addition, the transformation

ω to $-\omega^*$ causes a plus sideband to become a minus sideband. These symmetry properties are reflected in the coupled nonlinear Shroedinger equations and in the solutions presented below. When the pumps have unequal intensity, it is of interest to compare the gain spectrum due to a seed sideband which is injected from the strong-pump side of the medium with that due to a seed sideband which is injected from the weak-pump side of the medium. This is accomplished by making the transformation $P' = rP$, $r' = 1/r$.

The unique solution of Eq. (4.42) is written formally as

$$\vec{A}(\xi) = \exp(iM\xi)\vec{A}(0) , \quad (4.44)$$

where the matrix M can be exponentiated using the relation

$$\exp(iM\xi) = U \exp(iQ\xi)U^{-1} , \quad (4.45)$$

with U the matrix of eigenvectors of M , and Q the diagonal matrix of its eigenvalues. The four sideband equations are solved as a two-point boundary value problem, so Eq. (4.44) is rewritten as

$$\vec{A}_{out} = S\vec{A}_{in} , \quad (4.46)$$

where S maps input sidebands to their scattered sideband counterparts. The new sideband envelope vectors can be written in the form

$$\vec{A}_{in} = T_0\vec{A}(0) + T_1\vec{A}(1) , \quad (4.47)$$

$$\vec{A}_{out} = T_1\vec{A}(0) + T_0\vec{A}(1) , \quad (4.48)$$

and S is given formally by

$$S = [T_0 - \exp(iM)T_1]^{-1}[\exp(iM)T_0 - T_1] , \quad (4.49)$$

where,

$$T_0 = \begin{pmatrix} I_2 & 0 \\ 0 & 0 \end{pmatrix}, \quad T_1 = \begin{pmatrix} 0 & 0 \\ 0 & I_2 \end{pmatrix}. \quad (4.50)$$

Here, I_2 is the two dimensional identity matrix. In the discussion that follows the input amplitude vector will be $\vec{A}_{in} = (\delta, 0, 0, 0)^T$. This single probe-sideband with amplitude δ is injected into the nonlinear medium at $z = 0$ and scatters into four sidebands. The gain spectrum is given by \vec{A}_{out} or equivalently by S_{i1} . In practice, it may be easier to calculate S by assuming that the eigenfunctions have their usual exponential form

$$A_i = \sum_{j=1}^4 c_j U_{ij} \exp(ik_j \xi), \quad i = 1 - 4, \quad (4.51)$$

where \vec{c} is a constant vector, U is the matrix of eigenvectors of M , and the k_i are its eigenvalues. By applying the boundary conditions, A_{in} , Eqs. (4.51) can be reduced to the form of Eq. (4.46).

As the pump power is increased, the convective gain of the scattered sidebands increases. The system becomes absolutely unstable when sideband growth occurs as a function of time in the frame of the nonlinear medium. When the initial condition terms associated with the Laplace transform are retained, the Laplace inversion of $S(\omega)$ is the solution to the initial value problem. The poles of $S(\omega)$ are determined by the condition

$$\Delta = |T_0 - \exp(iM)T_1| = 0, \quad (4.52)$$

which is simply the determinant of the lower right hand partition of $\exp(iM)$. If the temporal growth rate of one of these poles is positive, $\omega_i > 0$, the system exhibits an absolute instability. This condition is equivalent to the condition that there be a nontrivial solution A_{out} with $\text{Im}(\omega) > 0$ when $F_{\pm}(0) = 0$, and $B_{\pm}(1) = 0$. As a result, the poles of $S(\omega)$ reveal the temporal stability of the

system directly, and contribute to the solution of the initial value problem as exponential factors which increase with time.

In the relatively rare case in which a pair of eigenvalues of M merge, the set of linear independent eigenvectors defined in Eq. (4.51) may no longer span the entire solution space. A new set of linear independent eigenvectors can be constructed which does span the entire solution space by generalizing U and Q to their canonical forms. With this generalization the above discussion continues to hold, but terms are introduced into the general solution which grow secularly with position, since at least one of the sidebands is driven at its fundamental wave number by one of the coupling terms.

When simple analytic expressions for the eigenvalues k_j exist, it is feasible to find analytic expressions for the envelopes A_i . The eigenvalue equation for M is biquadratic for the cases $\omega = 0$ or $r = 1$. In these two cases, the linear convective gain and absolute instability thresholds can be written in a reasonably compact form. In the following subsection the A_i are calculated analytically for these two cases, and numerical techniques are used to obtain solutions for more general cases. In the final subsection, the absolute instability thresholds are reviewed, and the thresholds for more general cases are calculated numerically.

4.2.1 Solutions in the Convective Regime

In the convective regime, where the pump intensity is below the threshold for absolute instability, the growth of the sidebands is obtained by calculating the matrix elements S_{i1} . The eigenvalues, k_j , of M are the roots of

$$\begin{aligned} & [(k_j + \omega)^2 + k_{\perp}^2(2\sigma r^2 P - k_{\perp}^2)] \\ & \times [(k_j - \omega)^2 + k_{\perp}^2(2\sigma P - k_{\perp}^2)] - (2\epsilon r P k_{\perp}^2)^2 = 0, \quad j = 1 - 4. \end{aligned} \quad (4.53)$$

Given four distinct eigenvalues, the matrix elements S_{i1} can be found by applying the boundary conditions, A_{in} , to Eq. (4.51). The analytic solutions for the convective gain of the four sidebands have the form

$$\begin{aligned}
F_+(\xi) &= \sum_{j=1}^4 a_j \left[1 - \left(\frac{k_j - \omega}{k_1^2} \right) \right] \exp(ik_j \xi) , \\
F_-^*(\xi) &= \sum_{j=1}^4 a_j \left[1 + \left(\frac{k_j - \omega}{k_1^2} \right) \right] \exp(ik_j \xi) , \\
B_+(\xi) &= - \sum_{j=1}^4 a_j \frac{\alpha_j}{2\epsilon r P k_1^2} \left[1 + \left(\frac{k_j + \omega}{k_1^2} \right) \right] \exp(ik_j(\xi - 1)) , \\
B_-^*(\xi) &= - \sum_{j=1}^4 a_j \frac{\alpha_j}{2\epsilon r P k_1^2} \left[1 - \left(\frac{k_j + \omega}{k_1^2} \right) \right] \exp(ik_j(\xi - 1)) , \quad (4.54)
\end{aligned}$$

where $\alpha_j = [(k_j - \omega)^2 + \kappa] \exp(ik_j)$ and $\kappa = k_1^2(2\sigma P - k_1^2)$. The constants are

$$\begin{aligned}
a_1 &= \frac{\delta k_1^2}{2\Delta} \left\{ \alpha_4 \alpha_3 (k_4 - k_3) \left[1 + \left(\frac{k_2 - \omega}{k_1^2} \right) \right] \right. \\
&\quad \left. - \alpha_4 \alpha_2 (k_4 - k_2) \left[1 + \left(\frac{k_3 - \omega}{k_1^2} \right) \right] \right. \\
&\quad \left. + \alpha_3 \alpha_2 (k_3 - k_2) \left[1 + \left(\frac{k_4 - \omega}{k_1^2} \right) \right] \right\} , \quad (4.55)
\end{aligned}$$

$$a_2 = -a_1(2 \rightarrow 1) , \quad (4.56)$$

$$a_3 = -a_2(3 \rightarrow 2) , \quad (4.57)$$

$$a_4 = -a_3(4 \rightarrow 3) , \quad (4.58)$$

where

$$\begin{aligned}
\Delta &= (\alpha_4 \alpha_3 + \alpha_2 \alpha_1)(k_4 - k_3)(k_2 - k_1) \\
&\quad + (\alpha_4 \alpha_1 + \alpha_3 \alpha_2)(k_4 - k_1)(k_3 - k_2) \\
&\quad - (\alpha_4 \alpha_2 + \alpha_3 \alpha_1)(k_4 - k_2)(k_3 - k_1) . \quad (4.59)
\end{aligned}$$

These formulae are the most general form of the solution of the linear four-sideband system when the eigenvalues are distinct.

In the $\omega = 0$ case the eigenvalues given by Eq. (4.53) become

$$k_{\pm}^2 = k_{\perp}^2 \left\{ k_{\perp}^2 - \sigma P(1 + r^2) \pm P[(1 - r^2)^2 + (2\epsilon r)^2]^{\frac{1}{2}} \right\}, \quad (4.60)$$

and the general solutions for the sideband envelopes can be reduced to

$$\begin{aligned} F_{\pm}^{(*)}(1) &= \frac{2\delta}{\Delta_{\omega=0}} k_+ k_- (k_-^2 - k_+^2) \\ &\times \left\{ \Lambda_- \left[(1 \pm 1) \cos(k_+) - i \left(\frac{k_{\perp}^2}{k_+} \pm \frac{k_+}{k_{\perp}^2} \right) \sin(k_+) \right] \right. \\ &\left. - \Lambda_+ \left[(1 \pm 1) \cos(k_-) - i \left(\frac{k_{\perp}^2}{k_-} \pm \frac{k_-}{k_{\perp}^2} \right) \sin(k_-) \right] \right\}, \end{aligned} \quad (4.61)$$

$$\begin{aligned} B_{\pm}^{(*)}(0) &= -\frac{\delta \Lambda_- \Lambda_+ k_- k_+}{\epsilon r \sigma P k_{\perp}^2 \Delta_{\omega=0}} \left\{ (\Lambda_+ + \Lambda_-)(1 \mp 1) \right. \\ &- i(\Lambda_+ - \Lambda_-) \left[\left(\frac{k_{\perp}^2}{k_+} \mp \frac{k_+}{k_{\perp}^2} \right) \sin(k_+) \cos(k_-) \right. \\ &\quad \left. - \left(\frac{k_{\perp}^2}{k_-} \mp \frac{k_-}{k_{\perp}^2} \right) \sin(k_-) \cos(k_+) \right] \\ &- (\Lambda_+ \mp \Lambda_-) \left[\left(\frac{k_-}{k_+} \mp \frac{k_+}{k_-} \right) \sin(k_+) \sin(k_-) \right. \\ &\quad \left. + (1 \mp 1) \cos(k_+) \cos(k_-) \right] \left. \right\}, \end{aligned} \quad (4.62)$$

where (*) is associated with the minus amplitude and

$$\begin{aligned} \Delta_{\omega=0} &= 4(\Lambda_+^2 + \Lambda_-^2) k_+ k_- \\ &\quad - 8\Lambda_+ \Lambda_- k_+ k_- \cos(k_+) \cos(k_-) \\ &\quad - 4\Lambda_+ \Lambda_- (k_+^2 + k_-^2) \sin(k_+) \sin(k_-), \end{aligned} \quad (4.63)$$

$$\Lambda_{\pm} = k_{\pm}^2 + \kappa. \quad (4.64)$$

These solutions extend previous calculations of the convective gain spectrum obtained by Vlcek and Malanov [44] to $r \leq 1$ when $\omega = 0$ and correct what is probably a typographical error in their solutions, which should be invariant to the transformation $k_+ \rightarrow k_-$.

In the $r = 1$, case the eigenvalues reduce to

$$k_{\pm}^2 = \omega^2 - \kappa \pm 2[(\epsilon P k_{\perp}^2)^2 - \omega^2 \kappa]^{\frac{1}{2}}, \quad (4.65)$$

or, $k_{\pm}^2 = \omega^2 - \kappa \pm \beta$ where $\beta = 2[(\epsilon P k_{\perp}^2)^2 - \omega^2 \kappa]^{\frac{1}{2}}$. The general solutions, Eqs. (4.54), then become

$$\begin{aligned} F_{\pm}^{(*)}(1) &= \frac{4\beta\delta}{k_{\perp}^2 \Delta_{r=1}} \\ &\times \left\{ 2k_{\perp}^2 k_{-} k_{+} \left[\left(\frac{1 \pm 1}{2} \right) (\beta - 2\omega k_{\perp}^2) \pm 2\omega k_{\perp}^2 \sigma P \right] [\cos(k_{+}) + \cos(k_{-})] \right. \\ &+ i \left[\omega k_{\perp}^2 (1 \pm 1) (\beta - 2\kappa) - (\beta - 2\omega^2) (k_{\perp}^4 \mp \kappa) \pm (2\epsilon P k_{\perp}^2)^2 \right] \\ &\left. \times [k_{+} \sin(k_{-}) + k_{-} \sin(k_{+})] \right\} \end{aligned} \quad (4.66)$$

$$\begin{aligned} B_{\pm}^{(*)}(0) &= \frac{-8\delta\epsilon P}{\Delta_{r=1}} \left\{ 2\omega k_{+} k_{-} (k_{\perp}^4 \pm \kappa) [1 - \cos(k_{+}) \cos(k_{-})] \right. \\ &- \{ 2\omega(\kappa - \omega^2) (k_{\perp}^4 \mp \kappa) \pm \beta^2 [(1 \mp 1) k_{\perp}^2 + 2\omega^2] \} \sin(k_{-}) \sin(k_{+}) \\ &+ i\beta k_{-} [(k_{\perp}^2 \pm \omega) (k_{\perp}^2 + \omega) \mp k_{+}^2] \cos(k_{-}) \sin(k_{+}) \\ &\left. - i\beta k_{+} [(k_{\perp}^2 \pm \omega) (k_{\perp}^2 + \omega) \mp k_{-}^2] \cos(k_{+}) \sin(k_{-}) \right\}, \end{aligned} \quad (4.67)$$

where $(*)$ is associated with the minus amplitude, and

$$\begin{aligned} \frac{\Delta_{r=1}}{32} &= 2k_{+} k_{-} (\epsilon P k_{\perp}^2)^2 \\ &+ 2k_{+} k_{-} [(\epsilon P k_{\perp}^2)^2 - 2\omega^2 \kappa] \cos(k_{+}) \cos(k_{-}) \\ &+ 2[\omega^2 \kappa (3\omega^2 + 2\kappa) - (4\omega^2 + \kappa) (\epsilon P k_{\perp}^2)^2] \sin(k_{+}) \sin(k_{-}) \\ &- \omega\beta k_{+} (\beta + 2\kappa) \sin(k_{-}) \cos(k_{+}) \\ &- \omega\beta k_{-} (\beta - 2\kappa) \sin(k_{+}) \cos(k_{-}). \end{aligned} \quad (4.68)$$

Vlasov and Sheinina [45] have also obtained analytic expressions for the $r = 1$ case. The two sets of analytic solutions stated above have a common limit at $\omega = 0$ and $r = 1$. In addition, for the large k_{\perp}^2 , ω limits in which only two-sideband

interactions are phase matched, these solutions reproduce the two-sideband results stated in Sec. 4.1. These limits have been verified numerically.

In general, Eqs. (4.7)–(4.10) may be solved numerically to obtain S . This calculation has been carried out using a Newton-Raphson shooting routine [86] which is generalized to include complex amplitude equations. The analytic solutions shown above have been compared to the numerical solutions of Eqs. (4.7)–(4.10) and to the numerical solutions of the nonlinear sideband equations which include pump depletion. This exercise shows that the nonlinear terms are only important near the absolute instability threshold in the convective regime and above, and it provides an independent check for the analytic results.

In Figs. 4.4–4.9 the values of the four-sideband S_{i1} are displayed as a function of the transverse wave number k_{\perp}^2 and the real frequency shift ω_r . These calculations were carried out numerically with pump powers at $0.95P_{th}$, where P_{th} is the minimal threshold intensity for absolute instability. The gain spectrum, S_{i1} , for each sideband is displayed for symmetric pump fields, $r^2 = 1$, in Fig. 4.4–4.5. The gain spectrum in the case of asymmetric pump fields, $r^2 = 0.1$, is displayed in Figs. 4.6–4.9. Figures 4.6–4.7 display the convective gain spectrum when F_0 is the strong pump, and figures 4.8–4.9 display the convective gain spectrum when B_0 is the strong pump. Each case is considered for both self-focusing and self-defocusing media.

When the pump intensities are equal, the maximal gain occurs over a distinct region in (ω_r, k_{\perp}^2) space. This region is centered at $\omega_r = 0$ and is slightly shifted from the pump axis, $k_{\perp}^2 = 0$. It corresponds to the overlap region in Fig. 4.3. For each sideband in Figs. 4.4–4.5, this peak is the dominant feature. It occurs in the same location for each sideband. This peak is due to gain of the four-sideband TMI.

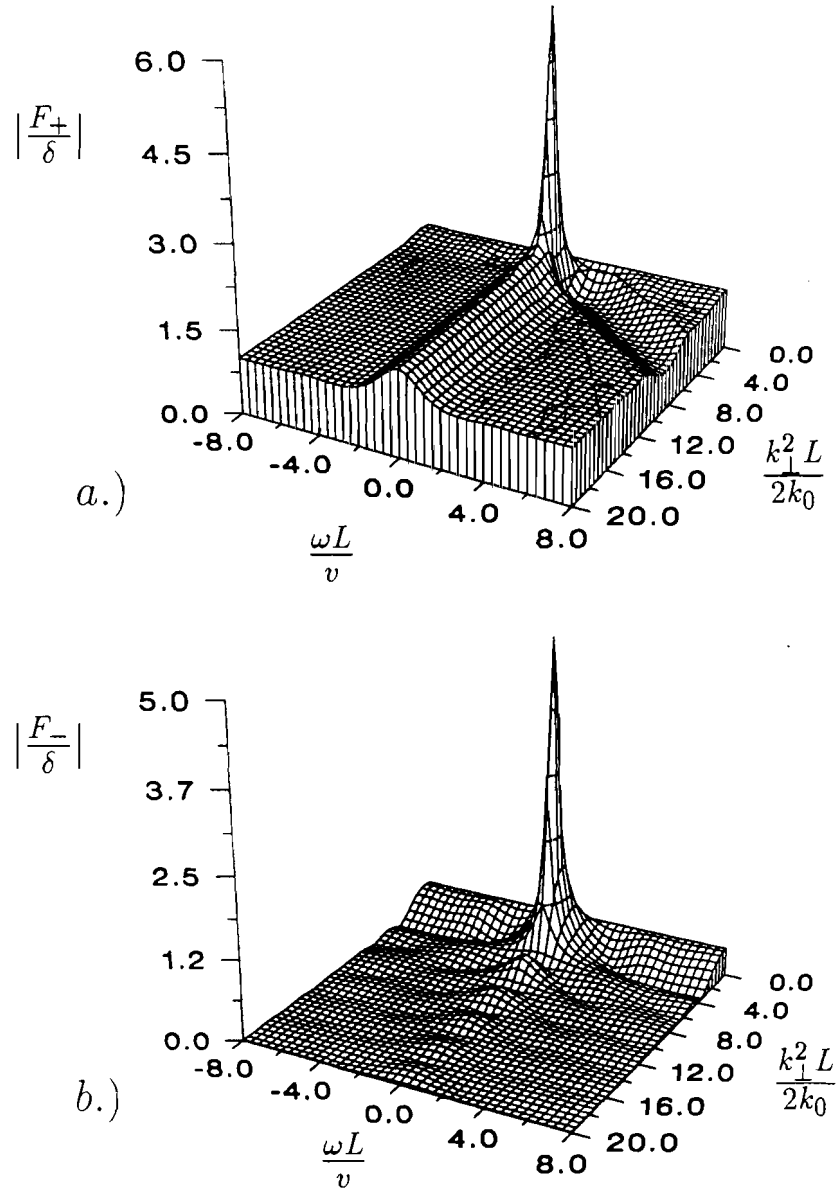


Figure 4.4: The linear convective gain spectrum for the four-sideband interaction is plotted in the plane of the real part of the perturbation frequency, $\text{Re}(\omega L/v)$, and the transverse perturbation wavenumber parameter, $k_{\perp}^2 L/2k_0$, for the case in which $\sigma = 1$, $\epsilon = 2.0$, $r^2 = 1.0$ and $P = 0.95P_{th} = 0.428$. The forward anti-Stokes sideband was seeded by $F_+(0) = \delta = 0.001$. Shown are the (a.) F_+ , and (b.) F_-^* sidebands.

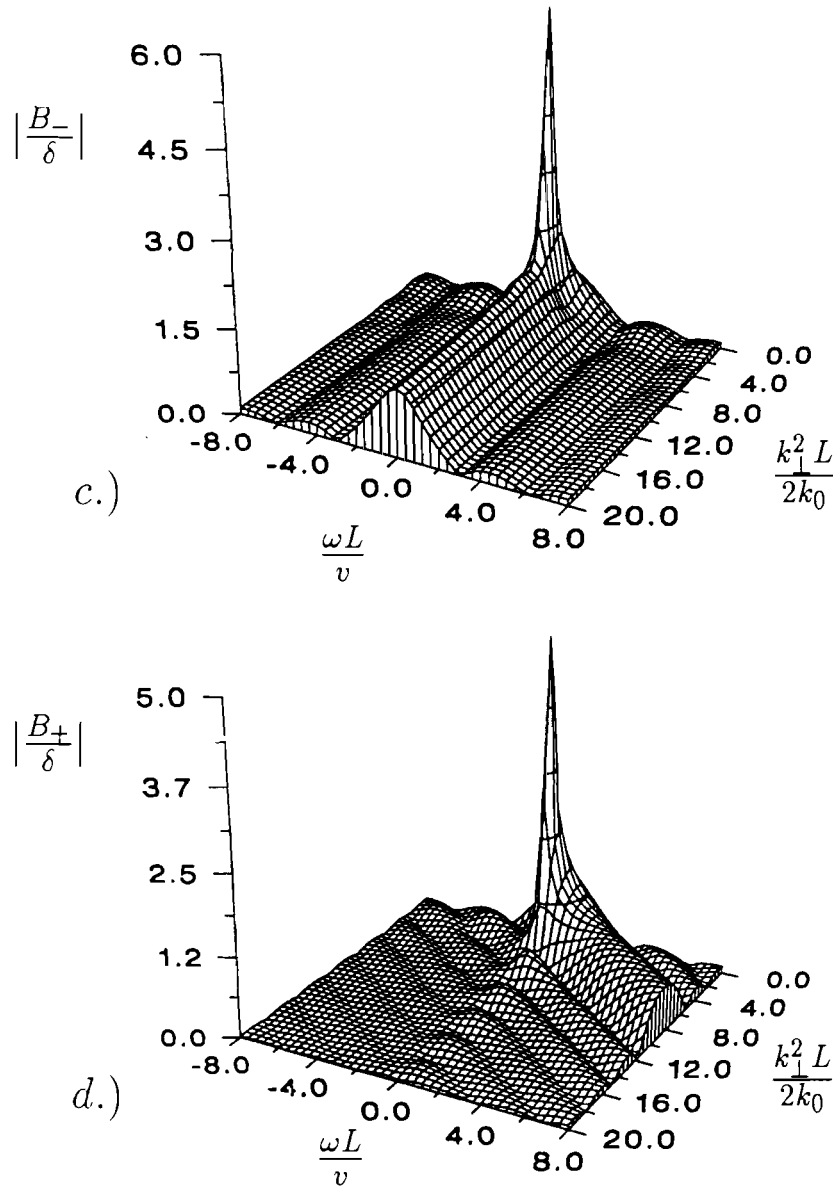


Figure 4.4: (continued) The linear convective gain spectrum for the four-sideband interaction is plotted in the plane of the real part of the perturbation frequency, $\text{Re}(\omega L/v)$, and the transverse perturbation wavenumber parameter, $k_{\perp}^2 L/2k_0$, for the case in which $\sigma = 1$, $\epsilon = 2.0$, $r^2 = 1.0$ and $P = 0.95P_{th} = 0.428$. The forward anti-Stokes sideband was seeded by $F_+(0) = \delta = 0.001$. Shown are the the (c.) B_-^* , and (d.) B_+ sidebands.

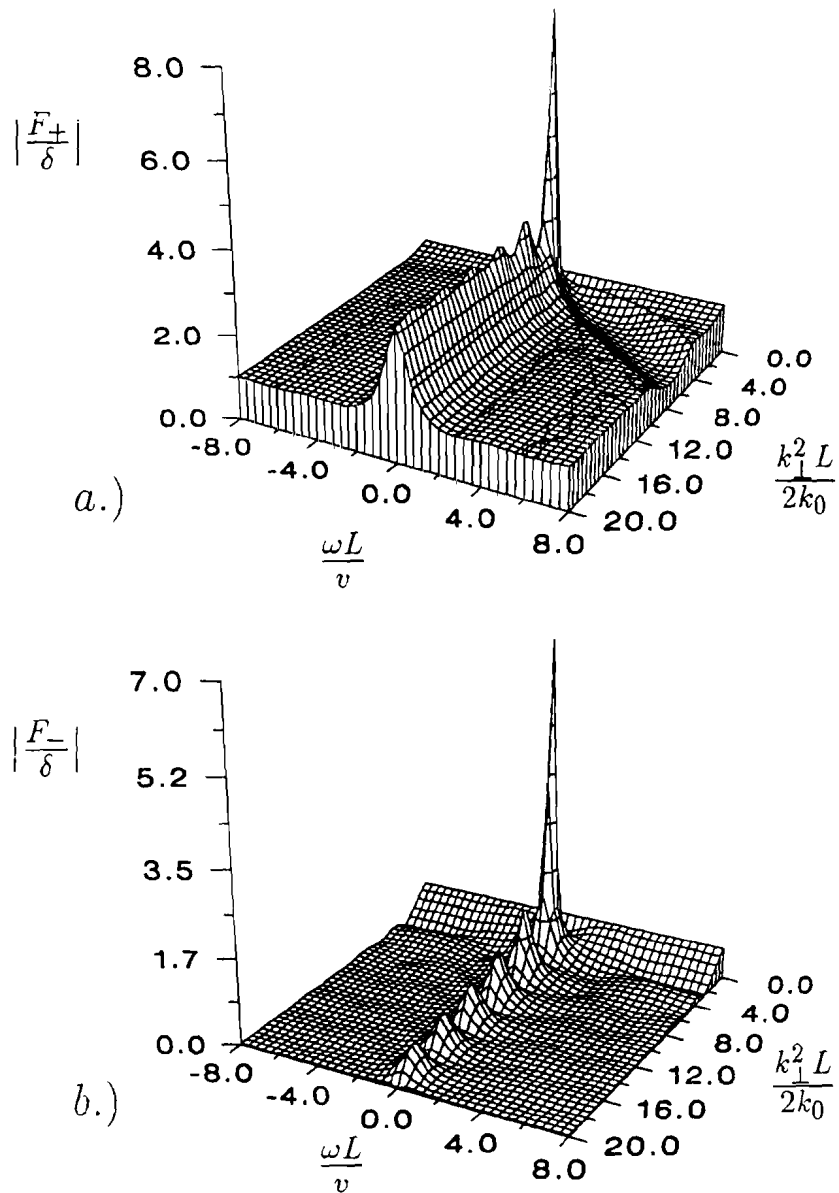


Figure 4.5: The linear convective gain spectrum for the four-sideband interaction is plotted in the plane of the real part of the perturbation frequency, $\text{Re}(\omega L/v)$, and the transverse perturbation wavenumber parameter, $k_1^2 L/2k_0$, for the case in which $\sigma = -1$, $\epsilon = 2.0$, $r^2 = 1.0$ and $P = 0.95P_{th} = 0.643$. The forward anti-Stokes sideband was seeded by $F_+(0) = \delta = 0.001$. Shown are the (a.) F_+ , and (b.) F_-^* sidebands.

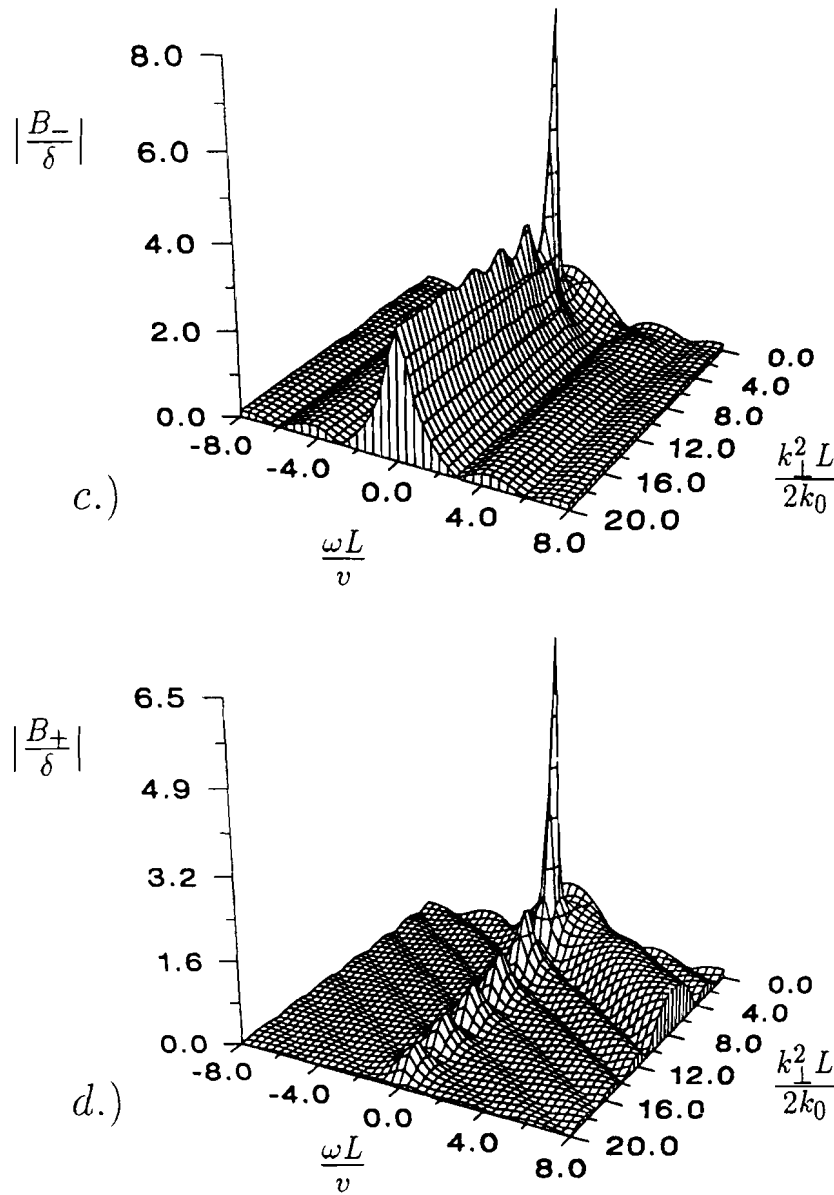


Figure 4.5: (continued) The linear convective gain spectrum for the four-sideband interaction is plotted in the plane of the real part of the perturbation frequency, $\text{Re}(\omega L/v)$, and the transverse perturbation wavenumber parameter, $k_{\perp}^2 L/2k_0$, for the case in which $\sigma = -1$, $\epsilon = 2.0$, $r^2 = 1.0$ and $P = 0.95P_{th} = 0.643$. The forward anti-Stokes sideband was seeded by $F_+(0) = \delta = 0.001$. Shown are the (c.) B_-^* , and (d.) B_+^* sidebands.

In the remainder of the ω_r, k_{\perp}^2 surface, three other types of gain can be observed. In Figs. 4.4(b) and 4.5(b) gain is seen to occur for $k_{\perp}^2 \approx 0$. This feature is independent of the frequency shift and has the same form as the gain of the two-sideband forward FWM interaction. In fact, this feature is exactly the forward FWM interaction having width $2P$ in self-focusing media and width $[P^2 + (\frac{\pi}{2})^2]^{\frac{1}{2}} + P$ in self-defocusing media. It was shown that the gain for this two-sideband interaction is exponential for self-focusing media, but oscillates for self-defocusing media.

In Figs. 4.4(c) and 4.5(c) gain occurs along $\omega = 0$. This feature is due to the phase-conjugate coupling between F_+ and B_-^* and at large k_{\perp}^2 it has the same gain spectrum as the corresponding two-sideband interaction. Its width is given by Eq. (4.31). Note that the gain due to the phase conjugate coupling is nearly half the gain due to four-sideband coupling for self-defocusing media, while the phase-conjugate gain is less than one third of the four-sideband gain in the self-focusing medium. Relative to the four-sideband instability, the phase-conjugate coupling has a more important role in self-defocusing media than it does in self-focusing media. The last feature can be seen in Figs. 4.4(d) and 4.5(d) where gain appears along the $\omega + k_{\perp}^2$ line. This feature is due to Bragg scattering by backward FWM. It is a stable interaction and it has the same gain spectrum as the two-sideband interaction. The width is predicted by Eqs. (4.39) and (4.40).

From Figs. 4.4–4.5 it is clear that the four-sideband interaction is optimally phase matched about a point that is not frequency shifted but has a small transverse wave number shift. Away from this point, the four sideband interaction is detuned, and further gain is due to two-sideband interactions which have the properties discussed in Sec. 4.1. This four-sideband instability dominates the gain of the two-sideband instabilities.

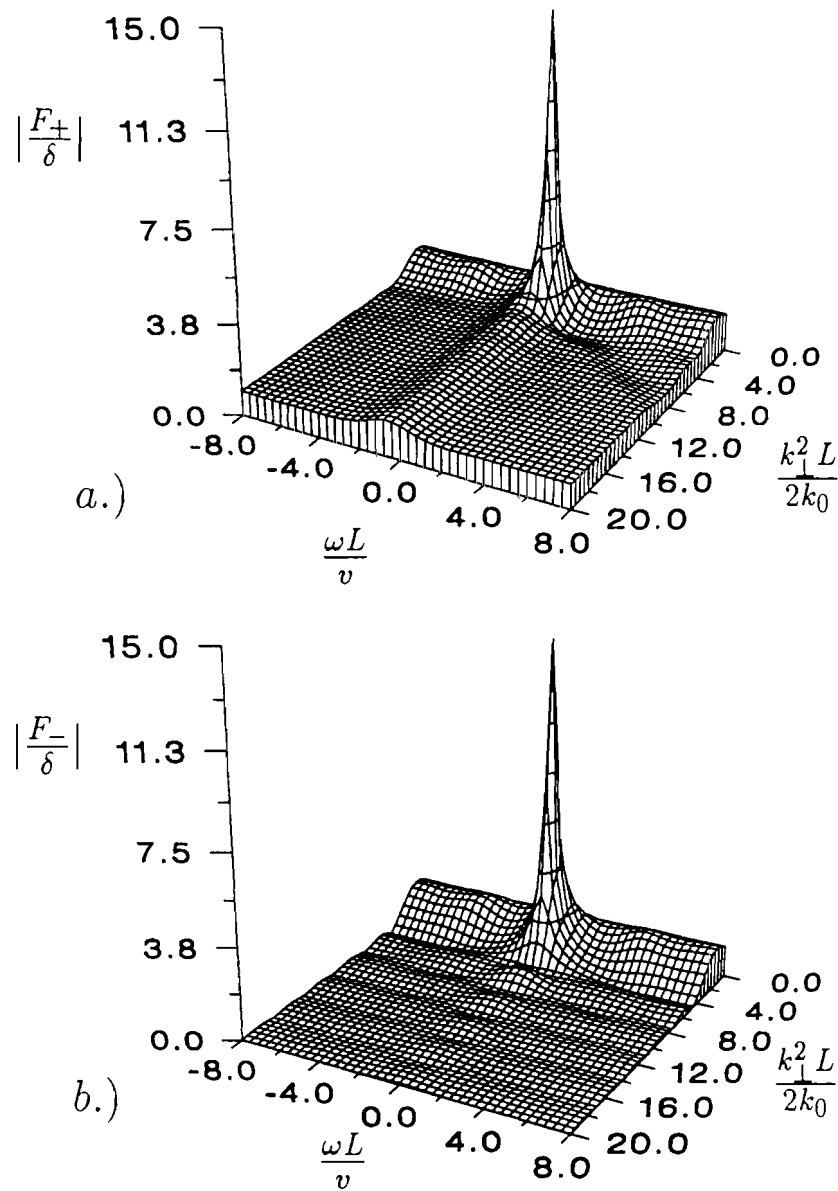


Figure 4.6: The linear convective gain spectrum for the four-sideband interaction is plotted in the plane of the real part of the perturbation frequency, $\text{Re}(\omega L/v)$, and the transverse perturbation wavenumber parameter, $k_{\perp}^2 L/2k_0$, for the case in which $\sigma = 1$, $\epsilon = 2.0$, $r^2 = 0.1$ and $P = 0.95P_{th} = 1.290$. The forward anti-Stokes sideband was seeded by $F_+(0) = \delta = 0.001$. Shown are the (a.) F_+ , and (b.) F_-^* sidebands.

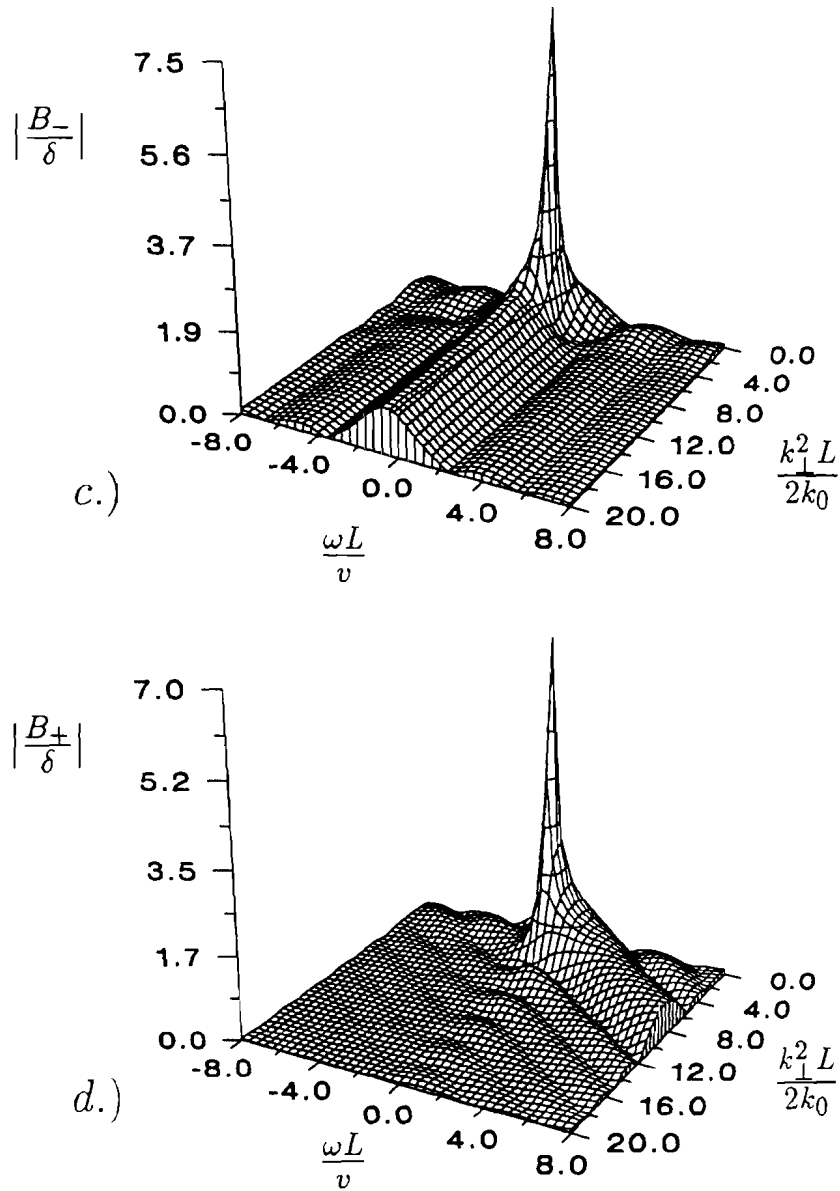


Figure 4.6: (continued) The linear convective gain spectrum for the four-sideband interaction is plotted in the plane of the real part of the perturbation frequency, $\text{Re}(\omega L/\nu)$, and the transverse perturbation wavenumber parameter, $k_{\perp}^2 L/2k_0$, for the case in which $\sigma = 1$, $\epsilon = 2.0$, $r^2 = 0.1$ and $P = 0.95P_{th} = 1.290$. The forward anti-Stokes sideband was seeded by $F_{+}(0) = \delta = 0.001$. Shown are the (c.) B_{-}^* , and (d.) B_{+} sidebands.

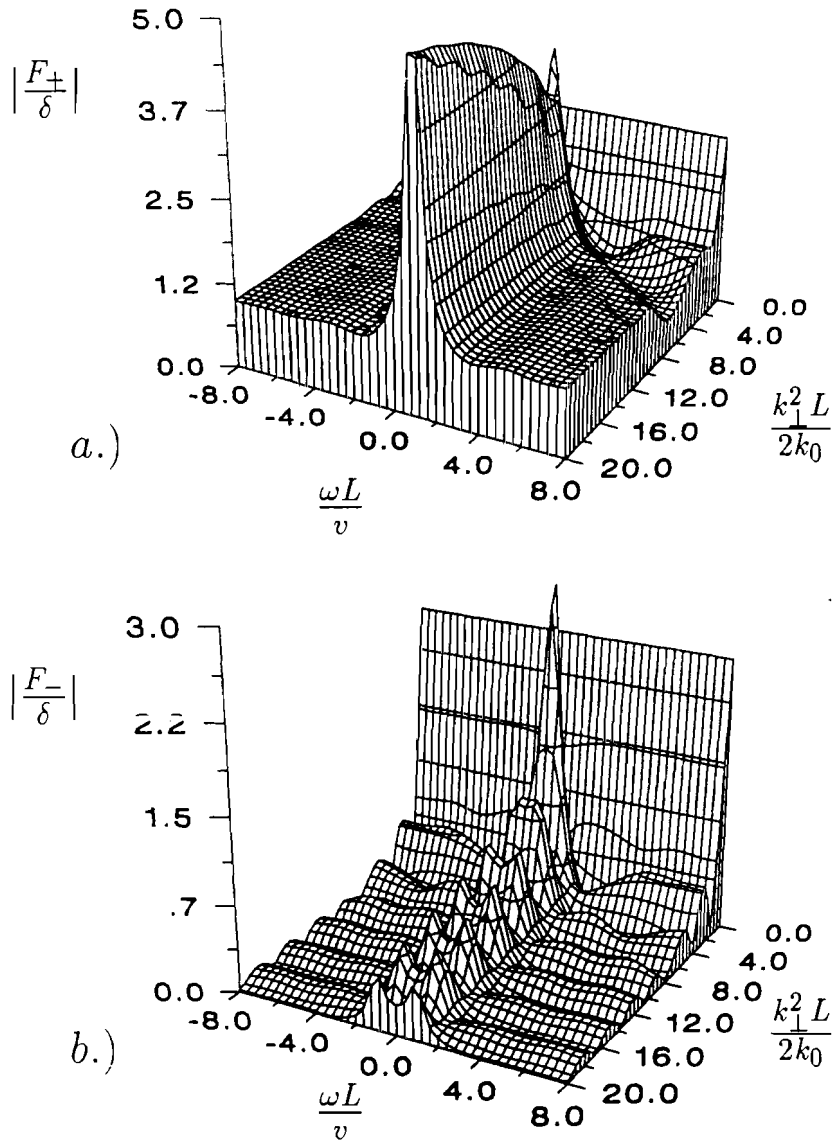


Figure 4.7: The linear convective gain spectrum for the four-sideband interaction is plotted in the plane of the real part of the perturbation frequency, $\text{Re}(\omega L/v)$, and the transverse perturbation wavenumber parameter, $k_{\perp}^2 L/2k_0$, for the case in which $\sigma = -1$, $\epsilon = 2.0$, $r^2 = 0.1$ and $P = 0.95P_{th} = 2.360$. The forward anti-Stokes sideband was seeded by $F_+(0) = \delta = 0.001$. Shown are the (a.) F_+ , and (b.) F_-^* sidebands.

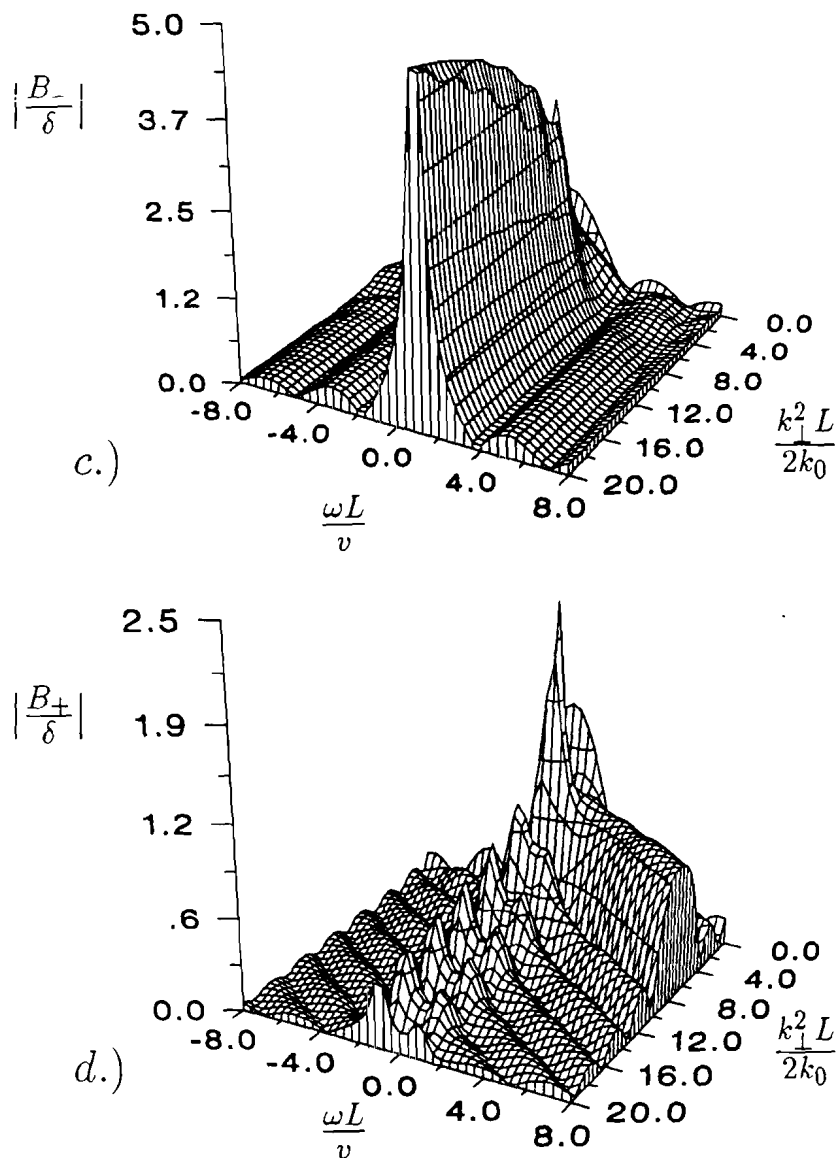


Figure 4.7: (continued) The linear convective gain spectrum for the four-sideband interaction is plotted in the plane of the real part of the perturbation frequency, $\text{Re}(\omega L/\nu)$, and the transverse perturbation wavenumber parameter, $k_{\perp}^2 L/2k_0$, for the case in which $\sigma = -1$, $\epsilon = 2.0$, $\tau^2 = 0.1$ and $P = 0.95P_{th} = 2.360$. The forward anti-Stokes sideband was seeded by $F_+(0) = \delta = 0.001$. Shown are the (c.) B_-^* , and (d.) B_+ sidebands.

The four-sideband instability can also dominate the two-sideband instabilities when the system is pumped asymmetrically. In Figs. 4.6–4.9 the pump fields have different intensities, and $r^2 = 0.1$. While this introduces several interesting differences, the major features displayed in Figs. 4.4–4.5 remain intact. In Figs. 4.6–4.7 the seed sideband is injected at the input face of the strong pump field. Figures 4.6 show that the four-sideband instability continues to dominate in self-focusing media even when $r^2 \neq 1$. Figures 4.7 show that the four-sideband instability for self-defocusing media is dominated by the phase conjugate gain when $r \ll 1$. At the same time, Fig. 4.7(c) shows that this phase conjugate gain is increased and the peak is frequency down-shifted. This shift is expected for phase conjugation and is also given by Eq. (4.31). These shifts also occur in the self-focusing case, but they are not visible in Figs. 4.6. As discussed in Sec. 3, for $k_{\perp}^2 L/2k_0 = 0$ the interaction of F_+ with F_-^* yields no net gain despite the appearance to the contrary in Figs. 4.7.

Finally, in Figs. 4.8–4.9, F_0 is the weak pump, so the interaction is seeded at the input face of the weak pump. The four-sideband gain has the same location, but it is reduced. The phase-conjugate gain shown in Fig. 4.9(c) is nearly the same as in Fig. 4.6(c) where the instability was seeded from the input face of the strong pump, but as expected, the frequency shift has the opposite sign. As the pump intensity ratio r^2 approaches zero, the four-sideband interaction is detuned, leaving only the forward FWM interaction of the two uncoupled pump waves. In this small r^2 limit the depletion of the weak pump becomes important, so nonlinear coupling terms must be retained.

In the convective regime a four-sideband instability exists which dominates the well known two-sideband instabilities in both self-focusing and self-defocusing media. This instability continues to dominate for a large range of the backward

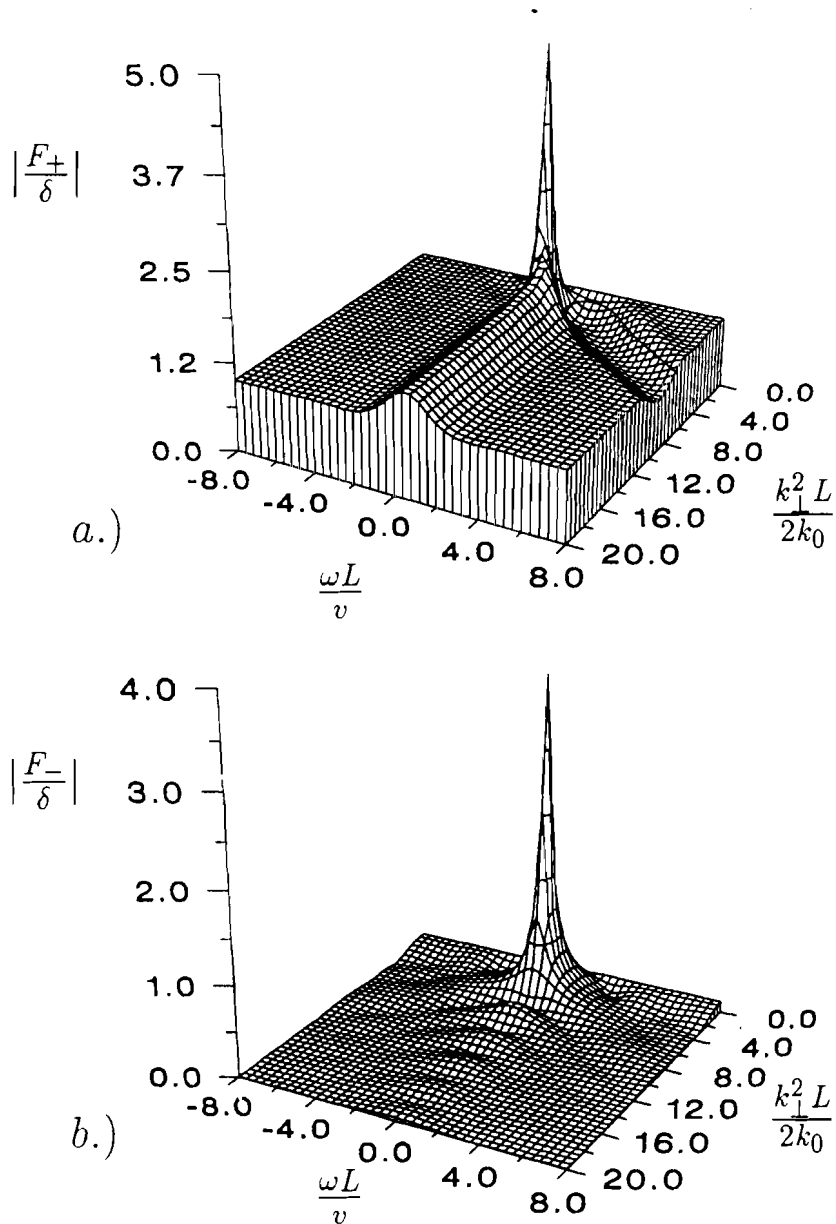


Figure 4.8: The linear convective gain spectrum for the four-sideband interaction is plotted in the plane of the real part of the perturbation frequency, $\text{Re}(\omega L/v)$, and the transverse perturbation wavenumber parameter, $k_{\perp}^2 L/2k_0$, for the case in which $\sigma = 1$, $\epsilon = 2.0$, $r'^2 = 10.0$ and $P = 0.95r^2 P_{th} = 0.129$. The forward anti-Stokes sideband was seeded by $B_+(1) = \delta = 0.001$. Shown are the (a.) F_+ , and (b.) F_-^* sidebands.

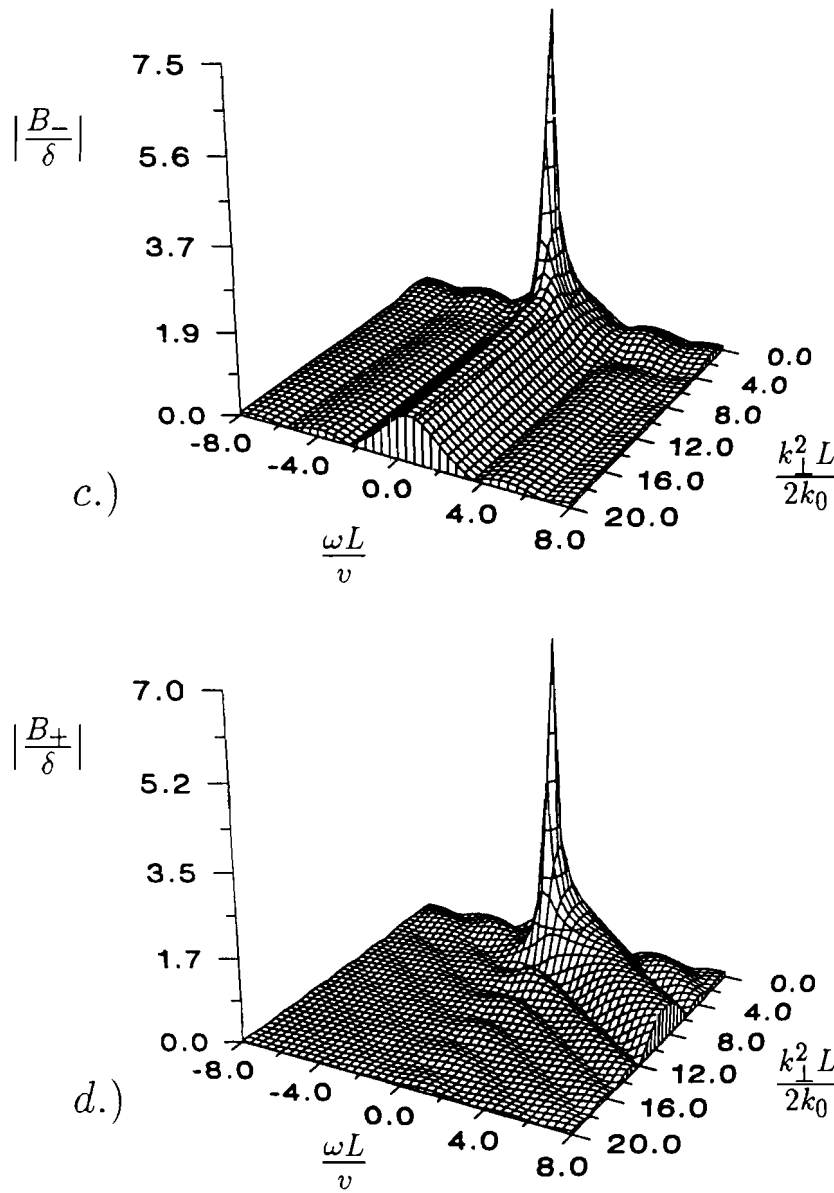


Figure 4.8: (continued) The linear convective gain spectrum for the four-sideband interaction is plotted in the plane of the real part of the perturbation frequency, $\text{Re}(\omega L/v)$, and the transverse perturbation wavenumber parameter, $k_{\perp}^2 L/2k_0$, for the case in which $\sigma = 1$, $\epsilon = 2.0$, $r'^2 = 10.0$ and $P = 0.95r^2 P_{th} = 0.129$. The forward anti-Stokes sideband was seeded by $B_{+}(1) = \delta = 0.001$. Shown are the (c.) B_{-}^* , and (d.) B_{+} sidebands.

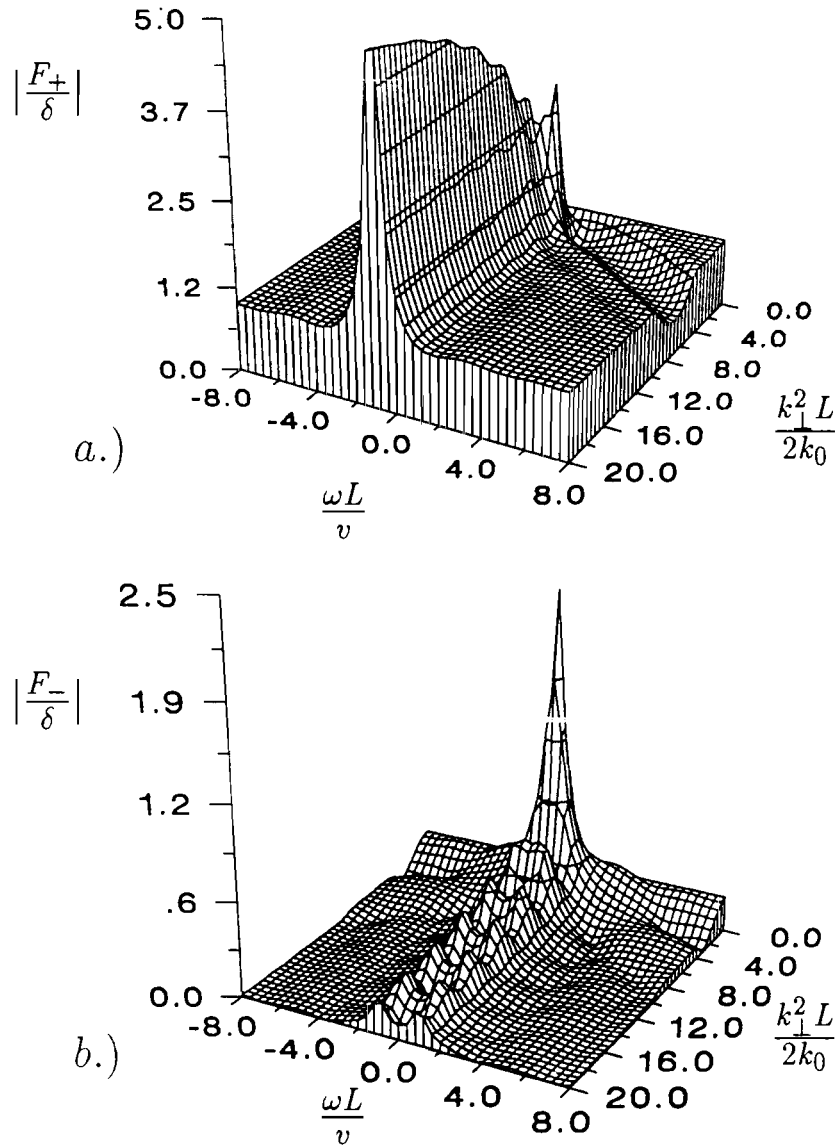


Figure 4.9: The linear convective gain spectrum for the four-sideband interaction is plotted in the plane of the real part of the perturbation frequency, $\text{Re}(\omega L/v)$, and the transverse perturbation wavenumber parameter, $k_{\perp}^2 L/2k_0$, for the case in which $\sigma = -1$, $\epsilon = 2.0$, $r'^2 = 10.0$ and $P = 0.95r^2 P_{th} = 0.236$. The forward anti-Stokes sideband was seeded by $B_+(1) = \delta = 0.001$. Shown are the (a.) F_+ , and (b.) F_-^* sidebands.

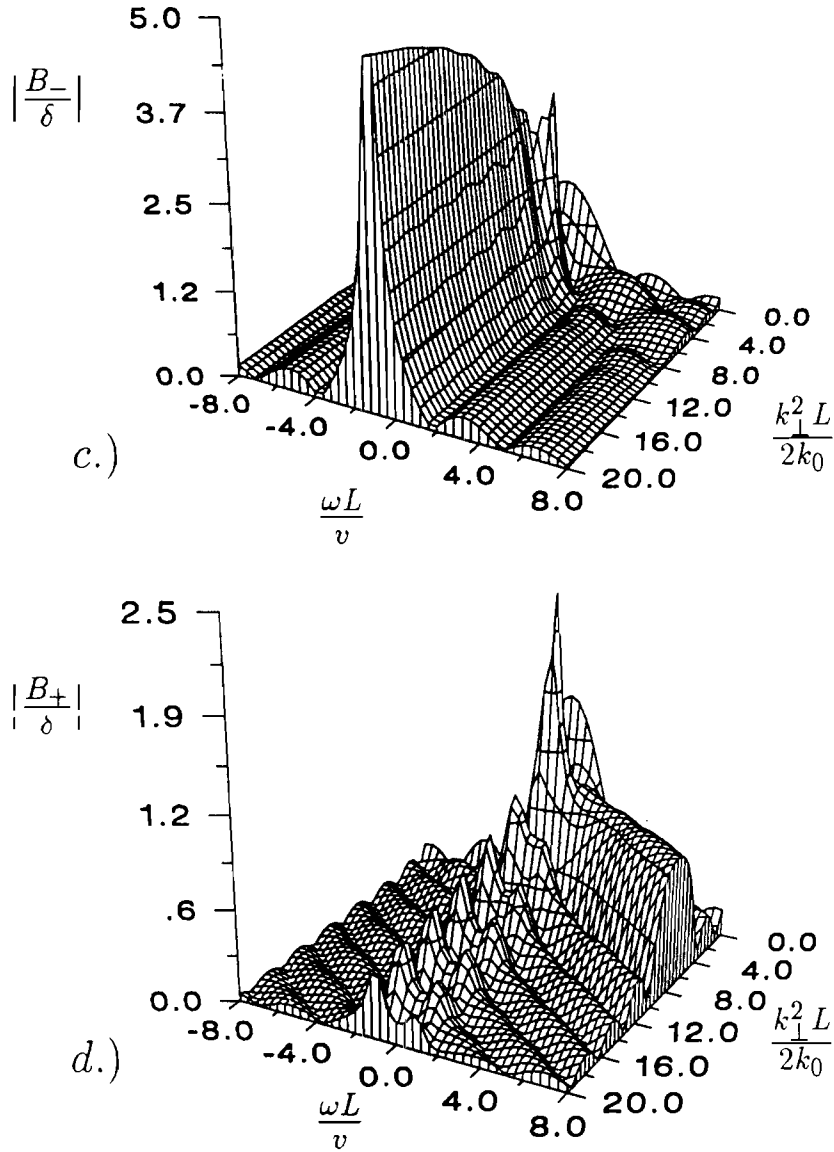


Figure 4.9: (continued) The linear convective gain spectrum for the four-sideband interaction is plotted in the plane of the real part of the perturbation frequency, $\text{Re}(\omega L/v)$, and the transverse perturbation wavenumber parameter, $k_{\perp}^2 L/2k_0$, for the case in which $\sigma = -1$, $\epsilon = 2.0$, $r'^2 = 10.0$ and $P = 0.95r^2 P_{th} = 0.236$. The forward anti-Stokes sideband was seeded by $B_+(1) = \delta = 0.001$. Shown are the (c.) B_-^* , and (d.) B_+ sidebands.

to forward pump intensity ratio, r^2 . In addition, the gain spectrum of the four-sideband TMI is displaced with respect to the single-wave TMI. At small r^2 , the phase conjugate interaction dominates in self-defocusing media.

4.2.2 The Absolute Instability Threshold

The absolute instability threshold condition is given by $\Delta = 0$. In the two cases where the eigenvalue relation for M , Eq. (4.53), is biquadratic, the threshold equation, Eq. (4.59), can be written in a simpler form. When $\omega = 0$, $\Delta = \Delta_{\omega=0}$ of Eq. (4.63). This equation was reported by Grynberg and Paye [48], and an equivalent equation was given in Refs. [50, 51]. When $r = 1$, $\Delta = \Delta_{r=1}$ of Eq. (4.68). Vlasov and Sheinina [45], Firth and Penman [53], and Luther, McKinstrie and Gaeta [54] each obtained analytical threshold equations for the $r = 1$ case. When both $r = 1$ and $\omega = 0$, the result stated by Vlasov and Talanov [44] and by Firth and Paré [46] is obtained.

When multiple eigenvalues occur, Eq. (4.59) is identically zero even if no instability exists, so the threshold condition must be calculated using Eq. (4.52) with the canonical forms of U and Q . This is not merely a mathematical point, for in complicated systems these multiple eigenvalues can arise. Gaeta [87] has encountered such difficulties in studies of combined polarization-diffraction instabilities.

When $\omega = 0$, there are two ways in which degenerate eigenvalues occur. Recall that the eigenvalues for this case were given in Eq. (4.60). That equation allows only one pair of eigenvalues to become degenerate at once. Thus, when either k_+ or k_- is zero,

$$k_{\perp}^2 = (1 + r^2)P \pm P[(1 - r^2)^2 + (2r\epsilon)^2]^{\frac{1}{2}}. \quad (4.69)$$

While $\Delta = 0$ is no longer the threshold condition when these repeated eigenvalues occur,

$$\Delta'_{\omega=0} = \frac{\Delta}{k_+ k_-}, \quad (4.70)$$

and the modified threshold condition is $\Delta'_{\omega=0} = 0$ [46]. When $r = 1$ there are three ways in which degenerate eigenvalues occur. The eigenvalues for this case are stated in Eq. (4.65). All four eigenvalues become zero when $\omega^2 = \kappa$ and $r^2 = (\kappa/\epsilon P k_{\perp}^2)^2$. One of the two cases $k_{\pm}^2 = 0$ occurs when

$$\omega^2 - \kappa \pm 2[(\epsilon r P k_{\perp}^2)^2 - \kappa \omega^2]^{\frac{1}{2}} = 0. \quad (4.71)$$

Finally, $k_+ \rightarrow k_- \neq 0$ when $k_{\perp}^2 = 2P\omega^2/[\omega^2 + (\epsilon r P)^2]$, and the two degenerate pairs of eigenvalues take the values $k_{\pm}^2 = \omega^2 - \kappa$. At these points, the occurrence of degenerate eigenvalues must be taken into account.

In general, the threshold for absolute instability in the four-sideband system may be calculated numerically based on the eigenvectors in Eq. (4.51). Typical examples of this technique may be found in [32, 33]. An alternate scheme which treats multiple roots properly is discussed in the Appendix.

Solutions for $\Delta_{\omega=0} = 0$ are displayed in Figs. 4.10 - 4.12, for σ equal to 1 and several values of r^2 . Each curve corresponds to the threshold condition for a different eigenmode. Whenever $\sigma\lambda|F_0|^2 L/v$ exceeds its minimal threshold value, at least one of the spatial eigenmodes is unstable. Figure 4.10(a) corresponds to the case in which $r^2 = 1.0$. The minimal threshold value of $\sigma\lambda|F_0|^2 L/v$ is 0.45, corresponding to a value of $k_{\perp}^2 L/2k_0$ equal to 3.0, and the threshold intensities for the two lowest-order spatial eigenmodes tend to the phase-conjugate oscillation threshold for large values of the transverse wavenumber, in complete agreement with the results of Vlasov and Talanov, and Firth and Paré. Notice that, for

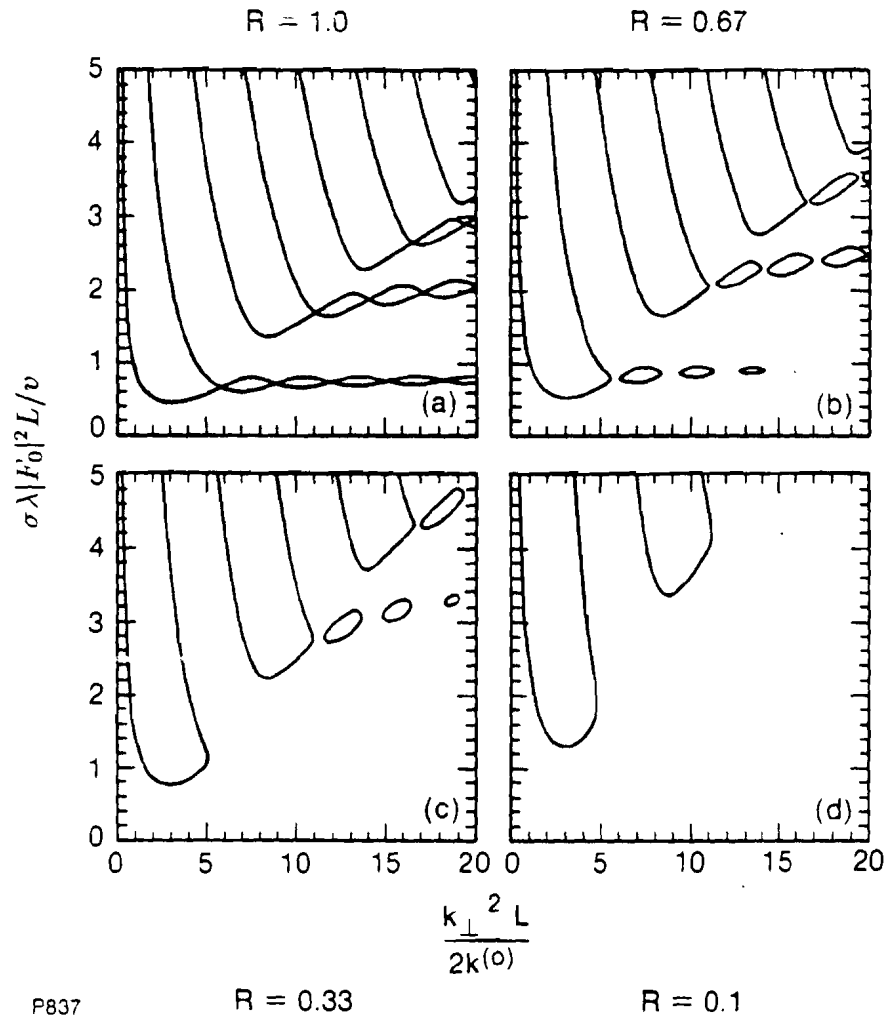
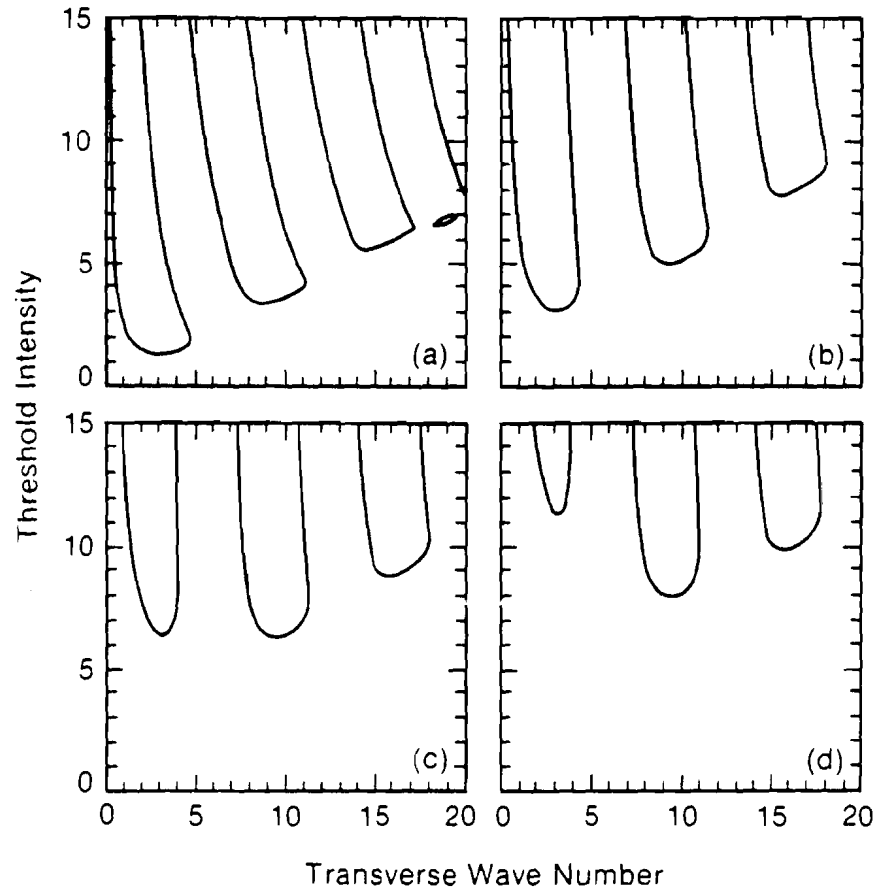


Figure 4.10: The static absolute intensity threshold $\sigma\lambda|F_0|^2L/v$ in a finite medium is plotted as a function of the transverse wavenumber $k_{\perp}^2 L/2k_0$, for the case in which $\sigma = 1$, and $\epsilon = 2$. (a) $r^2 = 1.00$. (b) $r^2 = 0.67$. (c) $r^2 = 0.33$. (d) $r^2 = 0.10$.

counterpropagating waves, the range of unstable transverse wavenumbers is unbounded, in contrast to the results of Sec. 3.1 for copropagating waves.

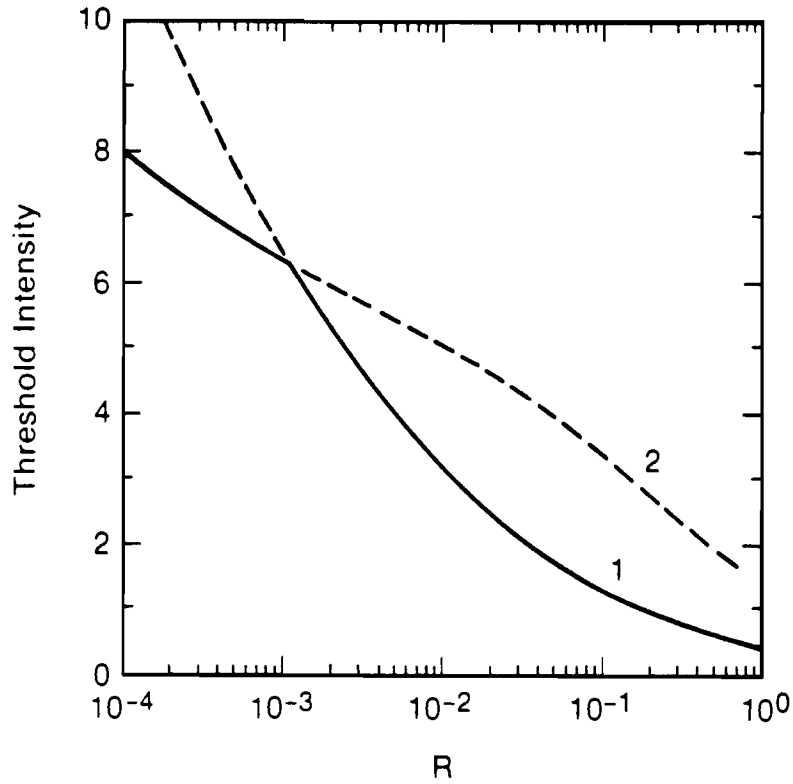
It can be seen from Figs. 4.10(b) – 4.10(d), for which r^2 is equal to 0.67, 0.33 and 0.10, respectively, that the topology of the threshold curves is rather complicated. However, for values of r^2 less than about 0.10, the ellipsoidal structures disappear and the static threshold is characterized by the presence of disjoint “lobes” at small transverse wavenumbers. Since the threshold value of $\sigma\lambda|F_0|^2L/v$ corresponding to phase-conjugate oscillation is equal to $\pi/2\epsilon r$, the absence of such a feature in Fig. 4.10(d) implies that the TMI is oscillatory for large values of the transverse wavenumber. However, the minimal static-threshold value is $\sigma\lambda|F_0|^2L/v = 1.3$ in Fig 4.10(d), which is significantly less than the phase-conjugate oscillation threshold of 2.5.

Solutions are displayed for a wider range of r^2 in Fig. 4.11. When $r^2 = 10^{-1}$ and 10^{-2} , the point corresponding to the minimal static-threshold intensity is located on the leftmost lobe. When r^2 is equal to 10^{-3} , the lowest points on the leftmost and middle lobes correspond to comparable static-threshold intensities and, when $r^2 = 10^{-4}$, the point corresponding to the minimal static-threshold intensity is located on the middle lobe. Throughout this range of r^2 , the lowest point on the leftmost lobe corresponds to a value of $k_{\perp}^2 L/2k_0$ which is approximately equal to 3.0 and the lowest point on the middle lobe corresponds to values of $k_{\perp}^2 L/2k_0$ which are reasonably close to 9.0. The static-threshold intensities corresponding to these specific values of the transverse wavenumber are plotted as functions of r^2 in Fig. 4.12. Although the static-threshold intensity increases as r^2 decreases, it does so much less rapidly than the threshold intensity for phase-conjugate oscillation, which increases as $1/r$. A more general analysis, which allows for nonzero ω_r , [88], shows that there exists an oscillatory branch of the instability with threshold



P836

Figure 4.11: The static absolute intensity threshold $\sigma\lambda|F_0|^2L/v$ in a finite medium is plotted as a function of the transverse wavenumber $k_1^2L/2k_0$, for the case in which $\sigma = 1$ and $\epsilon = 2$. (a) $r^2 = 10^{-1}$. (b) $r^2 = 10^{-2}$. (c) $r^2 = 10^{-3}$. (d) $r^2 = 10^{-4}$.



P838

Figure 4.12: The static absolute intensity threshold $\sigma\lambda|F_0|^2L/v$ is plotted as a function of the pump-wave intensity ratio r^2 , for the case in which $\sigma = 1$ and $\epsilon = 2$. Curve 1 corresponds to a transverse wavenumber $k_{\perp}^2L/2k_0$ of 3.0, while curve 2 corresponds to a transverse wavenumber $k_{\perp}^2L/2k_0$ of 9.0. The static threshold intensity is the envelope of these two curves, denoted by the solid line.

intensities which are lower than the static-threshold intensities for r^2 less than about 10^{-2} ; the threshold intensities obtained from Fig. 4.12 should therefore be regarded as upper bounds on the true threshold intensities. Hence, when $\sigma = 1$, the threshold intensities for the static branches of the TMI are significantly lower than that for phase-conjugate oscillation [89].

Solutions of $\Delta_{\omega=0} = 0$ are displayed in Fig. 4.13, for σ equal to -1 and several values of r^2 . The topology of the threshold curves is qualitatively similar to that of Fig. 4.10. When r^2 is close to 1.0, the lowest point on the threshold curves is located at small wavenumbers, although the difference between the static-instability threshold intensity and the threshold intensity for phase-conjugate oscillation is smaller than in the previous example. As r^2 is decreased, the ellipsoidal structure disappears and the static instability is again characterized by disjoint lobes at small wavenumbers. However, for values of r^2 less than about 0.10, the static-threshold intensity exceeds the threshold intensity for phase-conjugate oscillation and, hence, the TMI is of less importance than in the previous example.

The TMI of two counterpropagating waves has been studied independently by Grynberg and Paye [48]. Grynberg and Paye derived an equation for the static threshold which allows for unequal wave intensities. The threshold curves they obtained for r equal to 1.0 and 0.85 agree with the corresponding threshold curves determined from $\Delta_{\omega=0} = 0$, to the displayed accuracy. In comparing Figs. 4.10 and 4.13 to the corresponding figures of Grynberg and Paye, the reader should note that Grynberg and Paye use $|F_0 B_0|$ as their measure of wave intensity, whereas $|F_0|^2$ is used throughout this thesis.

In Sec. 3.1, it was shown that the effects of linear wave damping can alter the evolution of two copropagating waves significantly. Likewise, the intensity threshold for the instability of counterpropagating waves in a finite medium de-

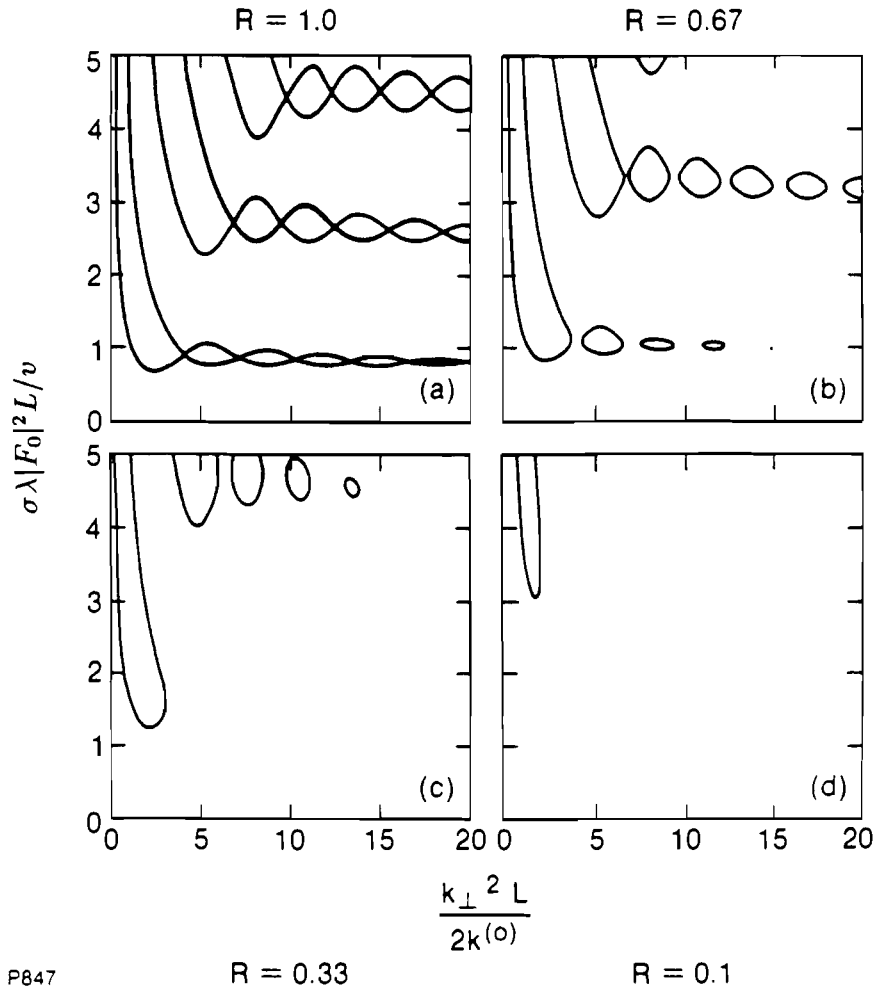


Figure 4.13: The static absolute intensity threshold $\sigma \lambda |F_0|^2 L / \nu$ in a finite medium is plotted as a function of the transverse wavenumber $k_{\perp}^2 L / 2k_0$, for the case in which $\sigma = -1$, and $\epsilon = 2$. (a) $r^2 = 1.00$. (b) $r^2 = 0.67$. (c) $r^2 = 0.33$. (d) $r^2 = 0.10$.

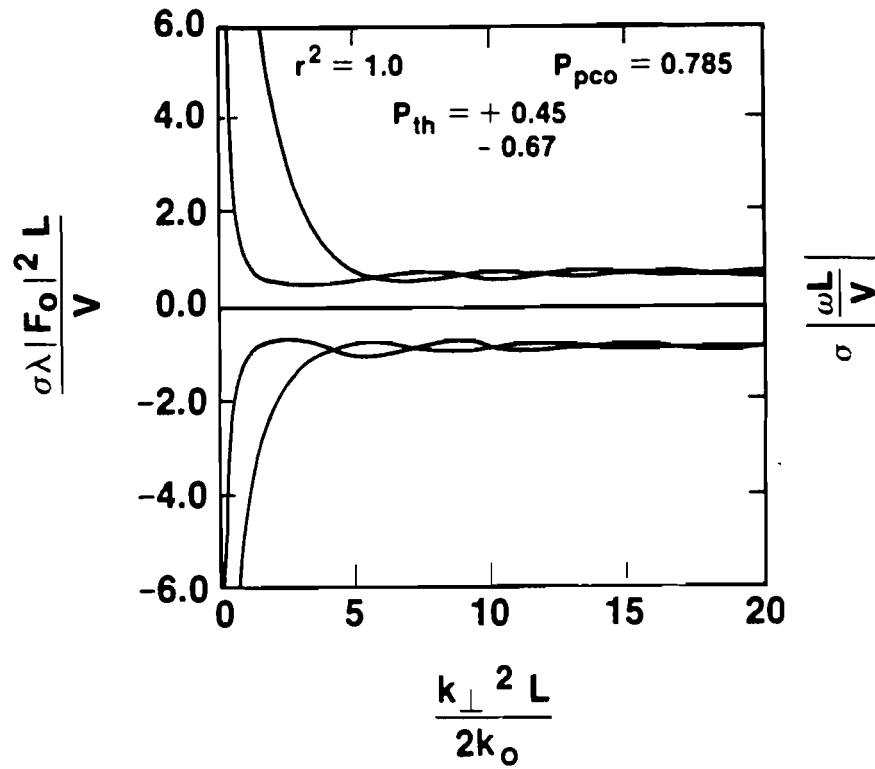
pends sensitively on the wave-damping coefficients. In the presence of linear wave damping, $|A_1(z)| \longrightarrow |A_1(0)| \exp(-\nu z/v)$ and $|A_2(z)| \longrightarrow |A_2(l)| \exp[\nu(z-l)/v]$. The self-nonlinear terms in Eq. (3.43) are no longer independent of position, which makes the determination of the threshold intensity more difficult. However, a crude estimate of the threshold intensity in the presence of linear wave damping can be made by replacing $|A_1(z)|$ and $|A_2(z)|$ by their average values $|A_1(0)| \exp(-\nu l/2v)$ and $|A_2(l)| \exp(-\nu l/2v)$, respectively. When $\nu l/v$ is much less than unity, the effects of wave damping are less important than the boundary effects and the threshold intensities found previously should approximate the true threshold intensities. When $\nu l/v$ is much greater than unity, the boundary effects are less important than the effects of wave damping and the threshold intensities can be estimated from the infinite-medium results of Sec. 3.2. It follows from Eq. (3.31) that the threshold condition is

$$(\gamma_{\pm} l/v) \sim (\nu l/v) \exp(\nu l/v) , \quad (4.72)$$

where γ_{\pm} are the temporal growth rates determined in terms of $|A_1(0)|$ and $|A_2(l)|$ by Eqs. (3.25) and (3.27).

These results show clearly that the threshold intensity of the TMI depends sensitively on the static or oscillatory nature of the instability, the transverse wavenumber of the perturbed wave amplitude, and the linear wave-damping coefficients. The threshold intensity can also be reduced by reflective boundaries [90]. In the remainder of this section the behavior of the absolute instability threshold when ω_r is not fixed at zero is illustrated.

In Figs. 4.14 and 4.15, the threshold for absolute instability of the four-sideband interaction is displayed. The topmost curves are the threshold curves for self-focusing, $\sigma > 0$. Below these threshold curves, but in the same half



P897

Figure 4.14: The threshold intensity for absolute instability of the four-sideband system is plotted as a function of the transverse perturbation wavenumber parameter for both self-focusing, $\sigma = 1$ (upper), and self-defocusing, $\sigma = -1$ (lower), media, where $r^2 = 1.0$ and $\epsilon = 2.0$. The line at $\omega L/v = 0$ indicates that the frequency of the absolutely unstable sidebands at threshold is the same as that of the pumps for both self-focusing and self-defocusing media in this case.

plane, the corresponding values of the frequency shifts at threshold are plotted. Similar data is included in the lower half plane for self-defocusing media. Note that, for each sign of σ , the frequency shifts are actually symmetric about the zero-frequency-shift line, though only the upper or lower half of the curves are shown. Pump intensities which have absolute value equal to or larger than the threshold curve make the system absolutely unstable. Below the threshold curves, the system can only be convectively unstable. For both signs of σ , these curves tend to the correct phase-conjugate threshold and frequency shift in the large k_{\perp}^2 limit [54].

The lowest threshold in self-focusing media is located near $k_{\perp}^2 L/2k_0 = 3.0$ for both values of r^2 shown in Figs. 4.14 and 4.15. No frequency shifts arise at these minimal thresholds. For self-defocusing media, the lowest threshold is located below $k_{\perp}^2 L/2k_0 = 3.0$ when $r^2 = 1.0$ with $\omega = 0$, but when $r^2 = 0.1$ the lowest threshold occurs at large $k_{\perp}^2 L/2k_0$ with $\omega_r \neq 0$. The absolute thresholds at low $k_{\perp}^2 L/2k_0$ are due to the four-sideband TMI. This is precisely what is expected based on the near-threshold convective gain. Note that the range of transverse perturbation wave numbers for which this absolute instability dominates is broad, even though the gain spectrum narrows as the power is increased through the convective regime. This result suggests that the spectrum in k_{\perp} should appear to broaden at threshold.

In Fig. 4.16, the minimal absolute instability thresholds are plotted as functions of r^2 for both the four-sideband TMI and the phase-conjugate instability limit. In self-focusing media, the absolute instability threshold for the TMI remains below the phase-conjugate threshold. As r^2 is decreased in self-defocusing media, the value of $k_{\perp}^2 L/2k_0$ corresponding to the minimal threshold first decreases. As r^2 continues to decrease, the original minimum rises above the next

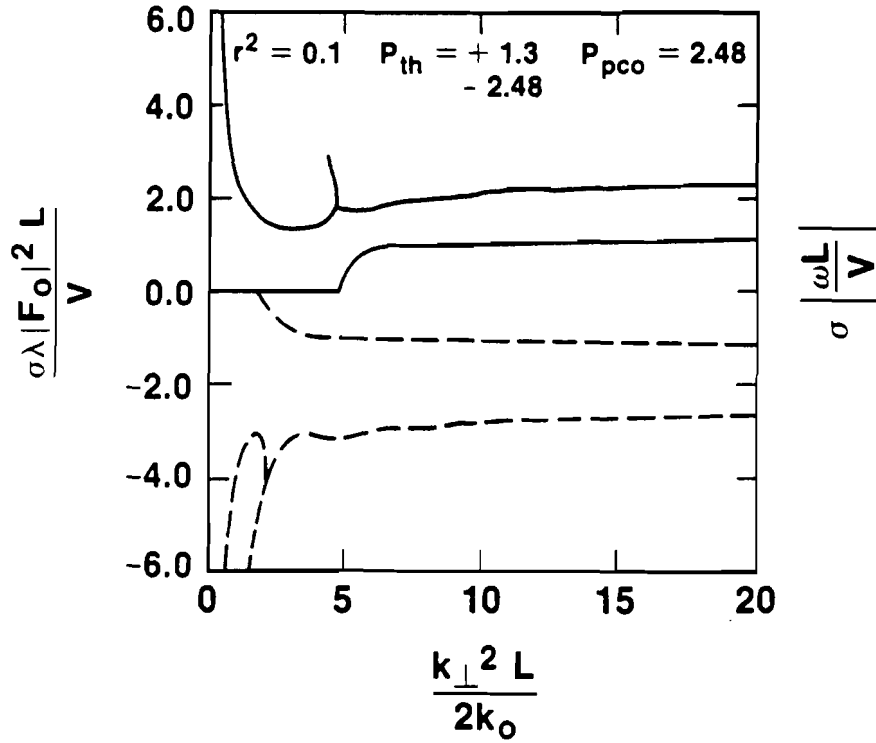
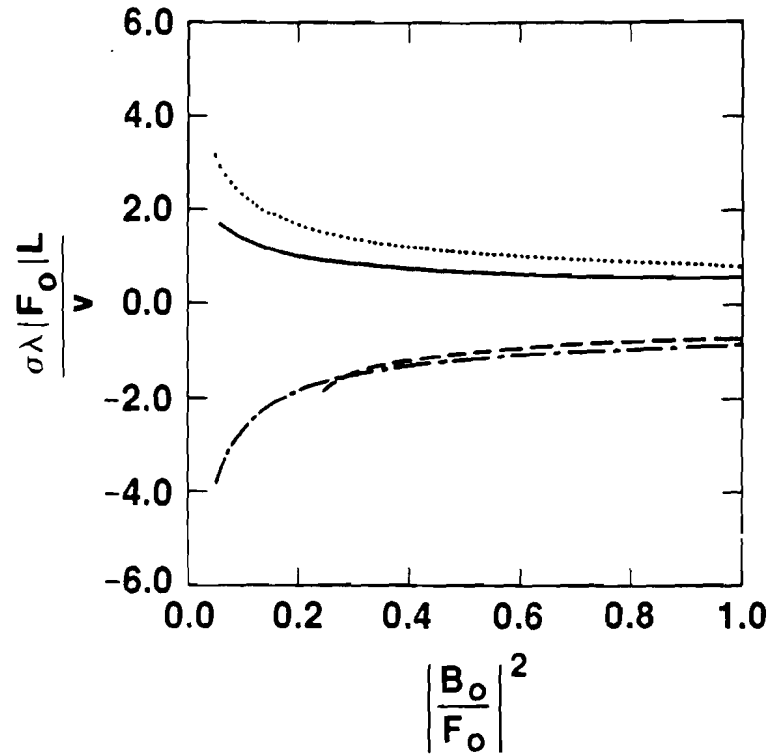


Figure 4.15: The threshold intensity for absolute instability of the four-sideband system is plotted as a function of the transverse perturbation parameter for both self-focusing (—), $\sigma = 1$, and self-defocusing (---), $\sigma = -1$, media, where $r^2 = 0.1$ and $\epsilon = 2.0$. The two lines nearest $\omega L/v = 0$ indicate that the values of the perturbation frequencies at threshold become finite when the pumps intensities are unequal.



P1050

Figure 4.16: The minimum absolute instability threshold is plotted as a function of the pump intensity ratio r^2 , for (—) $\sigma = 1$ and $k_{\perp}^2 L/2k_0 \approx 3.0$, (•••) $\sigma = 1$ and $k_{\perp}^2 L/2k_0 \approx 20$, (— — —) $\sigma = -1$ and $k_{\perp}^2 L/2k_0 \approx 2.5$, and (• — — •) $\sigma = -1$ and $k_{\perp}^2 L/2k_0 \approx 20$.

relative minimum at a larger $k_{\perp}^2 L/2k_0$. This process continues as r^2 is decreased until the absolute threshold for the phase-conjugate interaction is the minimal threshold [54]. This transition takes place near $r^2 = 0.25$ as shown in Fig. 4.16. The threshold for absolute phase conjugation instability is $\sigma\pi/2\epsilon r$. Over a significant fraction of r^2 in both self-focusing and self-defocusing media, the four-sideband TMI is dominant. As r^2 becomes small this instability remains absolutely unstable, but in self-defocusing media the absolute instability of the two-sideband phase-conjugate limit dominates.

4.3 Summary

It has been shown that the system of counterpropagating light waves studied here has a four-sideband TMI in the spectral overlap region of forward FWM, phase conjugation, and Bragg scattering. In the limits where the sidebands have large transverse wave number, k_{\perp}^2 , large frequency shift, ω_r , or large $\omega_r \pm k_{\perp}^2$, the four-sideband instability is detuned and its three limiting two-sideband interactions are recovered. Solutions for the linear gain spectrum and the absolute instability threshold of the four-sideband problem have been provided both analytically and numerically. These solutions show that the four-sideband instability dominates for a significant range of backward to forward intensity ratios, r^2 , both as a convective instability and as an absolute instability in both self-focusing and self-defocusing media. The phase-conjugate instability becomes important as r^2 is reduced and is the dominant absolute instability for $r^2 < 0.25$ in self-defocusing media. The analysis of the four-sideband interaction reveals the properties of the four-sideband instability and its relationship to three distinct two-sideband interactions which are based on FWM processes.

Both four-sideband and single-wave TMI have a distinct band of transverse wave numbers for which their gain is optimized. As a result, the spatial distribution of light in the far field can contain a ring that is a signature of the instability. The phase-conjugation instability is independent of the transverse modulational wave number and, by itself, is not responsible for structure in the transverse intensity profile. Recent observations of conical light emission in sodium vapor [47, 49, 52, 91] are consistent with the theory of the TMI of counterpropagating waves described above. In addition, the competition between the phase-conjugate gain and other convective or absolute instabilities is important for high-gain phase-conjugation applications, since the four-sideband TMI can dominate the phase conjugation interaction.

Appendix 4: Numerical Calculation of the Absolute Threshold

There are several ways to obtain the absolute instability threshold numerically. One relatively quick way is to assume that the eigenfunctions are exponentials. The zeroes of the solvability condition for the coefficients are then obtained using a multidimensional Newton-Raphson routine. This method will, of course, yield erroneous results when multiple eigenvalues become important. A scheme which accounts for multiple eigenvalues is described below. Though this scheme is more computationally intensive, it is useful for local investigations.

The solution of the eigenvalue problem has the form

$$\vec{A}(\xi) = E(\xi)\vec{a}, \quad (4A.1)$$

where \vec{a} is the set of coefficients which are defined by the boundary conditions.

By specifying a complete set of linearly-independent initial conditions,

$$\vec{A}(0) = E(0)\vec{a} , \quad (4A.2)$$

which map into the solution space and span that entire space, $\vec{A}(1)$ can be calculated by integrating the equations over the length of the medium. Thus,

$$\vec{A}(1) = E(1)\vec{a} , \quad (4A.3)$$

where $\vec{A}(1)$ spans the entire solution space. A new matrix E' is then defined by

$$E'M_{\vec{a}} = [T_1E(0) + T_0E(1)]M_{\vec{a}} , \quad (4A.4)$$

where $M_{\vec{a}}$ is the matrix of coefficients determined by the initial conditions. Now, since the terms in the right hand side of Eq. (4A.4) have been calculated,

$$|E' ||M_{\vec{a}}| = |E'M_{\vec{a}}| , \quad (4A.5)$$

and

$$|M_{\vec{a}}| \neq 0 , \quad (4A.6)$$

the condition that $|E'M_{\vec{a}}| = 0$ is equivalent to

$$|E'| = 0 . \quad (4A.7)$$

Therefore, the zeroes of $|E'M_{\vec{a}}| = 0$ give the absolute instability threshold.

Chapter 5

Resonant Instabilities of Counterpropagating Light Waves

During the interaction of high-power laser fields with plasmas, the plasma density responds to intensity variations. Gratings in the index of refraction form as the laser fields interfere and drive variations in the plasma density. When these gratings are driven nonresonantly, the light waves are governed by the nonlinear Schroedinger equations analyzed in the earlier chapters, where $\sigma > 0$ for plasmas. However, the ion-acoustic modes in a plasma can also be driven by the counterpropagating wave system. This process is analogous to the interaction of light waves with acoustic waves in other Brillouin-active media. In this chapter the gratings are allowed to be driven at their natural frequencies. This modification yields a comparison between the cooperative transverse modulational instability (TMI) and resonant single-wave and cooperative instabilities [92].

The fact that several distinct four-wave mixing (FWM) interactions can coexist in coupled-wave systems is ubiquitous. In the nonresonant system, the four-sideband interaction was the only one requiring more than two sidebands, but in media in which the coupling of the waves has resonant frequency dependence, there may be several situations in which single- and multiple-sideband interac-

tions are simultaneously phase matched forming hybrid interactions which may have characteristics different from those predicted by non-hybrid models. These coupled-wave interactions increase the number of channels by which pump energy can be scattered into sideband modes, making them more virulent than single-wave interactions.

We begin by substituting the expansion of the total field, Eqs. (4.5) and (4.6), into the electromagnetic wave equation (2.9) and the sound wave equation (2.10). The nonlinear current term couples the total field to the plasma and the ion-sound wave equation, Eq. (2.10), governs the motion of low frequency density perturbations in the plasma. These plasma waves are taken to vary on scales no faster than the beat frequency, ω , and no longer than the beat wave number, $|\vec{q}|$. As in the analysis of nonresonant media, linearization yields a set of equations that govern the evolution of the sideband envelopes. In this case however, the response of $\langle n \rangle$ is more complicated. By Fourier-Laplace transforming the linearized equations, the ion-acoustic wave equation becomes

$$\Gamma^{-1}(\vec{q} + i\hat{z}\partial_z, \omega)\langle n \rangle \propto f_L(|A|^2), \quad (5.1)$$

where f_L is the series of linearized terms which arise due to the ponderomotive nonlinearity. We make the usual simplifying assumption that the response of the plasma to the field is local in z [37]. In a homogeneous plasma this approximation is valid when the spatial growth rate of the instability is much smaller than $|\vec{q}|$ and the ion-acoustic damping rate is much larger than $|\vec{q}|$.

The grating Green's function, Γ , then parameterizes the linear resonant response of the ion-wave gratings to the fields. This response, at the beat frequency and wavenumber, is characterized by

$$\Gamma(\omega, k) = \frac{c_s^2 k^2}{\omega^2 + 2i\nu_{ia}\omega - c_s^2 k^2}, \quad (5.2)$$

when $(k\lambda_D)^2 \ll 1$ and $v_i \ll \omega/k \ll v_e$. The parameter ν_{ia} is a phenomenological ion-acoustic damping coefficient, λ_D is the electron Debye length, $v_e(v_i)$ is the electron (ion) thermal speed. More generally, if one takes the beat ponderomotive force to have the same effect as the linear response of the plasma to the force of the charge separation field, the response function is generalized in terms of the electrostatic dielectric function which can be given in terms of the plasma dispersion function [37].

By collecting resonant terms, the coupled mode equations for the four sideband envelopes in a Brillouin-active medium are obtained. They have the form [93]

$$L\vec{A} = N\vec{A}, \quad (5.3)$$

where $\vec{A} = (F_+, F_-^*, B_+, B_-^*)^T$ is the vector containing the envelope amplitudes of the waves, L is their linear propagation matrix, and N is their coupling matrix. The propagation matrix is diagonal having the entries

$$L_{11} = ivd_z + (\omega - c^2 k_\perp^2 / 2\omega_0), \quad (5.4)$$

$$L_{22} = -ivd_z - (\omega + c^2 k_\perp^2 / 2\omega_0), \quad (5.5)$$

where $v = c^2 k_0 / \omega_0$. The entries L_{33} and L_{44} are obtained from L_{11} and L_{22} , respectively by the substitution $v \rightarrow -v$. The coupling matrix has the entries

$$N_{11} = \alpha[\Gamma_\perp |F_0|^2 + (\Gamma_\parallel - 1)|B_0|^2], \quad (5.6)$$

$$N_{12} = \alpha\Gamma_\perp F_0^2, \quad (5.7)$$

$$N_{13} = \alpha(\Gamma_\perp + 1)F_0 B_0^*, \quad (5.8)$$

$$N_{14} = \alpha(\Gamma_\perp + \Gamma_\parallel)F_0 B_0, \quad (5.9)$$

where $\alpha = -Zm_e\omega_e^2 / (8m_i\omega_0c_s^2)$. The remaining terms are $N_{ij} = N_{ji}^*$, $N_{22} = N_{11}$, $N_{23} = N_{14}^*$, $N_{24} = N_{13}$, $N_{33} = N_{44} = N_{11}(|F_0| \leftrightarrow |B_0|)$, and $N_{34} = N_{12}(F_0 \leftrightarrow B_0)$.

The terms in each entry of N correspond to the low frequency response of the plasma to the linearized ponderomotive force of the beating of the fields. The coupling matrix contains two resonant gratings. There is a short wavelength grating, $\Gamma_{\parallel} = \Gamma(\omega, \pm 2\vec{k}_0 + \vec{k}_{\perp})$, having a wave vector which lies nearly parallel to that of the pumps, and a long wavelength grating, $\Gamma_{\perp} = \Gamma(\omega, \vec{k}_{\perp})$, having a wave vector which lies perpendicular to that of the pumps. Terms which are independent of either Γ arise due to the static pump-pump grating.

Single-wave backward stimulated Brillouin scattering (SBS) is mediated by a sound-wave which couples each sideband to its respective counterpropagating pump. Terms in N proportional to $(\Gamma_{\parallel} - 1)$ characterize this interaction. Backward SBS grows as $\gamma L/v = \sqrt{\alpha|F_0|^2 L/v} \sqrt{k_0 L(c_s/c)(c/v)}$ [1, 3]. Single-wave near-forward SBS is mediated by the Γ_{\perp} grating, coupling a pump wave to both its Stokes and anti-Stokes sidebands. For significant gain of the Stokes sideband a finite wave vector mismatch is required to detune the strong mutual interaction of the Stokes and anti-Stokes sidebands. The single-wave filamentation instability is also mediated by the Γ_{\perp} grating, but both sidebands grow and the peak growth occurs when the grating is driven off resonance at $\omega = 0$. Its peak growth rate is $\alpha|F_0|^2$ ($\alpha|B_0|^2$) for the forward (backward) pump.

Cooperative instabilities are driven by the action of both pump waves making the cross terms of matrix N necessary. The two phase conjugation interactions couple Stokes shifted sidebands to their counterpropagating anti-Stokes shifted sidebands through the Γ_{\parallel} , Γ_{\perp} , or the static grating. Two Stokes or two anti-Stokes shifted sidebands couple through either the Γ_{\perp} or $\Gamma(0, 2\vec{k}_0)$ grating due to Bragg scattering by FWM. Though this interaction may be stable by itself, its presence is required to correctly model four-sideband instabilities. The cooperative filamentation of counterpropagating waves is the four-sideband analog

of single-wave filamentation. The simultaneous action of the phase conjugation, Bragg scattering, and single-wave filamentation couplings drives the $\Gamma(0, k_{\perp})$ grating producing a four-sideband instability. Resonant four-sideband instabilities in the one dimensional limit have also been found [35, 36].

These single-wave and cooperative instabilities can be identified in the linear convective gain spectrum of the four sidebands. In Figs. 5.1, the single-pass convective gain of each sideband is plotted as a function of $k_{\perp}^2 L/2k_0$, which is related to the scattering angle, $\theta^2 \approx 2(k_{\perp}^2 L/2k_0)/k_0 L$, and $\text{Re}(\omega L/v)$, which is the real part of the perturbation frequency. The intensities are symmetric, $|B_0|^2 = |F_0|^2$, the ratio $c_s/c = 0.001$, $k_0 L = 1000$ and $\nu_{ia}/\Omega_{ia} = 0.2$, where Ω_{ia} is the ion-acoustic frequency. The pump power is $\alpha|F_0|^2 L/v = 0.43$, which is 0.95 of the minimal absolute threshold intensity for cooperative filamentation. These spectra were calculated by numerically integrating the coupled mode equations (5.3) – (5.9) with $B_{\pm}(L) = 0$, $F_{-}(0) = 0$ and $F_{+}(0) = \delta$, where $F_{+}(0)$ seeds the interaction and $\delta \ll 1$. The peaks in the gain occur where the sidebands are oriented and spectrally tuned such that their linear and nonlinear phase shifts are optimally matched inside the medium. They occur at frequency shifts corresponding to the frequency degenerate gratings, the resonant Γ_{\perp} gratings or the resonant Γ_{\parallel} gratings. At large k_{\perp} the pure phase conjugation interaction of F_{+} with B_{-} due to both resonant and nonresonant gratings is recovered, as seen in Fig. 5.1(d). Near $k_{\perp}^2 = 0$ for $\text{Re}(\omega L/v)$ near neither zero nor one of the ion-acoustic resonances, the single-pump filamentation between F_{+} and F_{-} is recovered and can be seen in Fig. 5.1(b). For $k_{\perp}^2 L/2k_0 \sim \text{Re}(\omega L/v) \gg 1$ in Fig. 5.1(c), the nonresonant Bragg scattering interaction between F_{+} and B_{-} is recovered [55].

For smaller values of k_{\perp}^2 , where $\text{Re}(\omega L/v)$ is near zero or one of the ion-acoustic resonances, the simple one- and two-sideband instabilities overlap causing hybrid

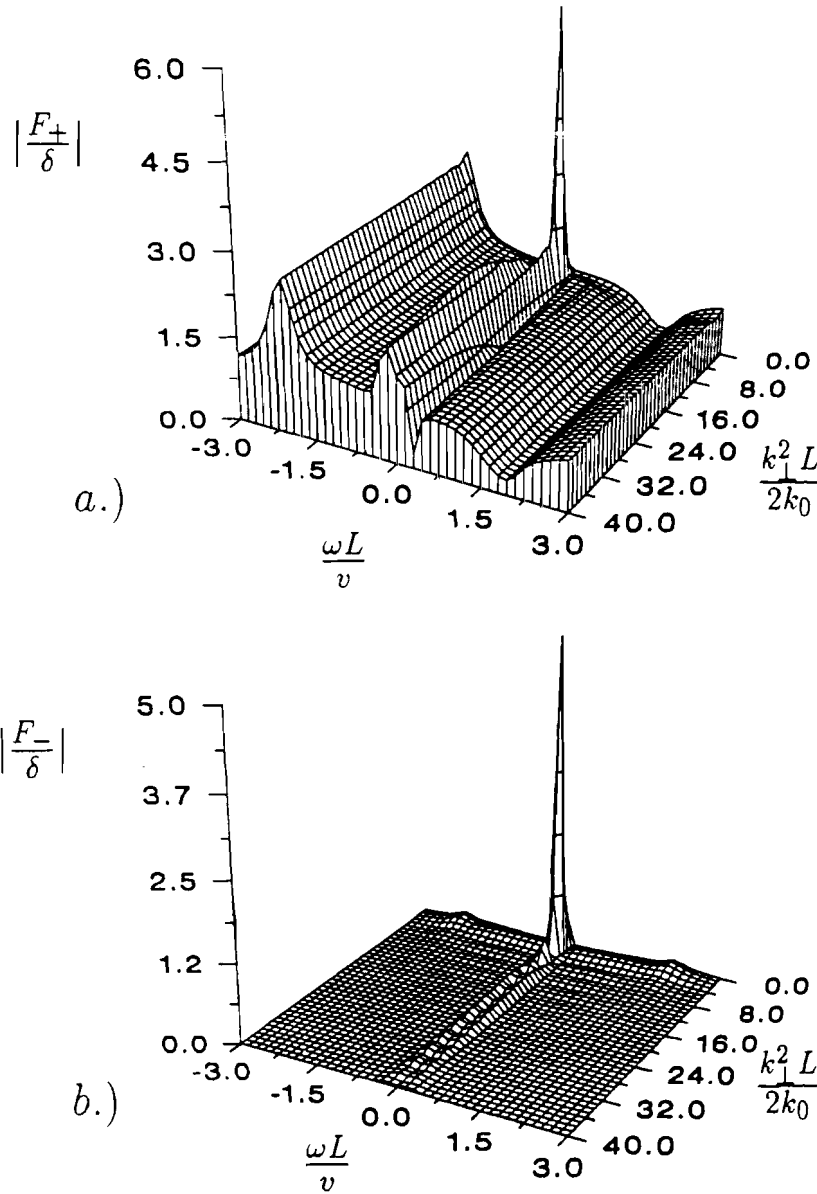


Figure 5.1: The linear convective gain spectrum of the resonant four-sideband interaction is plotted in the plane of the real part of the perturbation frequency, $\text{Re}(\omega L/v)$, and the transverse perturbation wavenumber parameter, where $|B_0|^2 = |F_0|^2$, $c_s/c = 0.001$, $k_0 L = 1000$, $\nu_{ia}/\Omega_{ia} = 0.2$, and $\alpha|F_0|^2 L/v = 0.43$, which is 0.95 of the minimal absolute threshold intensity for cooperative filamentation. The spectra for the seeded sideband (a.) and its forward FWM pair (b.) are plotted here.

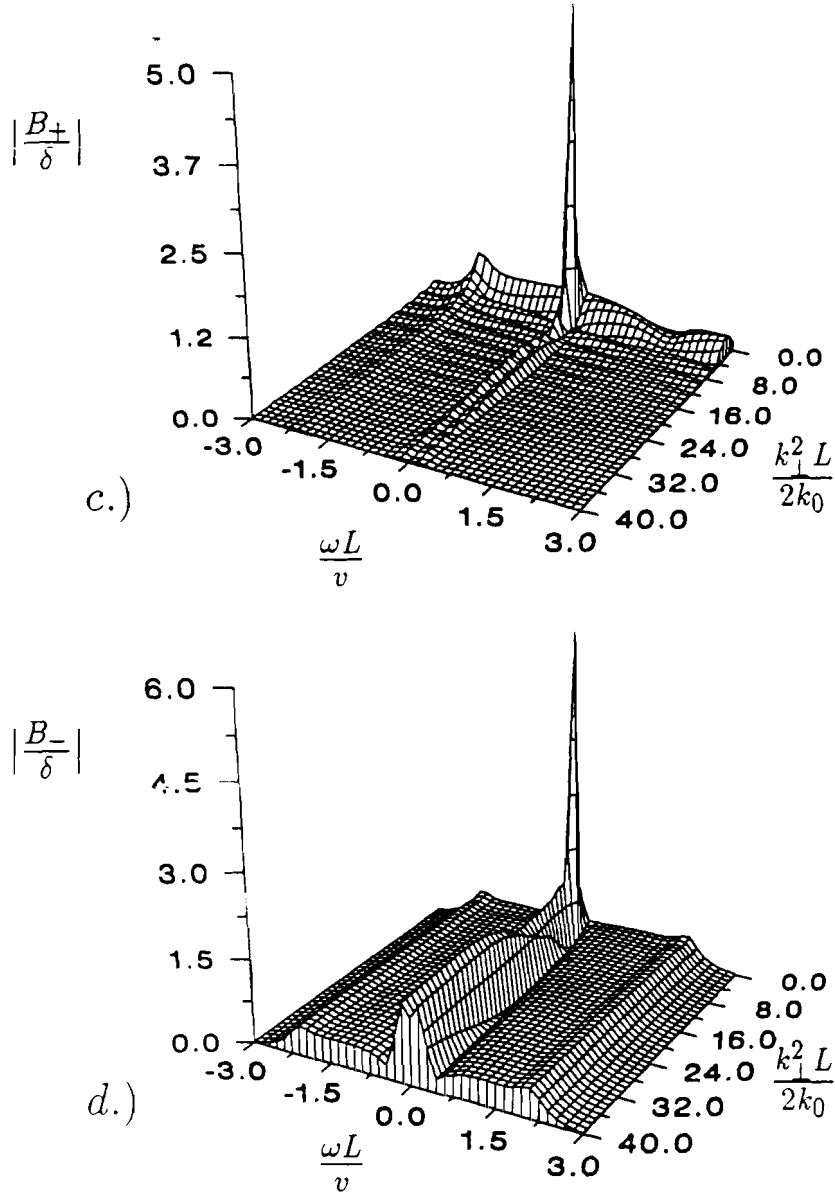


Figure 5.1: (continued) Linear convective gain spectrum of the resonant four-sideband interaction is plotted in the plane of the real part of the perturbation frequency, $\text{Re}(\omega L/v)$, and the transverse perturbation wavenumber parameter, where $|B_0|^2 = |F_0|^2$, $c_s/c = 0.001$, $k_0 L = 1000$, $\nu_{ia}/\Omega_{ia} = 0.2$, and $\alpha|F_0|^2 L/v = 0.43$, which is 0.95 of the minimal absolute threshold intensity for cooperative filamentation. The spectra for the Bragg scattering (c.) and the phase conjugate (d.) sideband are plotted here. The resonances in Γ_\perp and Γ_\parallel have the frequencies $\text{Re}(\omega L/v) = c_s k_\perp k_0/v \approx 0.17$ and $\text{Re}(\omega L/v) = 2k_0 L c_s/v \approx 2.0$, respectively.

instabilities [55, 93]. The largest convective gain in Figs. 5.1, located near $\text{Re}(\omega L/v) = 0$ and $k_{\perp}^2 L/2k_0 = 3.1$ for each sideband, is due to cooperative filamentation [55]. Peaks in the convective gain spectrum such as this indicate that the scattered light will have important transverse structure. At larger values of k_{\perp}^2 these three two-sideband processes may overlap interacting through the Γ_{\perp} grating. Backward SBS is detuned as ω deviates from the ion-acoustic frequency since the ion wave is no longer driven resonantly. In matrix N , $(\Gamma_{\parallel} - 1) \rightarrow 0$ when $\omega \rightarrow 0$ at fixed k_{\perp} implying that none of the gain near $\omega = 0$ is due to backward SBS. Backward SBS shares the Γ_{\parallel} resonance with the two phase conjugation interactions. Their spectral overlap is clearly illustrated in Fig. 5.1(d) at $k_{\perp}^2 = 0$ and the Γ_{\parallel} resonance. Recall that the pure phase conjugation interaction is independent of k_{\perp} and the backward SBS interaction is largest for $k_{\perp} = 0$. This convective gain analysis suggests that cooperative instability growth rates can exceed single-wave instability growth rates by a significant margin and that transverse effects can be important.

While single-pump backward SBS is known to become absolutely unstable when the pump intensity is above $(\alpha|F_0|^2 L/v)_{SBS} = \nu_{ia}^2 L/4v\omega_0(c_s/c)^2$ [3], the counterpropagating pump wave introduces several cooperative absolute instabilities which may have thresholds below those for the single-pump convective or absolute instabilities. Intensity thresholds for cooperative absolute instabilities predicted by Eqs. (5.3) – (5.9) are plotted in Figs. 5.2 and 5.3 for two values of the ion damping rate, $\nu_{ia}/\Omega_{ia} = 0.2$ and 0.05 , respectively, and $|F_0|^2 = |B_0|^2$. In the upper graphs of Figs. 5.2 and 5.3, the threshold intensity is measured in units of the single pass convective gain of the filamentation instability of the forward pump. The threshold intensity corresponding to $\alpha|F_0|^2 L/v = 1$ is $I[\text{Wcm}^{-2}] \sim \{4.42 \times 10^{13} T_{\text{eV}} [1 - (n_0/n_c)] / k_0 L \lambda_{\mu}^2 (n_0/n_c)\}$ where n_0/n_c is the

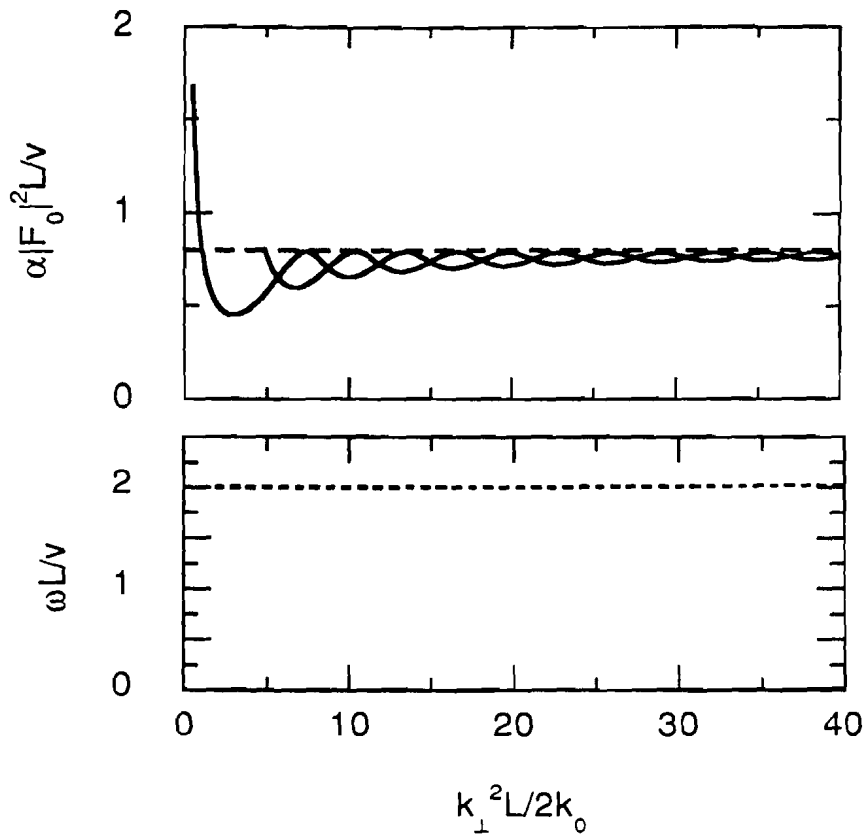


Figure 5.2: In the upper graph the lowest resonant (---) and non-resonant (—) absolute instability thresholds are plotted for the resonant four-sideband system. In the lower graph the frequency shifts corresponding to these thresholds are plotted. Both graphs are plotted as a function of the transverse perturbation wavenumber parameter, where $|B_0|^2 = |F_0|^2$, $c_s/c = 0.001$, $k_0 L = 1000$, and $\nu_{ia}/\Omega_{ia} = 0.2$. The frequency shift corresponding to the Γ_{\parallel} resonance is $\text{Re}(\omega L/v) = 2c_s k_0 L/v \approx 2.0$ and to the nonresonant mode is $\text{Re}(\omega L/v) = 0$.

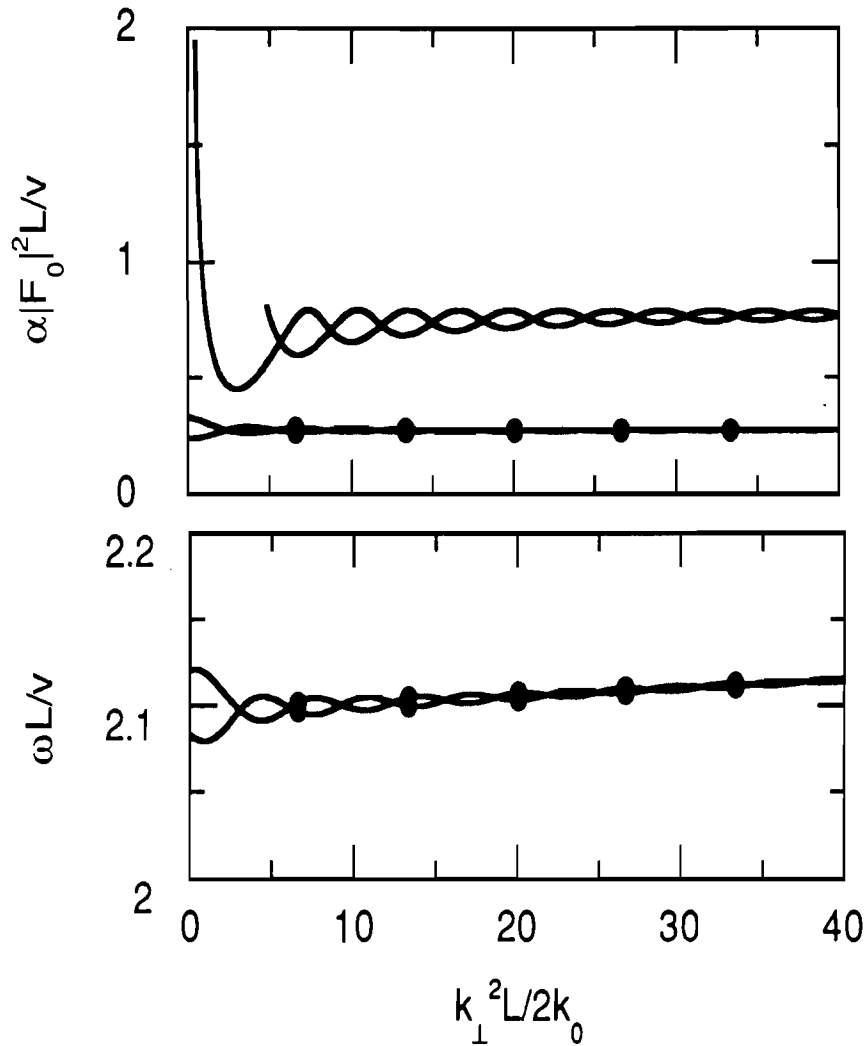


Figure 5.3: In the upper graph the resonant (•••) and non-resonant (—) absolute instability thresholds are plotted for the resonant four-sideband system. In the lower graph the frequency shifts corresponding to these thresholds are plotted. Both graphs are plotted as a function of the transverse perturbation wavenumber parameter, where $|B_0|^2 = |F_0|^2$, $c_s/c = 0.001$, $k_0 L = 1000$, and $\nu_{ia}/\Omega_{ia} = 0.05$. The frequency shift corresponding to the $\Gamma_{||}$ resonance is $\text{Re}(\omega L/v) = 2c_s k_0 L/v \approx 2.1$ and to the nonresonant mode is $\text{Re}(\omega L/v) = 0$.

number density of the plasma divided by its critical value. For $c_s/c = 0.001$, $k_0 L = 1000$, $n_0/n_c = 0.25$ and $\lambda_\mu = 1.06\mu$, $L = 170\mu$, and $T = 940\text{eV}$, so $I = 1.1 \times 10^{14}\text{Wcm}^{-2}$. For these parameters $(\alpha|F_0|^2 L/v)_{SBS} = 20.0$ and 1.25 for $\nu_{ia}/\Omega_{ia} = 0.2$ and 0.05 respectively. The real part of the perturbation frequency at these thresholds, $\pm\text{Re}(\omega L/v)$ is plotted in the lower graphs of Figs. 5.2 and 5.3, where $\text{Im}(\omega L/v) = 0$. The ion-acoustic frequency of the short wavelength grating is $\Omega_{ia} L/v \simeq 2k_0 L(c_s/c) = 2$.

The dashed curves in Fig. 5.2 correspond to the minimal resonant absolute intensity thresholds for $\gamma_{ia}/\Omega_{ia} = 0.2$. The lowest nonresonant threshold is plotted as a solid line and has $\omega L/v = 0$. The minimal intensity threshold occurs on the nonresonant branch at $\alpha|F_0|^2 L/v = 0.45$ for $k_\perp^2 L/2k_0 = 3.1$ and is due to cooperative filamentation. In the linear regime light scattered by this cooperative filamentation instability has frequency ω_0 and forms a hollow cone with $\theta_c = \sqrt{6.2/k_0 L}$. This and other signatures of cooperative filamentation have been observed in atomic gas experiments [47]. In the large- k_\perp limit the nonresonant phase conjugation threshold is recovered where $\alpha|F_0|^2 L/v$ scales as $\pi|F_0|/4|B_0|$, and $\text{Re}(\omega L/v) \propto \alpha(|B_0|^2 - |F_0|^2)$. These results show that the cooperative filamentation instability can be important even when cooperative resonant absolute instabilities occur.

The curves labeled with dots in Fig. 5.3 correspond to the resonant absolute instabilities having the lowest intensity thresholds when $\gamma_{ia}/\Omega_{ia} = 0.05$. Their frequency shift corresponds to that of the Γ_{\parallel} grating. The solid curves correspond to the nonresonant branch as in Fig. 5.2. The resonantly unstable modes have finite frequency shifts of the order of the acoustic wave frequency of the Γ_{\parallel} grating. Neither sign of the acoustic frequency shift in either figure is favored since the Stokes and anti-Stokes sidebands are free to switch roles as $\omega \rightarrow \omega^*$ and the

system is invariant to rotations about the pump axis. While the resonant absolute instability thresholds approach the phase conjugate threshold at large k_{\perp} , they have a hybrid character near $k_{\perp} = 0$ [93]. The cooperative absolute instability intensity thresholds can be much lower than single-pump thresholds, as stated previously.

The minimum values of the absolute instability thresholds and some of their phase conjugate limits are plotted as a function of $\ln(|B_0/F_0|^2)$ in Fig. 5.4 following the labeling convention of Figs. 5.2 and 5.3. In the limit $|B_0/F_0|^2 \rightarrow 1$ the minimum thresholds found in Figs. 5.2 and 5.3 are recovered. At $|B_0/F_0|^2 = 1$ the lowest three threshold curves are due to the resonant modes at $\gamma_{ia}/\Omega_{ia} = 0.05$ where $\alpha|F_0|^2 L/v = 0.24, 0.28, 0.33$ for $k_{\perp}^2 L/2k_0 = 0.0, 20.0, 0.0$, respectively. The non-resonant thresholds are $\alpha|F_0|^2 L/v = 0.45, 0.72, 0.79$ for $k_{\perp}^2 L/2k_0 = 3.1, 20.0, 20.0$ and the resonant threshold for $\gamma_{ia}/\Omega_{ia} = 0.20$ is $\alpha|F_0|^2 L/v = 0.80$ at $k_{\perp}^2 L/2k_0 = 0.0$. Note that the cooperative TMI threshold given by the $\alpha|F_0|^2 L/v = 0.45$, $k_{\perp}^2 L/2k_0 = 3.1$ curve remains degenerate with $\omega = 0$ and is below the degenerate phase conjugation threshold over the entire range of r^2 shown. The phase conjugation thresholds for the $\alpha|F_0|^2 L/v = 0.72, 0.79$, $k_{\perp}^2 L/2k_0 = 20.0$ are allowed to become nondegenerate as shown by the small frequency shift they acquire as r is decreased. Near $r = 1$, this frequency is in qualitative agreement with the expected frequency shift of the phase conjugate signal, $(|F_0|^2 - |B_0|^2)/2$, stated in Chapter 4. However, as $|B_0|^2$ approaches zero the graph shows a shift having a smaller limiting value than expected from the degenerate phase conjugation instability. Notice that the limiting value of this frequency shift is $\omega_r = 0.2$ which is the value that is expected for the resonant k_{\perp} grating. In addition, these two thresholds have the same r^2 dependence as that of the resonant large- k grating as r becomes small. Both of these facts suggest that the resonant and nonresonant

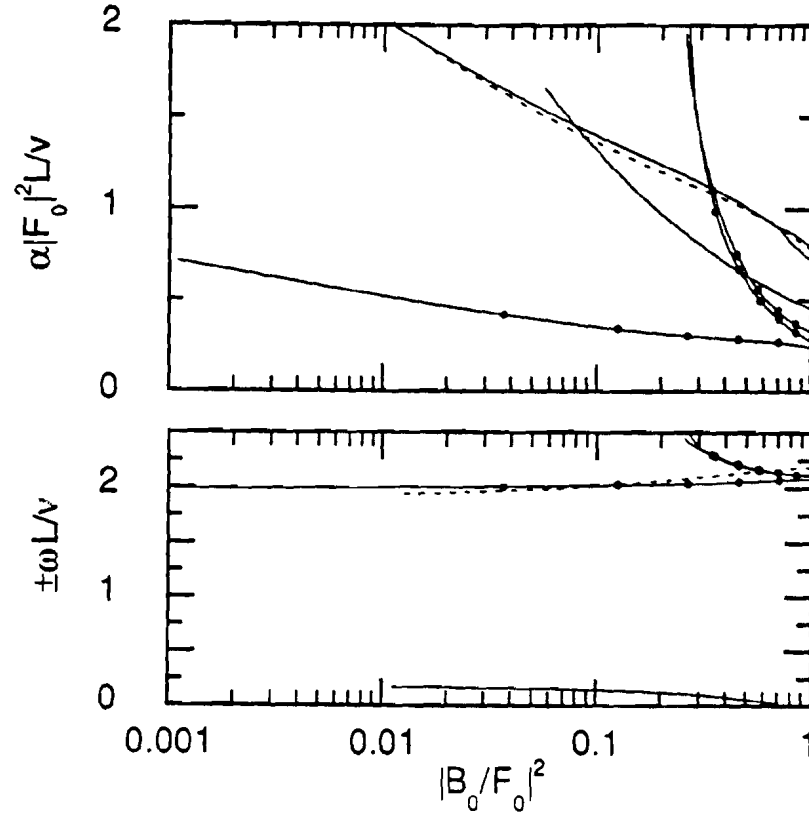


Figure 5.4: The variation of the minimal absolute intensity thresholds and their associated frequency shifts are plotted for several modes of the resonant four-sideband system as a function of the pump intensity ratio, where $c_s/c = 0.001$, $k_0L = 1000$. The solid curves (—) arise due to nonresonant modes at $r^2 = 1.0$. The dashed curves (---) arise due to resonant modes with $\nu_{ia}/\Omega_{ia} = 0.2$, while the dotted curves (•••) arise due to modes with $\nu_{ia}/\Omega_{ia} = 0.05$. The resonance for Γ_{\perp} is $\text{Re}(\omega L/v) = k_{\perp}Lc_s/v \approx 0.17$ and for Γ_{\parallel} is $\text{Re}(\omega L/v) = 2k_0Lc_s/v \approx 2.0$. See text for the values of $k_{\perp}^2L/2k_0$ associated with each mode.

branches overlap and that these two degenerate thresholds take on a resonant instability character as r is decreased, forming still another hybrid cooperative instability. Observations consistent with the $k_{\perp}^2 L/2k_0 = 0.0$ results are described in [36]. The cooperative absolute instability thresholds are lower than the single-wave or phase conjugate thresholds even when the pump intensity ratio is small.

This work can be extended to treat the three dimensional instabilities of counterpropagating waves [74], the effects of inhomogeneity of the plasma, the motion of the plasma and the motion of the critical surface. A mode which is reflected from the critical surface and is Doppler-shifted with respect to the pump has been shown to enhance the backward SBS signal [63 – 65]. The analysis presented here may be extended to include this effect by retaining the pump depletion terms and allowing a frequency difference between the pumps of the order of the sound frequency.

In summary, cooperative instabilities can have larger convective gains and lower absolute instability thresholds than single-wave instabilities when two counterpropagating electromagnetic waves interact via ponderomotively driven ion-acoustic waves in a finite homogeneous plasma. The intensity thresholds of cooperative absolute instabilities increase slowly as a function of the ratio of the pump intensities. The presence of the counterpropagating light wave introduces both cooperative filamentation and cooperative Brillouin-enhanced FWM instabilities, both of which can be attributed to the combined effect of one- and two-sideband instabilities. Because some cooperative instabilities scatter light at a finite angle to the pump axis, they cannot be adequately modeled in one dimension.

Chapter 6

Discussion

In this thesis, it has been shown that a family of hybrid cooperative instabilities exist in counterpropagating-wave systems and a description of their character and mechanism has been given. A thorough investigation of the cooperative transverse modulational instability (TMI) in cubically nonlinear media has been carried out showing its stability properties and its basic relation to the constituent four-wave mixing (FWM) interactions. The extension of the stability analysis to Brillouin-active media suggests that the cooperative TMI continues to be important and that other new and interesting hybrid and cooperative instabilities also arise.

These results are of interest in both the field of laser-plasma interactions and in the more general context of nonlinear optics. Realizations of FWM and phase conjugation in laser-plasma interaction experiments are likely to show the effects of cooperative instabilities. Unfortunately, no published work dealing with these issues has appeared. Laser-produced plasma experiments have been performed to investigate scattered light with frequency near that of the pump [68, 69, 94, 95]. These studies have provided data which is consistent with the idea that back-reflected light can enhance filamentation [69] and backward stimulated Brillouin scattering (SBS) [94, 95].

The theory presented in this thesis predicts thresholds which are at the level

of current experiments. For example, direct observations of ponderomotive filamentation in laser-driven plasmas have been made recently by Young *et al.* [68]. In these experiments, a single laser pulse was passed through a preformed underdense plasma and the transverse intensity profile of the laser was intentionally modulated to produce a striated intensity distribution of known periodicity. These initial modulations in the incident laser intensity were rather large. Consequently, Young *et al.* argued that the laser filaments could be observed with only a single exponentiation in laser intensity. On this basis, the convective threshold intensity for the single pump was predicted to be approximately $5 \times 10^{13} \text{ Wcm}^{-2}$. The observed threshold intensity was approximately $3 \times 10^{13} \text{ Wcm}^{-2}$. Thus, filamentation has been observed at the intensities predicted by the single-wave analysis.

Suppose now that one was to redo the experiment of Young *et al.* with two counterpropagating laser beams rather than a single laser beam. With laser beams of equal intensity in a finite plasma typical of this experiment, the predicted threshold intensity of the absolute filamentation instability is approximately $4.5 \times 10^{13} \text{ Wcm}^{-2}$. With a backward-to-forward intensity ratio of 5%, the predicted threshold intensity of the forward laser beam is approximately $1.8 \times 10^{14} \text{ Wcm}^{-2}$. Since typical laser intensities are in the range of $10^{13} - 10^{15} \text{ Wcm}^{-2}$, it should be possible to observe the absolute filamentation instability in current plasma-physics experiments. It might also be possible to observe the absolute filamentation instability with a single laser beam if back-scattered radiation from the density maximum of the plasma is sufficiently intense.

The preceding analysis shows that it is possible for the cooperative filamentation instability to occur in current inertial-confinement fusion experiments. What is more, this work suggests that cooperative resonant instabilities may also be important and may lead to transverse structure resulting from resonant instabilities.

A definitive conclusion on the likelihood of such occurrences must await a more detailed theory which takes absorption and plasma inhomogeneities into account.

In the field of nonlinear optics both experimental and computational work exists which supports this analysis. Conical light emission, which is a far-field signature of the TMI, has been observed in several recent experiments on phase conjugation in sodium vapor [91, 47, 49, 52]. In these experiments, the range of incident laser wavelengths encompassed regimes in which sodium vapor is both a self-focusing ($\sigma = 1$) and a self-defocusing ($\sigma = -1$) medium, and the incident laser intensities were approximately equal. Conical emission near the critical angle corresponding to the most unstable linearly growing mode was observed to occur spontaneously whenever the incident intensities exceeded certain threshold values.

In the experiments of Grynberg *et al.* [47], no conical emission was observed during single-wave illumination of the sodium vapor. When the sodium vapor was illuminated with two light waves, bidirectional conical emission was observed in the self-focusing regime.

In most of the experiments of Pender and Hesselink [49, 52] no conical emission was observed during single-wave illumination of the sodium vapor. However, in one set of single-wave experiments in the self-focusing regime [49], they did observe unidirectional conical emission. This observation is consistent with the hypothesis that noise-level radiation is amplified convectively and can be detected when the incident intensities exceed a certain value. When the sodium vapor was illuminated with two light waves, bidirectional conical emission was observed in both the self-focusing and self-defocusing regimes. Unfortunately, however, no information on either the relative intensity thresholds in these two regimes, or how the observed conical-emission thresholds compared to the theoretical phase-conjugate oscillation thresholds, was given.

Both sets of experiments were completed before the properties of the cooperative TMI and its relation to the two-sideband processes were well understood. However, the importance of the cooperative TMI has now been realized and work is now being carried out in which the full system of partial differential equations is integrated numerically and the analysis is being extended into the nonlinear regime [96]. A new set of experiments using simple nonlinear optical media might now be carried out to confirm the predictions of these theoretical works.

It should be of particular interest to continue the work discussed here. In the field of laser-plasma interactions further understanding of cooperative instabilities could have important implications both for the understanding of FWM and phase conjugation and for the understanding of indirect absorption of laser light in applications of laser-plasma interactions. The ideas presented here are directly applicable and of central importance to the understanding of transverse effects in both cubic and Brillouin-active media.

References

- [1] J. F. Drake, P. K. Kaw, Y. C. Lee, G. Schmidt, C. S. Liu and M. N. Rosenbluth, "Parametric Instabilities of Electromagnetic Waves in Plasmas," *Phys. Fluids* **17**, 778 – 785 (1974).
- [2] *Advances in Plasma Physics*, Vol. 6, A. Simon and W. Thompson, eds. (Wiley, New York, 1976).
- [3] B. I. Cohen and C. E. Max, "Stimulated Scattering of Light by Ion Modes in a Homogeneous Plasma: Space-Time Evolution," *Phys. Fluids* **22**, 1115 – 1132 (1979).
- [4] W. L. Kruer, *The Physics of Laser Plasma Interactions* (Addison-Wesley, Redwood City, California, 1988).
- [5] Y. R. Shen and N. Bloembergen, "Theory of Stimulated Brillouin and Raman Scattering," *Phys. Rev. A* **137**, 1787 – 1805 (1965).
- [6] N. Bloembergen, *Nonlinear Optics* (Benjamin, New York, 1965).
- [7] W. Kaiser and M. Maier, "Stimulated Rayleigh, Brillouin and Raman Spectroscopy," in *Laser Handbook*, F. T. Arecchi and E. O. Schulz-Dubois, eds. (North-Holland, Amsterdam, 1972), pp. 1077 – 1150.
- [8] Y. R. Shen, *The Principles of Nonlinear Optics* (Wiley, New York, 1984).

- [9] R. A. Fisher, ed., *Optical Phase Conjugation* (Academic Press, New York, 1983).
- [10] B. Ya. Zel'dovich, N. F. Pilipetsky, V. V. Shkunov, *Principles of Phase Conjugation* (Springer-Verlag, New York, 1985).
- [11] A. L. Berkhoer and V. E. Zakharov, "Self Excitation of Waves with Different Polarizations in Nonlinear Media," *Sov. Phys. JETP* **31**, 486 – 490 (1970).
- [12] K. P. Das and S. Sihi, "Modulational Instability of Two Transverse Waves in a Cold Plasma," *J. Plasma Phys.* **21**, 183 – 191 (1979).
- [13] C. R. Menyuk, "Nonlinear Pulse Propagation in Birefringent Optical Fibers," *IEEE J. Quantum Electron.* **QE-23**, 174 – 176 (1987).
- [14] Y. Inoue, "Nonlinear Interaction of Dispersive Waves With Equal Group Velocity," *J. Phys. Soc. Japan* **43**, 243 – 249 (1977).
- [15] B. K. Som, M. R. Gupta and B. Dasgupta, "Coupled Nonlinear Schroedinger Equation for Langmuir and Dispersive Ion Acoustic Waves," *Phys. Lett. A* **72**, 111 – 114 (1979).
- [16] A. G. Litvak and G. M. Fraiman, "Interactions of Beams of Oppositely Traveling Electromagnetic Waves in a Transparent Nonlinear Medium," *Radiophys. Quantum Electron.* **15**, 1024 – 1029 (1972).
- [17] M. R. Gupta, B. K. Som and B. Dasgupta, "Coupled Nonlinear Schroedinger Equations for Langmuir and Electromagnetic Waves and Extension of their Modulational Instability Domain," *J. Plasma Phys.* **25**, 499 – 507 (1981).
- [18] G. P. Agrawal, "Modulational Instability Induced by Cross-Phase Modulation," *Phys. Rev. Lett.* **59**, 880 – 883 (1987).

- [19] B. Ghosh and K. P. Das, "Nonlinear Interactions of Two Compressional Hydromagnetic Waves," *J. Plasma Physics* **39**, 215 – 228 (1988).
- [20] C. J. McKinstrie and R. Bingham, "The Modulational Instability of Coupled Waves," *Phys. Fluids B* **1**, 230 – 237 (1989); **2**, 3215 (1990).
- [21] C. J. McKinstrie and G. G. Luther, "The Modulational Instability of Co-linear Waves," *Physica Scripta* **T-30**, 31 – 40 (1990).
- [22] R. J. Briggs, *Electron-Stream Interaction with Plasmas* (Massachusetts Institute of Technology Press, Cambridge, Massachusetts, 1964), pp. 8 – 46.
- [23] A. Bers, "Space-Time Evolution of Plasma Instabilities — Absolute and Convective," in *Handbook of Plasma Physics* M. N. Rosenbluth and R. Z. Sagdeev, eds. *Vol. I – Basic Plasma Physics*, A. A. Galeev and R. N. Sudan, eds. (North-Holland, New York, 1983), pp. 451 – 517.
- [24] P. Huerre, "Spatio-Temporal Instabilities in Closed and Open Flows," in *Instabilities and Nonequilibrium Structures*, E. Tirapegui and D. Villarroel, eds. (D. Reidel Publishing Company, New York, 1987), pp. 141 – 177.
- [25] S. Wabnitz, "Modulational Polarization Instability of Light in a Nonlinear Birefringent Dispersive Medium," *Phys. Rev. A* **38**, 2018 – 2021 (1988).
- [26] G. P. Agrawal, P. L. Baldeck and R. R. Alfano, "Modulation Instability Induced by Cross-Phase Modulation in Optical Fibers," *Phys. Rev. A* **39**, 3406 – 3413 (1989).
- [27] S. Trillo, S. Wabnitz, G. I. Stegeman and E. M. Wright, "Parametric Amplification and Modulational Instabilities in Dispersive Nonlinear Directional

- Couplers with Relaxing Nonlinearity," *J. Opt. Soc. Am. B* **6**, 889 – 900 (1989).
- [28] G. P. Agrawal, *Nonlinear Fiber Optics* (Academic Press, Boston, 1989).
- [29] C. T. Law and A. E. Kaplan, "Dispersion-Related Multimode Instabilities and Self-Sustained Oscillations in Nonlinear Counterpropagating Waves," *Opt. Lett.* **14**, 734 – 736 (1989).
- [30] C. T. Law and A. E. Kaplan, "Instabilities and Amplification of Counterpropagating Waves in a Kerr Nonlinear Medium," *J. Opt. Soc. Am. B* **8**, 58 – 67 (1991).
- [31] Y. Silberberg and I. Bar-Joseph, "Instabilities, Self-Oscillation and Chaos in a Simple Nonlinear Optical Interaction," *Phys. Rev. Lett.* **48**, 1541 – 1543 (1982).
- [32] Y. Silberberg and I. Bar-Joseph, "Optical Instabilities in a Nonlinear Kerr Medium," *J. Opt. Soc. Am. B* **1**, 662 – 670 (1984).
- [33] A. L. Gaeta, R. W. Boyd, J. R. Ackerhalt and P. W. Milonni, "Instabilities and Chaos in the Polarization of Counterpropagating Light Fields," *Phys. Rev. Lett.* **58**, 2432 – 2435 (1987).
- [34] D. J. Gauthier, M. S. Malcuit and R. W. Boyd, "Polarization Instabilities of Counterpropagating Laser Beams in Sodium Vapor," *Phys. Rev. Lett.* **61**, 1827 – 1830 (1988).
- [35] P. Narum, A. L. Gaeta, M. D. Skeldon and R. W. Boyd, "Instabilities of Laser Beams Counterpropagating through a Brillouin-Active Medium," *J. Opt. Soc. Am. B* **5**, 623 – 628 (1988).

- [36] A. L. Gaeta, M. D. Skeldon, R. W. Boyd and P. Narum, "Observation of Instabilities of Laser Beams Counterpropagating through a Brillouin Medium," *J. Opt. Soc. Am. B* **6**, 1709 – 1713 (1989).
- [37] M. V. Goldman and E. A. Williams, "Time-Dependent Phase Conjugation and Four-Wave Mixing in Plasmas," *Phys. Fluids B* **3**, 751 – 765 (1991) and references therein.
- [38] M. V. Goldman, "Time-Dependent Phase Conjugation in Plasmas: Numerical Results and Interpretation," *Phys. Fluids B* **3**, 2161 – 2169 (1991) and references therein.
- [39] B. Ya. Zel'dovich and V. V. Shkunov, "Characteristics of Stimulated Scattering in Opposite Pump Beams," *Sov. J. Quantum Electron.* **12**, 223 – 225 (1982).
- [40] N. F. Andreev, V. I. Bespalov, A. M. Kiselev, G. A. Pasmanik and A. A. Shilov, "Raman Interaction in the Field of Opposing Light Waves," *Sov. Phys. JETP* **55**, 612 – 617 (1982).
- [41] V. I. Bespalov, E. L. Bubis, S. N. Kulagina, V. G. Manishin, A. Z. Matveev, G. A. Pasmanik, P. S. Razenshtein and A. A. Shilov, "Stimulated Brillouin Scattering in a Field of Opposite Light Waves," *Sov. J. Quantum Electron.* **12**, 1544 – 1547 (1982).
- [42] A. M. Scott and K. D. Ridley, "A Review of Brillouin-Enhanced Four-Wave Mixing," *IEEE J. Quantum Electron.* **QE-25**, 438 – 459 (1989) and references therein.

- [43] F. W. Perkins and E. J. Valeo, "Thermal Self-Focusing of Electromagnetic Waves in Plasmas," *Phys. Rev. Lett.* **32**, 1234 – 1237 (1974).
- [44] S. N. Vlasov and V. I. Talanov, "About Some Features of Scattering of Signal Wave on Counterpropagating Pump Beams Under Conditions of Degenerate Four-Photon Interaction," in *Optical Phase Conjugation in Nonlinear Media*, V. I. Bespalov, ed. (USSR Academy of Science, Gorkii, 1979), pp. 85 – 91; a convenient account of this work is to be found on pp. 165 – 167 of Ref. [10].
- [45] S. N. Vlasov and E. V. Sheinina, "Theory of the Interaction of Waves Traveling in Opposite Directions in a Nonlinear Cubic Medium," *Radiophys. Quantum Electron.* **26**, 15 – 22 (1983).
- [46] W. J. Firth and C. Paré, "Transverse Modulational Instabilities for Counterpropagating Beams in Kerr Media," *Opt. Lett.* **13**, 1096 – 1098 (1988).
- [47] G. Grynberg, E. Le Bihan, P. Verkerk, P. Simoneau, J. R. R. Leite, D. Bloch, S. Le Boiteux and M. Ducloy, "Observation of Instabilities Due to Mirrorless Four-Wave Mixing Oscillation in Sodium," *Opt. Commun.* **67**, 363 – 366 (1988).
- [48] G. Grynberg and J. Paye, "Spatial Instability for a Standing Wave in a Nonlinear Medium," *Europhys. Lett.* **8**, 29 – 33 (1989).
- [49] J. Pender and L. Hesselink, "Conical Emissions and Phase Conjugation in Atomic Sodium Vapor," *IEEE J. Quantum Electron.* **QE-25**, 395 – 402 (1989).
- [50] W. J. Firth, A. Fitzgerald and C. Paré, "Transverse Instabilities Due to

- Counterpropagation in Kerr Media," *J. Opt. Soc. Am. B* **7**, 1087 - 1097 (1990).
- [51] G. G. Luther and C. J. McKinstrie, "Transverse Modulational Instability of Collinear Waves," *J. Opt. Soc. Am. B* **7**, 1125 - 1141 (1990).
- [52] J. Pender and L. Hesselink, "Degenerate Conical Emissions in Atomic-Sodium Vapor," *J. Opt. Soc. Am. B* **7**, 1361 - 1373 (1990).
- [53] W. J. Firth and C. Penman, "Counterpropagation in Kerr Media: Combined Diffractive-Dispersive Instabilities," OSA Proceedings on Nonlinear Dynamics in Optical Systems, Vol. 7, Neal B. Abraham, Elsa M. Garmire, Paul Mandel, eds. (Opt. Soc. Am., Washington, DC 1991), pp. 142 - 145.
- [54] G. G. Luther, C. J. McKinstrie and A. L. Gaeta, "The Transverse Modulational Instability of Counterpropagating Light Waves," OSA Proceedings on Nonlinear Dynamics in Optical Systems, Vol. 7, Neal B. Abraham, Elsa M. Garmire, Paul Mandel, eds. (Opt. Soc. Am., Washington, DC 1991), pp. 205 - 209.
- [55] G. G. Luther and C. J. McKinstrie, "The Transverse Modulational Instability of Counterpropagating Light Waves," to be published in *J. Opt. Soc. Am. B*.
- [56] G. P. Agrawal, "Transverse Modulation Instability of Copropagating Optical Beams in Nonlinear Kerr Media," *J. Opt. Soc. Am. B* **7**, 1072 - 1078 (1990).
- [57] C. J. McKinstrie and D. A. Russell, "Nonlinear Focusing of Coupled Waves," *Phys. Rev. Lett.* **61**, 2929 - 2933 (1988).

- [58] G. P. Agrawal, "Induced Focusing of Optical Beams in Self-Defocusing Non-linear Media," *Phys. Rev. Lett.* **64**, 2487 – 2490 (1990).
- [59] N. B. Abraham and W. J. Firth, "Overview of Transverse Effects in Nonlinear-Optical Systems," *J. Opt. Soc. Am. B* **7**, 951 – 962 (1990).
- [60] C. E. Max, "Physics of the Coronal Plasma in Laser Fusion Targets," in *Interaction Laser-Matière*, R. Balian and J. C. Adam, eds. (North-Holland, Amsterdam, 1982), pp. 301 – 410.
- [61] R. L. McCrory and J. M. Soures, "Inertially Confined Fusion," *Laser-Induced Plasmas and Applications*, L. J. Radziemski and D. A. Cremers, eds. (Dekker, New York, 1989), Chapter 5.
- [62] R. S. Craxton, R. L. McCrory and J. M. Soures, "Progress in Laser Fusion," *Sci. Am.* **255**, 68 – 79 (1986).
- [63] I. M. Begg and R. A. Cairns, "Enhanced Reflection of Laser Light from an Expanding Plasma," *J. Phys. D (Appl. Phys.)* **9**, 2341 – 2348 (1976).
- [64] C. J. Randall, J. J. Thomson and K. G. Estabrook, "Enhancement of Stimulated Brillouin Scattering Due to Reflection of Light from Plasma Critical Surface," *Phys. Rev. Lett.* **43**, 924 – 927 (1979).
- [65] C. J. Randall, J. R. Albritton and J. J. Thompson, "Theory and Simulation of Stimulated Brillouin Scatter Excited by Non-Absorbed Light in Laser Fusion Systems," *Phys. Fluids* **24**, 1474 – 1484 (1981).
- [66] R. H. Lehmberg, "Theory of Optical Ray Tracing in Laser-Plasma Backscatter," *Phys. Rev. Lett.* **41**, 863 – 866 (1978).

- [67] S. M. Cameron, M. D. Tracy, J. S. DeGroot, K. Estabrook, and E. A. Williams, *Bull. Am. Phys. Soc.* **36**, 2352 (1991)
- [68] P. E. Young, H. A. Baldis, R. P. Drake, E. M. Campbell and K. G. Estabrook, "Direct Evidence of Ponderomotive Filamentation in a Laser-Produced Plasma," *Phys. Rev. Lett.* **61**, 2336 – 2339 (1988).
- [69] P. E. Young, "Experimental Study of Filamentation in Laser-Plasma Interactions," *Phys. Fluids B* **3**, 2331 – 2336 (1991).
- [70] B. R. Suydam, "Self-Focusing of Very Powerful Laser Beams," in *Laser Induced Damage in Optical Materials: 1973*, A. J. Glass and A. H. Guenther, eds. (National Bureau of Standards Special Publication 387, 1973), pp. 42 – 48.
- [71] L. S. Hall and W. Heckrotte, "Instabilities: Convective versus Absolute," *Phys. Rev.* **166**, 120 – 128 (1968).
- [72] A. Bers, A. K. Ram and G. Francis, "Relativistic Analysis of Absolute and Convective Instability Evolutions in Three Dimensions," *Phys. Rev. Lett.* **53**, 1457 – 1460 (1984).
- [73] O. L. Antipov, V. I. Bespalov and G. A. Pasmanik, "New Possibilities of Generation of Pump-Conjugate Beams by Stimulated Scattering of Opposed Light Waves," *Sov. Phys. JETP* **63**, 926 – 932 (1986).
- [74] C. J. McKinstrie and M. V. Goldman, "Three-Dimensional Instabilities of Counterpropagating Light Waves in Homogeneous Plasma," to be published in *J. Opt. Soc. Am. B*.

- [75] R. Y. Chiao, P. L. Kelley and E. Garmire, "Stimulated Four-Photon Interaction and its Influence on Stimulated Rayleigh-Wing Scattering," *Phys. Rev. Lett.* **17**, 1158 - 1161 (1966).
- [76] G. Askar'yan, "Effects of the Gradient of a Strong Electromagnetic Beam on Electrons and Ions," *Sov. Phys. JETP* **15**, 1088 - 1090 (1962).
- [77] R. Y. Chiao, E. Garmire and C. H. Townes, "Self-Trapping of Optical Beams," *Phys. Rev. Lett.* **15**, 479 - 482 (1964).
- [78] V. I. Bespalov and V. I. Talanov, "Filamentary Structure of Light Beams in Nonlinear Liquids," *Sov. Phys. JETP Lett.* **3**, 307 - 310 (1966).
- [79] A. J. Palmer, "Stimulated Scattering and Self-Focusing in Laser-Produced Plasmas," *Phys. Fluids* **14**, 2714 - 2718 (1971).
- [80] P. K. Kaw, G. Schmidt, T. Wilcox, "Filamentation and Trapping of Electromagnetic Radiation in Plasmas," *Phys. Fluids* **16**, 1522 - 1525 (1973).
- [81] C. E. Max, J. Arons and A. B. Langdon, "Self-Modulation and Self-Focusing of Electromagnetic Waves in Plasmas," *Phys. Rev Lett.* **33**, 209 - 212 (1974).
- [82] M. S. Sodha, A. K. Ghatak and V. K. Tripathi, "Self Focusing of Laser Beams in Plasmas and Semiconductors," *Progress in Optics, Vol. 3*, E. Wolf, ed. (North-Holland, Amsterdam, 1976), pp. 169 - 265.
- [83] W. L. Kruer , "Ponderomotive and Thermal Filamentation of Laser Light," *Comments Plasma Phys. Controlled Fusion* **9**, 63 - 72 (1985).
- [84] A. Yariv, *Quantum Electronics* (Wiley, New York, 1967), pp. 327 - 338.

- [85] C. J. McKinstrie and A. Simon, "Nonlinear Saturation of the Absolute Stimulated Raman Scattering Instability in a Finite Collisional Plasma," *Phys. Fluids* **29**, 1959 – 1970 (1986).
- [86] W. H. Press, B. P. Flannery, S. A. Teukolsky and W. T. Vetterling, *Numerical Recipes: The Art of Scientific Computing* (New York: Cambridge University Press, 1986).
- [87] A. L. Gaeta, The Institute of Optics, University of Rochester, Rochester, New York 14627 (private communication, 1991).
- [88] A. L. Gaeta, The Institute of Optics, University of Rochester. Rochester. New York 14627 (private communication, 1989).
- [89] G. G. Luther, C. J. McKinstrie and R. W. Short, Poster 1P31, 16th IEEE International Conference on Plasma Science, Buffalo, New York, May 22 – 24, 1989.
- [90] E. M. Epperlein, Laboratory for Laser Energetics, 250 East River Road, Rochester, New York 14623 (private communication, 1989).
- [91] N. Tan-no, T. Hoshimiya and H. Inaba, "Dispersion-Free Amplification and Oscillation in Phase-Conjugate Four-Wave Mixing in an Atomic Vapor Doublet," *IEEE J. Quantum Electron.* **QE-16**, 147 – 153 (1980).
- [92] G. G. Luther and C. J. McKinstrie, "Cooperative Instabilities of Counter-propagating Light Waves in Homogeneous Plasma," to be published in *Phys. Rev. Lett.*
- [93] G. G. Luther, C. J. McKinstrie and M. V. Goldman, *Bull. Am. Phys. Soc.* **35**, 1943 and 2126 (1990).

- [94] P. E. Young, H. A. Baldis and K. G. Estabrook, "Scattered Light Near the Laser Wavelength from Nova Two-Color Experiments," *Phys. Fluids B* **3**, 1245 – 1249 (1991).
- [95] R. P. Drake, R. E. Turner, B. F. Lasinski, E. M. Campbell, W. L. Kruer, E. A. Williams and R. L. Kauffman, "Measurements of Absorption and Brillouin Sidescattering from Planar Plasmas Produced by $0.53\mu\text{m}$ Laser Light," *Phys. Fluids B* **1**, 1295 – 1300 (1989).
- [96] J. B. Geddes, R. Chang, W. J. Firth, J. V. Moloney and E. M. Wright, "Three-Dimensional Simulations and Analysis of Hexagonal Formation in a Kerr Medium," OSA Annual Meeting, San Jose, California, November 3 – 8, 1990.